

2017

Coarse-Grained and Analytical Models for Vesicle-to-Membrane Adhesion Mechanisms

Nicole Fortoul
Lehigh University

Follow this and additional works at: <http://preserve.lehigh.edu/etd>



Part of the [Chemical Engineering Commons](#)

Recommended Citation

Fortoul, Nicole, "Coarse-Grained and Analytical Models for Vesicle-to-Membrane Adhesion Mechanisms" (2017). *Theses and Dissertations*. 2592.

<http://preserve.lehigh.edu/etd/2592>

This Dissertation is brought to you for free and open access by Lehigh Preserve. It has been accepted for inclusion in Theses and Dissertations by an authorized administrator of Lehigh Preserve. For more information, please contact preserve@lehigh.edu.

**Coarse-Grained and Analytical Models for
Vesicle-to-Membrane Adhesion Mechanisms**

by

Nicole Fortoul

A Thesis

Presented to the Graduate and Research Committee

of Lehigh University

in Candidacy for the Degree of

Doctor of Philosophy

In

Chemical Engineering

Lehigh University

May 2017

Copyright by Nicole Fortoul

May 2017

Approved and recommended for acceptance as a dissertation in partial fulfillment of the requirements for the degree of Doctor of Philosophy in Chemical Engineering.

Date

Professor Anand Jagota
Dissertation Advisor

Accepted Date

Committee Members:

Professor Jeetain Mittal

Professor Bryan W. Berger

Professor Dmitri Vezenov

Professor Dimitrios Vavylonis

Acknowledgements

I have had a great amount of support from everyone both professionally and at home. I would first like to thank my advisor, Professor Anand Jagota, for his support and patience throughout my PhD. Throughout my time he has ensured that I had a strong foundation and understanding of the fundamental science behind our work through one-on-one meetings and suggestions for classes. Professor Jagota was a source of motivation and instilled the idea of producing quality research and presenting that research to others through talks and conferences. During this process, Professor Jagota has changed me into more of a critical thinker and problem solver which will help me throughout my future career.

I would also like to thank our collaborator, Professor Maria Bykhovskaia from Wayne State University, for always giving valuable insight in the neuroscience aspects of our SNARE work and helping to build my background in biology. I am thankful for our collaborators, Professor Herbert Hui and Pankaj Singh from Cornell University, for their help and collaboration in our SNARE modeling and analysis. I have worked closely with Pankaj Singh, and he has always been an approachable source for any modeling help. I would also like to thank our collaborator Professor Frank Zhang for his input and help in the EBOV and host cell modeling particularly in his knowledge of the biological system and AFM experiments.

I would like thank Professor Bryan Berger and his lab, particularly Logan MacDonald, for training me in protein transformation, expression, and purification and allowing me to use their lab and supplies. They were an invaluable, knowledgeable

resource for all of my experimental work. Thank you to the rest of my dissertation committee, Professor Jeetain Mittal, Professor Dimitri Vezenov, and Professor Dimitrios Vavylonis, for their time and feedback throughout this process.

I thank my group members, both past and present, Akshaya Shankar, Sara Iliafar Cook, Yoona Yang, Nichole Asermely, Zhenping He, Mark Lee, Jonathan Dillen, Ying Bai, Dadhichi Paretkar, and Nichole Nadermann for always being there as a source of help and making this journey an enjoyable one. I would like to give a large thank you to the faculty and staff of the Chemical and Biomolecular Engineering Department at Lehigh University for always being helpful and giving me the best undergraduate and graduate experience that I could ask for.

Finally I would like to thank my family and friends for all of their love and support throughout my education. My fiancé, James, has been a source of encouragement particularly during stressful times. My parents, Alejandro and Kathleen Fortoul, have always made sure that my education was a priority since I was a small child, and I will always be grateful for that. My brother and sister, Alejandro Jr. and Rebecca, have been my best friends and a couple of my greatest supporters to the point that they are both now pursuing their own doctoral degrees in physical therapy and pharmacy.

Table of Contents

List of Tables.....	xi
List of Figures.....	xii
Abstract.....	1
Chapter 1: Introduction to Molecular Adhesion, SNAREs, EBOV, Multi-Scale Modeling, Simulation Techniques, and Previous Studies.....	4
1.1 Introduction.....	4
1.2 Computational Modeling Scales.....	8
1.3 Simulation Techniques.....	12
1.4 SNARE Optical Tweezers Experiment.....	14
1.5 Appendix.....	17
1.5.1 Derivation of the Standard Deviation of the Random Force in Brownian/Langevin Dynamics.....	17
1.5.2 Derivation of Brownian Dynamics Criteria.....	20
1.6 References.....	22
Chapter 2: Coarse-Grained Model of SNARE Mediated Docking.....	25
2.1 Introduction.....	26
2.2 Materials and Methods.....	29
2.2.1 All Atom Simulations.....	29
2.2.2 SNARE Coarse-Grained Model.....	29
2.2.3 Continuum Model of the Vesicle and Plasma Membrane.....	37

2.2.4	Governing Equations for the Continuum Membrane Model and Their Solution	42
2.3	Results	44
2.3.1	Force-Displacement Response of the Vesicle-Membrane Interaction	44
2.3.2	SNARE Force-Separation Curve	45
2.3.3	Combined SNARE and Vesicle-Membrane Results	48
2.4	Discussion and Conclusion	54
2.5	Appendix	57
2.5.1	Coarse-Grained Simulations: Solution Procedure	57
2.5.2	ENM Reference State	59
2.5.3	Determining the Cut-Off Distance and Spring Constant in the Elastic Network Model for SNARES	61
2.5.4	Calibration of λ and Displacement Orientation	65
2.5.5	SNARE Force Displacement Instabilities and Their Effect on Energy	67
2.5.6	Continuum Governing Equations and Their Solution	68
2.5.7	Example Problem of Continuum Model	73
2.5.8	SNARE Force Separation Curve Shift	74
2.5.9	Choice of SNARE Model	76
2.5.10	Robustness of Model Results	77
2.6	References	91
Chapter 3: Coarse-Grained Model of SNARE Shows that Partial Assembly and Helicity are Required for Quick Zippering		
3.1	Introduction	100

3.2	Materials and Methods	104
3.2.1	Simulation Methods	104
3.2.2	First Step: Separating Syb from the SNARE Under Force Control.....	105
3.2.3	Re-assembly of SNARE	108
3.3	Results and Discussion.....	110
3.3.1	SNARE Unzippering and Assembly with Fully Helical Syb	111
3.3.2	SNARE Unzippering and Assembly with Syb Melting and Rapid Helix Formation.....	114
3.3.3	SNARE Unzippering and Assembly with Syb Melting and Helix Formation with Distance Criterion.....	117
3.3.4	Combining the Results of Fully Helical Syb and Rapid Helix Reformation Case	120
3.4	Appendix	123
3.4.1	Adjustment of CG Parameters from Chapter 2 and Fortoul et al. ⁸	123
3.4.2	Force Based MC Unraveling Method	126
3.4.3	Force Control Pulling Rate	130
3.4.4	Helical Formation/Raveling Methods.....	131
3.5	References	135
Chapter 4: SNARE Protein Expression, Purification, and Characterization		139
4.1	Introduction	139
4.2	Materials and Methods	140
4.2.1	SNARE Sequence	140
4.2.2	SNARE Protein Expression and Purification	142

4.2.3	Surface Functionalization on Silicon Wafer	142
4.2.4	Surface Functionalization for JKR Experiments	144
4.2.5	JKR Experiments	145
4.3	Results and Discussion.....	145
4.4	Appendix	151
4.4.1	Protein Expression and Purification Protocol.....	151
4.4.2	Protein Flash Freezing and Tip Sonication Protocol	152
4.4.3	Protein Purification Protocol.....	153
4.4.4	Moles of PEG Calculation	153
4.4.5	Protein Purification Gels.....	154
4.4.6	Thrombin Cleavage Gels	155
4.5	References	157
Chapter 5: Analytical Model and Kinetics of TIM Protein-Mediated Ebola Virus-Host		
Cell Adhesion.....		
5.1	Introduction	158
5.2	Materials and Methods	161
5.2.1	Analytical Model of EBOV-Host Cell Interaction	161
5.2.2	Kinetics of TIM Protein-Mediated Ebola Virus-Host Cell Adhesion	165
5.3	Results and Discussion.....	167
5.3.1	Analytical Model of EBOV-Host Cell Interaction	167
5.3.2	Kinetics of TIM Protein-Mediated Ebola Virus-Host Cell Adhesion	171
5.4	Appendix	172

5.4.1	Mechanics of Virus Attachment by Adhesion When Bending Dominates	
	Over Tension	172
3.6	References	177
Chapter 6: Conclusions and Future Work.....		179
6.1	Main Results.....	179
6.2	Ongoing and Future Work.....	181
6.3	References	183
Curriculum Vitae.....		184

List of Tables

Table A2.1	The lowest natural frequencies and characteristic times for Syb determined are shown below for different values of k_s63
Table A2.2	The RMSD values between the AA and CG fluctuation spectra are shown below for all helices for a range of values of k_s . The minimum RMSD values are shaded in grey.....64
Table A2.3	Parameters used for the continuum model of the vesicle and plasma membrane.....73
Table 4.1	Two sets of ellipsometry experiments were done on for surface functionalizations on silicon wafer. These experiments showed that with each new layer added to the sample there was an additional thickness gained in the sample.147
Table 4.2	The advancing and receding contact angles were determined for all samples in sample set 1 and sample set 2 that correspond to the samples in Table 4.1.....148
Table 4.3	The results of JKR experiments are shown for several sample types. The results were robust for the three experiments performed for each sample type.149

List of Figures

- Figure 1.1 A schematic of a general endocytosis/exocytosis problem is shown. An object with a curved surface (say, a vesicle or a viral particle) is repelled from second surface (say, the plasma membrane). Some specific adhesive molecular interaction is needed to bring the two surfaces into proximity. Two circles indicate the width of the contact region. 4
- Figure 1.2 (A) A schematic of 2 SNAREs and the vesicle/membrane system is shown including Syb (*blue*), Syx (*red*), and SNAP25 (*orange*). (B) A schematic of the SNARE and the vesicle/membrane system as the vesicle approaches the membrane. In this view, Syb (*blue*), Syx (*red*), SN1 (*orange*), and SN2 (*gray*) have formed 2 SNARE bundles. 5
- Figure 1.3 (A) Schematic of the adhesion of EBOV and the cell membrane is shown. (B) A schematic of the TIM-1 receptor coming into contact with the EBOV surface is shown. 8
- Figure 1.4 Computational modeling types are shown as a function of length scale and timescale including quantum level, all atom, coarse-grained, mesoscale, and continuum models. 9
- Figure 1.5 (A) Diagram of the optical tweezers setup in Gao et al.'s⁹ experiment. The ternary SNARE complex comprises Syb (*blue*), Syx (*green*), and SNAP25 (*purple*). The C-terminal end of Syb was attached to a DNA handle attached to Dig attached to an optical bead. The C-terminal end of Syx was attached to Biotin attached to an optical bead. Syb and Syx were linked at their N-

terminal ends. The N-terminal domain (*NTD*), C-terminal domain (*CTD*) and the linker domain (*LD*) of the SNARE bundle are indicated. (B) Force extension curve for SNARE unzipping (*black*) and zipping (*gray*). The worm-like-chain model fits for the four unzipping stages are shown (1,2,3,4, *red*). Figures 1.5A and 1.5B were published by Gao et al.⁹ and copyright permission was obtained prior to the submission of this document..... 15

Figure 1.6 The unfolding probability of Syb (up to the ionic layer) is shown as a function of force. Figure 1.6 was published by Gao et al.⁹ and the copyright permission was obtained prior to the submission of this document. 17

Figure 2.1 (A) The AA (*left*) and CG (*middle*) representations of the SNARE bundle are shown. Both models include helices Syb, Syx, SN1, and SN2 with each helix contributing one residue to the ionic layer (*beads*): R56, Q226, Q53, and Q174 respectively. The C-terminal ends of Syb and Syx play an integral role in the fusion process in that they attach to the vesicle (Syb) and plasma membrane (Syx). The ENM spring network (*right*) that maintains the individual helical structure is shown for Syb and Syx where the thick lines represents the $C\alpha$ backbones and the thin lines represent ENM springs. The Miyazawa and Jernigan contacts between Syb and Syx are also represented (*dotted lines*). (B) The spectra used to compare the fluctuations of the AA and CG models are shown for Syb. Values for k_s of 0.0963 N/m and R_c of 20 Å were used for the CG model. The inset shows 10 snapshots of Syb during the corresponding AA simulation. (C) Mean distance for different

values of parameter A along with snapshots of the SNARE bundle. The original crystal is represented by the black line. The version chosen for simulation is marked by the black circle..... 31

Figure 2.2 (A) A schematic of the axisymmetric model in the undeformed configuration, showing the location of SNARE and direction of force applied. (B) The repulsive forces (shown by the dotted lines) act on the deformed configuration of the vesicle as does the SNARE force, F . (C) The figure shows the convention for shear force (Q), in-plane tension (T), and moment (M) acting on the cross-section of the membrane a location ξ (S), where ϕ (S) is the tangent angle in the undeformed configuration measured from the vertical. (D) Example of a deformed vesicle-plasma membrane complex for a 20-nm diameter vesicle docked by 15 SNAREs..... 39

Figure 2.3 (A) Force versus SNARE end separation for the vesicle-membrane system for different numbers of SNAREs for the hydration repulsion case. (B) The force during separation of the ends of the SNARE bundle using λ of 0.30 for the CG model of SNARE along with snapshots of the SNARE bundle at the corresponding C-terminal end separation. The end separation is defined as the distance between the Syb and Syx C-terminal beads. Syb, Syx, the ionic layer residues (*beads*), and the C-terminal residues (*beads with arrows*) that are attached to pulling beads are shown in each SNARE snapshot. The purple arrows correspond to the direction along which the C-terminal beads are being pulled. (C) The force as a function of Syb-Syx C-

terminal distance is shown for the vesicle-membrane (the exponentially decreasing curves) and SNARE. One (*solid line*), two (*dash line*), and three (*dash-dot line*) SNAREs are shown in this plot. Intersections between the vesicle-membrane and SNARE force-displacement responses represent equilibrium states. There are a number of instabilities represented by load-drops. These correspond to separation of individual layers and have been so labeled. 46

Figure 2.4 (A) Energy as a function of SNARE end separation when repulsion between the vesicle and plasma membrane is dominated by hydration repulsion. The energetic contributions from SNARE (attractive), hydration (repulsive), and the total (their sum) are shown. The hydration repulsion has been shifted vertically by -17 kT for clarity. (B) Contour plot of total energy as a function of SNARE end separation distance for different numbers of SNAREs under hydration repulsion. Circles correspond to global energy minima representing the equilibrium SNARE end separation for a given number of SNAREs. Vesicle radius is 20 nm. (C) Contour plot of total energy as a function of SNARE end separation distance for different numbers of SNAREs under electrostatic repulsion for a fixed charge of -0.025 C/m^2 on the vesicle and the membrane in the limit of high tension in the vesicle and plasma membrane. For this case, minimum lateral separation between the SNARE bundles has been increased from 3 nm to 4nm. (D) The structure of SNARE corresponding to the case shown in Fig. 4 B, number of SNAREs=1. Syb, Syx, SN1, SN2 are shown with the ionic layer residues

indicated as large beads. (E) The same structure as in Fig. 4 D but showing only Syb and Syx for clarity. All contacts for residues within 2σ of each other are indicated with thin lines..... 51

Figure A2.1 A model showing two beams. The reference or zero energy state for both beams is when they are separated from each other. When the beams form a bundle, mutual interactions deform them into some shape with associated stored energy that will be released when the beams are separated.....59

Figure A2.2 A histogram for the number of ENM springs per bead is shown for Syb with a value of 20 Å for R_c62

Figure A2.3 The spectra used to compare the fluctuations of the AA (*blue*) and CG (*red*) models are shown for Syb for 2 ns. Values of k_s as 0.0963 N/m and R_c of 20 Å were used for the CG model. An RMSD of 4.7E-10 was found.....64

Figure A2.4 The force as a function of timestep is shown for a displacement control run with λ set to 0.30. The forces on the C-terminal beads of Syb (*blue*) and Syx (*red*) are shown. Each spike in the Syb force corresponds to application of a new displacement step. A total displacement of 20 nm is shown.....66

Figure A2.5 Force displacement curves are shown for displacement control simulations done using λ values of 0.16 (*red*), 0.24 (*blue*), 0.30 (*black*), and 0.40 (*magenta*).....67

Figure A2.6 (A) Arc length and tangent angle over the membrane, (B) Forces and moment along the cut in the membrane.....69

Figure A2.7 Deformed geometry for different force magnitudes. The thick lines represent the neuron base and the thin lines represent the vesicle. The inset on the left shows the zoomed in section of the load application point (shown as •) and the inset on the right shows the vertical separation between the two ends of SNARE-machinery versus the net SNARE force. The parameters are for the analysis are: load application point, $\bar{s}_0 = \pi / 6$, pretension in plasma membrane, $\bar{t}_0 = 1$ and vesicle pressure. $\bar{p}_0 = 1$ 74

Figure A2.8 Drawing of a vesicle near a plane along with a model for the SNARE bundle.....75

Figure A2.9 (A) The force in the membrane/vesicle system is shown as a function of SNARE end separation for a vesicle radius of 20nm with electrostatic repulsion with a fixed surface charge. (B) The corresponding contour plot of total energy as a function of SNARE end separation distance and the number of SNAREs. Gray circles correspond to global energy minima representing the equilibrium SNARE end separation for a given number of SNAREs.....78

Figure A2.10 The force in the membrane/vesicle system is shown as a function of SNARE end separation for a vesicle radius of 100nm with (A) hydration repulsion and (C) electrostatic repulsion with a fixed surface charge. Contour plots of total energy as a function of SNARE end separation distance and the

number of SNAREs are shown for a vesicle radius of 100nm with (B) hydration repulsion and (D) electrostatic repulsion with a fixed surface charge. Gray circles correspond to global energy minima representing the equilibrium SNARE end separation for a given number of SNAREs.....79

Figure A2.11 For a 20nm vesicle with hydration repulsion, contour plots of normalized total energy as a function of SNARE end separation distance and the number of SNAREs are shown. Gray circles correspond to energy minima representing the equilibrium SNARE end separation for a given number of SNAREs. Several cases are shown: (A) 2 helical turns unraveled, (B) Syx frozen, (C) SNAP25 frozen, and (D) Syx and SNAP25 frozen.....82

Figure A2.12 For a 20nm vesicle with electrostatic repulsion assuming a fixed surface charge, contour plots of normalized total energy as a function of SNARE end separation distance and the number of SNAREs are shown. Gray circles correspond to energy minima representing the equilibrium SNARE end separation for a given number of SNAREs. Several cases are shown: (A) 2 helical turns unraveled, (B) Syx frozen, (C) SNAP25 frozen, and (D) Syx and SNAP25 frozen.....83

Figure A2.13 For a 20nm vesicle with high osmotic pressure and low pretension in the plasma membrane with constant potential the vesicle and plasma membrane structures are shown including their bilayer thickness for (A) 10 SNAREs and (B) 15 SNAREs.....85

Figure A2.14 Contour of normalized total energy as a function of SNARE end separation and number of SNAREs for a 20nm vesicle with high osmotic pressure and low pretension in the plasma membrane, and with constant potential on the vesicle and plasma membrane. White circles correspond to energy minima representing the equilibrium SNARE end separation for a given number of SNAREs.....86

Figure A2.15 For the high vesicle pressure high membrane tension limiting case, the net applied force in the membrane/vesicle system is shown as a function of SNARE end separation for a vesicle with a (A) 20nm radius with fixed charge, (B) 20nm radius with fixed surface potential, (C) 100nm radius with fixed charge, and (D) 100nm radius with fixed surface potential.....88

Figure A2.16 For the high vesicle pressure high membrane tension limiting case, the net applied force in the membrane/vesicle system is shown as a function of SNARE end separation for a radius for a vesicle with a 20nm radius with fixed charge when (A) the SNARE bundle diameter is 2nm and (B) the SNARE bundle diameter is 2nm.....89

Figure A2.17 For the high pressure high tension limiting case, contour plots of normalized total energy as a function of SNARE end separation distance and the number of SNAREs are shown. Gray circles correspond to energy minima representing the equilibrium SNARE end separation for a given number of SNAREs. Several cases are shown for the vesicle with a radius of 20nm and fixed charge. The size of the SNARE bundle was varied to (A) 2nm and (B) 4nm.....90

Figure 3.1 A schematic in which the synaptic vesicle and plasma membrane are shown along with the CG model of SNARE including Syb (*blue*), Syx (*red*), SN1 (*gray*), and SN2 (*orange*). The pulling beads (*green*) for Syb and Syx are indicated where the Syx pulling bead is held fixed. An example of the ENM springs are shown in the inset for a portion of Syb (*blue*) and Syx (*red*) along with the MJ interactions between the two helices (*pink*). The Syb-Syx C-terminal distance is indicated as well (*purple double arrowed line*)...... 104

Figure 3.2 (A) A Markov chain model is shown for the unfolding/folding states of Syb for increasing force, according to Gao et al.⁶ Syb starts out fully helical and has a probability for the LD to melt or to remain fully helical. If the LD is melted, Syb is in state 1 where there is a probability to remain in that state, refold or melt to the IL. If Syb melts to the IL, it is in state 2 where there is a probability to remain in that state, refold to the LD, or to melt completely. If Syb is fully melted, this is irreversible and it remains in state 3. (B) The analytical probability of LD and IL being in a folded (*solid blue*) or unfolded (*dashed red*) state are shown for Syb as functions of applied force. These match the experimentally estimated values of P_u (*red circles*) and P_f (*blue X's*) from Gao et al. At low forces, there is reversible transition between a folded and unfolded state (shown with a blue arrow and structures) with the folded state being favored. At high forces, there is reversible transition between a folded and unfolded state (shown with a red arrow and structures) with the unfolded state being favored..... 107

Figure 3.3 Examples of a portion of an assembly simulation are shown using the two methods of helix reformation. Both simulations start from the same initial state produced using the FC method. (A) Rapid helix formation immediately turns on the ENM springs for Syb when the relaxation simulation begins and the applied force is released. (B) The distance criterion method only turns on ENM springs for residues that are within 1 nm of the SNARE bundle. The red arrow shows the portion of the Syb helix that has regained structure due to its close proximity to the bundle. The black arrow shows the portion of the Syb helix that is not within the distance criterion and has not yet regained its helical structure..... 109

Figure 3.4 The Syb-Syx C-terminal distance is shown as a function of time for fully helical SNARE unzipping (*blue traces (B and C) and snapshots 1-5 (A and D)*) using FC. Snapshots are shown for one unzipping trajectory and one assembly trajectory (*A, B, and D*). The force was released at several points within the unzipping trajectory (*black, magenta, red, and gray traces in C*) and the bundle was permitted to relax. The layer up to which the SNARE bundle is zippered is indicated for all snapshots and for several points in unzipping/assembly (*C*). For small initial SNARE openings of only a couple of layers (*black*) the bundle assembles at a relatively constant fast rate. For intermediate initial openings (*magenta and red*) the bundle starts to assemble initially at a slow rate and then assembles at a faster rate. The snapshots (*4-4c*) are shown for one specific assembly case in this intermediate region. The bundle assembles slowly from layer -4 to layer -1

(near the ionic layer). Then from layer -1 to layer 8 it assembles quickly. For large initial openings, where no layers are in contact (*gray*), the bundle first experiences a plateau and Syb fluctuates at roughly a constant distance from the bundle until layer -7 is assembled, then the bundle assembles at a constant rate. (Only a few of the BD assembly simulations are shown in this figure for clarity.)..... 112

Figure 3.5 The Syb-Syx C-terminal distance is shown as a function of time for SNARE unzipping using FC with a MC force based unraveling criterion (*blue traces (B and C) and snapshots 1-5 (A and D)*). Snapshots are shown for one unzipping trajectory and one assembly trajectory (*A, B, and D*). The force was released at several points within the unzipping trajectory (*black, magenta cyan, green, red, brown, and gray traces in C*) and the bundle was permitted to relax. The layer up to which the SNARE bundle is zippered is indicated for all snapshots and for several points in unzipping/assembly (*C*). When the force was released, the ENM springs were immediately reinstated for Syb, and helix formation occurred in $<10^4$ timesteps. For small initial SNARE openings of up to 10 nm (*black, magenta, and cyan*) the bundle assembles at a relatively constant fast rate. For intermediate initial openings (*green, red, and brown*) the bundle starts to assemble initially at a slow rate and then assembles at a faster rate. The snapshots (*4-4c*) are shown for one specific assembly case in this intermediate region. The bundle assembles slowly from layer -4 to layer 2 (near the ionic layer). Then from layer 2 to layer 8 it assembles quickly. For large initial openings

(grey) the bundle first experiences a plateau and Syb fluctuates at roughly a constant distance from the bundle until layer 2 is assembled, then the bundle assembles at a constant rate. For the largest initial separations (*dark green*) SNARE does not re-assemble within the duration of the simulation. Note that even for small separations of ~ 5 nm, the bundle is unzipped to layer - 3. This is due to the unraveling of Syb which disrupts the interaction between Syb and Syx/SNAP25. (Only a few of the BD assembly simulations are shown in this figure for clarity.) 115

Figure 3.6 The Syb-Syx C-terminal distance is shown as a function of time for SNARE unzipping using FC with a MC force based unraveling criterion (*blue traces (B and C) and snapshots 1-5 (A and D)*). Snapshots are shown for one unzipping trajectory and one assembly trajectory (*A, B, and D*). The force was released at several points within the unzipping trajectory (*magenta, dark green, gray, black, red, green and yellow green in C*) and the bundle was permitted to relax. The layer up to which the SNARE bundle is zippered is indicated for all snapshots and for several points in unzipping/assembly (*C*). When the force was released, the ENM springs were reversibly replaced using a distance criterion as described in the methods section. For small initial SNARE openings of up to 10 nm (*magenta, dark green, grey, and black*) the bundle assembles at a relatively constant fast rate. For intermediate initial openings (*red and yellow green*) the bundle starts to assemble initially at a slow rate and then assembles at a faster rate. The snapshots (*4-4c*) are shown for one specific assembly case

in this intermediate region. The bundle assembles slowly from layer -4 to layer 2 (near the ionic layer). Then from layer 2 to layer 8 it assembles quickly. For large initial openings (*green*) the bundle first experiences a plateau and Syb fluctuates at roughly a constant distance from the bundle until layer 0 is assembled, then the bundle assembles at a constant rate. Note that even for small separations of ~ 5 nm, the bundle is unzipped to layer -3. This is due to the unraveling of Syb which disrupts the interaction between Syb and Syx/SNAP25. (Only a few of the BD assembly simulations are shown in this figure for clarity.) 118

Figure 3.7 (A) A schematic is shown defining pseudo assembly time. Initial Syb-Syx C-Terminal distance, **d_1** , is that distance at the start of a relaxation simulation when the force is released. The time required from that point to SNARE bundle formation is defined as pseudo assembly time **Δt_1** . Initial helical Syb-Syx C-Terminal distance, **d_2** , is the Syb-Syx distance during a relaxation simulation when Syb first becomes helical. The time required from that point to SNARE bundle formation is defined as pseudo assembly time **Δt_2** . (B) **Δt_2** as a function of d_2 was fitted with an exponential function, **$\Delta t_1 = 4.96nsexpd^{13.10nm}$** . Fully helical (*circle*), rapid helix reassembly (*asterisk*), and distance criterion method (*triangle*) cases follow the same trend when only helical distance is taken into account..... 121

- Figure A3.1 The free energy diagram for the transition to/from the folded state to the unfolded state of Syb is shown. The relative positions of the different states can vary depending on the applied force.....127
- Figure A3.2 The force as a function of time is shown for 2 fully helical unzipping runs. The applied force on the C-terminal Syb bead (*dotted line*) as well as the negative of the force on the C-terminal Syx bead (*solid line*) are shown. (A) If a pulling rate of $2.2\text{E-}1$ pN/ns is used which leads to the Syb and Syx C-terminal forces not being in equilibrium with one another. (B) If a slower pulling rate of $5.6\text{E-}2$ pN/ns is used the forces are closer together and the system is closer to equilibrium.....130
- Figure A3.3 In order to prove that the rapid helix formation model is indeed “rapid”, the Syb structure was isolated with the N-terminal bead held fixed and a restraint on the C-terminal bead. The ENM springs for 10 helical turns were removed and Syb was stretch using displacement control on the C-terminal bead for which snapshots are shown. After Syb was stretched, the restraint on the C-terminal bead was released, and Syb was permitted to relax back into a helix (snapshots shown). This was accomplished in 7800 timesteps.....132
- Figure A3.4 Two simulations were done where force dependent MC unraveling/raveling was used to unzip the SNARE bundle (*blue*) and set up an initial state for two distance criterion relaxation simulations. One relaxation simulation was

done with an R_{DC} of 0.5 nm (*black*) and another with an R_{DC} of 1 nm (*red*).....134

Figure 4.1 The sequences used for the SNARE proteins are shown using the pMBP7 cloning vector including MBP (*underlined*), 2 his-tags for purification (*gray*), a thrombin cleavage site (*green*), and the SNARE sequences (*yellow*). 141

Figure 4.2 Structures are shown for (A) piranha cleaned silicon wafer functionalized with APTES, (B) piranha cleaned silicon wafer functionalized with APTES with NHS-PEG3400-MAL and NHS-PEG2000 in solution, (C) piranha cleaned silicon wafer functionalized with APTES and PEGS with a helical protein with a C-terminal cysteine (Syb or Syx) in solution, (D) and the final surface layer structure. Figure 4.2 was published by Idiris et al.⁴ and the copyright permission was obtained prior to the submission of this document..... 143

Figure 4.3 The JKR adhesion setup is shown including a PDMS functionalized surface with Syx and a glass indenter functionalized with Syb. SNAP25 is added in solution immediately before the adhesion experiments are performed. . 144

Figure 4.4 The electrophoresis gel for them IMAC effluents for the Syb + MBP purification is shown with the sample wells labeled. Syb + MBP (56 kDa) is present in wells 6 – 15..... 145

Figure 4.5 The electrophoresis gel for thrombin cleavage of Syb and MBP are shown. In the first well is Syb + MBP. The other wells contain the addition of thrombin

	with incubation times of 30 min, 1 hour, and 2 hours respectively for all of which thrombin cleavage is successful.	146
Figure 4.6	Successful force displacement data for an overnight JKR experiment for SNARE adhesion is shown. Upon recession from the PDMS surface, the glass indenter experiences an adhesive force.....	150
Figure A4.1	The electrophoresis gel for them IMAC effluents for the Syx + MBP purification is shown with the sample wells labeled. Syx + MBP (56 kDa) is present in wells 5 – 15.....	154
Figure A4.2	The electrophoresis gel for them IMAC effluents for the SNAP25 + MBP purification is shown with the sample wells labeled. SNAP25 + MBP (67 kDa) is present in wells 6 – 15.....	155
Figure A4.3	The electrophoresis gel for thrombin cleavage of Syx + MBP and SNAP25 + MBP are shown. To the left of the protein ladder in the first well is SNAP25 + MBP. The other wells (to the left of the ladder) contain the addition of thrombin with incubation times of 30 min, 1 hour, and 2 hours respectively for all of which thrombin cleavage is successful. To the right of the protein ladder in the first well is Syx + MBP. The other wells (to the right of the ladder) contain the addition of thrombin with incubation times of 30 min, 1 hour, and 2 hours respectively for all of which thrombin cleavage is successful.....	156
Figure 5.1	(A) Schematic of the adhesion of EBOV and a deformed host cell membrane is shown including TIM-1 receptors on the host cell. (B) A schematic of the TIM-1 receptor coming into contact with the EBOV surface. TIM-1	

comprises a negatively charged stalk or mucin-like domain, MLD, and a positively charged head group, IgV. The base of the TIM-1 stalk is imbedded in the cell membrane that is covered with a flexible glycocalyx layer. The surface of the virus is negatively charged and covered with PS and large glycoproteins. 159

Figure A5.1 Example of normalized total energy as a function of normalized deflection and contact-half-width for $\alpha = 0.85$ and $\bar{l} = 5$. For each deflection, we find the value of normalized contact half-width that minimizes total energy. Then, along the locus of these points (black line in the figure), we search for the condition that shear force is zero.176

Abstract

Molecular adhesion is the basis for many complicated biological processes. In particular the role of regulated adhesion of the vesicle to the plasma membrane in exocytosis as part of synaptic transmission is crucial. This adhesion must overcome the long-range electrostatic and hydration repulsion in a mediated fashion. Complications within this neurological process can lead to serious diseases and disorders such as schizophrenia and botulism. Little is understood about the mechanistic details of this process. Therefore, developing fundamental knowledge is invaluable to the design of treatments and therapies. Many molecular players have been identified to take part in this process, but we focus on SNARE (soluble N-ethylmaleimide-sensitive factor attachment protein receptor) because that is the central conserved player. SNARE proteins are the workhorses of this adhesion and therefore developing an understanding of their role in the process is important. This is a very complex system, so in addition to experiments, modeling of the system is also required, and there are several options available. Because of the combination of long length scale (10s of nm) and time scales (1-10s of μ s, to seconds), it is difficult to study this system using all-atom simulations. Therefore residue based coarse-grained (CG) Brownian dynamics simulations are used that are validated by both experimental data and detailed all-atom simulation results. The CG model of SNARE included an elastic spring-network model for intrahelical interactions and chemically specific Miyazawa and Jernigan potentials for helix-helix interactions.

Using this CG model this thesis investigates two underlying questions dealing with synaptic vesicle to membrane docking/fusion that have yet to be definitively answered: (1)

how many SNAREs are required in this process? and (2) how do SNAREs assemble? The force-displacement relationship for the unzipping of SNARE was determined using CG displacement control simulations. These results were combined with a continuum model of the vesicle/membrane including electrostatic and hydration repulsion to predict that 1 SNARE can bring the vesicle to within 3 nm of the membrane. This docking distance can be reduced as additional SNAREs are added. However, adding more than 4-6 SNAREs increases the minimum distance between the vesicle and plasma membrane. The vesicle was never brought closer than 2nm to the membrane, suggesting that SNAREs alone are not sufficient for vesicle to membrane fusion, that their principal role is docking.

Next, the SNARE assembly process was studied using the CG model. Two models for SNARE assembly are proposed in the literature: (1) Munc18 acts as a template for SNARE assembly by holding SNARE in a semi-zipped conformation and promoting helicity, and (2) SNARE serves as a self-template for zippering and assembly. Force control unzipping simulations were performed to set up initial states for assembly simulations. Several simulations were performed mimicking the two hypotheses. We find that assembly time grows exponentially with how far the SNARE has been unzipped, and this assembly time is increased even more with the degree of unfolding. We find that helical SNAREs assemble rapidly, however it is known (from experiments) that unstructured, completely disassembled SNAREs assemble in ms to s timescales. Therefore, Munc18 or another chaperone would most likely be required to promote a half-zipped SNARE state prior to assembly.

We tackled another system of importance due to its deadly and contagious

characteristics: the Ebola virus (EBOV) internalization by the host cell which is an adhesion problem of comparable length and time scales. A better understanding of this system will lead to the development of possible vaccines/therapies. Again this system included two negatively charged surfaces, EBOV and the host cell membrane. We developed an analytical model to investigate the parameters required for EBOV ingestion into the host cell. We studied this system at two limits: (1) membrane bending dominates in resisting deformation and (2) membrane tension dominates in resisting deformation. From the membrane bending limit study, a dimensionless parameter representing the ratio of membrane bending stiffness to adhesion was found that determines whether EBOV will be engulfed into the host cell. From the membrane tension limit study we also extract a dimensionless parameter representing the ratio of membrane tension to adhesion that determines whether engulfment will occur. In particular, these dimensionless parameters can be used to relate single-molecule force spectroscopy measurements to the behavior at the length scale of the full virus.

Chapter 1: Introduction to Molecular Adhesion, SNAREs, EBOV, Multi-Scale Modeling, Simulation Techniques, and Previous Studies

1.1 Introduction

Molecular adhesion is the basis for many biological processes ranging from cell-cell adhesion to protein function. There is an entire class of protein-mediated endocytosis and exocytosis problems that are dominated by molecular adhesion shown in Fig. 1.1.

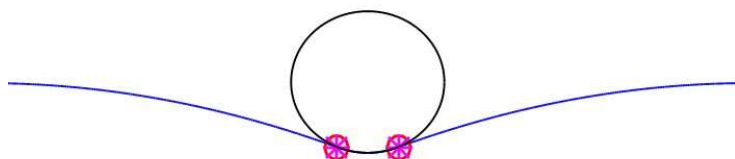


Figure 1.1 A schematic of a general endocytosis/exocytosis problem is shown. An object with a curved surface (say, a vesicle or a viral particle) is repelled from second surface (say, the plasma membrane). Some specific adhesive molecular interaction is needed to bring the two surfaces into proximity. Two circles indicate the width of the contact region.

At first glance, all of these problems look quite similar where there is a curved object with a negative surface charge interacting with a flat membrane also with a negative surface charge due to lipid composition. There is a repulsive force between the membranes due to electrostatics and short-range hydration repulsion that is counteracted by the adhesive force provided by some group of molecular players. The inside of a cell is very crowded and processes are intertwined and complicated, but this set of problems can be simplified to this curved and flat surface system. We chose to study two specific systems in this class of problems: (1) Soluble N-Ethylmaleimide-sensitive Factor Attachment Protein Receptor

(SNARE) mediated synaptic vesicle to membrane docking/fusion and (2) T-cell immunoglobulin and mucin domain (TIM) mediated host cell Ebola virus internalization.

In particular, the role of regulated adhesion of a synaptic vesicle to the plasma membrane in exocytosis is crucial for synaptic transmission. This adhesion must overcome the long-range electrostatic and hydration repulsion in a mediated fashion. Complications within this neurological process can lead to serious diseases and disorders such as schizophrenia and botulism¹. SNARE complexes are the core machinery in synaptic vesicle-membrane docking and fusion. The SNARE complex is a 4-helix bundle comprising vesicle bound transmembrane protein Synaptobrevin (Syb), membrane bound transmembrane protein syntaxin (Syx), and SNAP25 that is tethered to the plasma membrane and contributes two helices to the bundle^{2,3} as shown in Fig. 1.2.

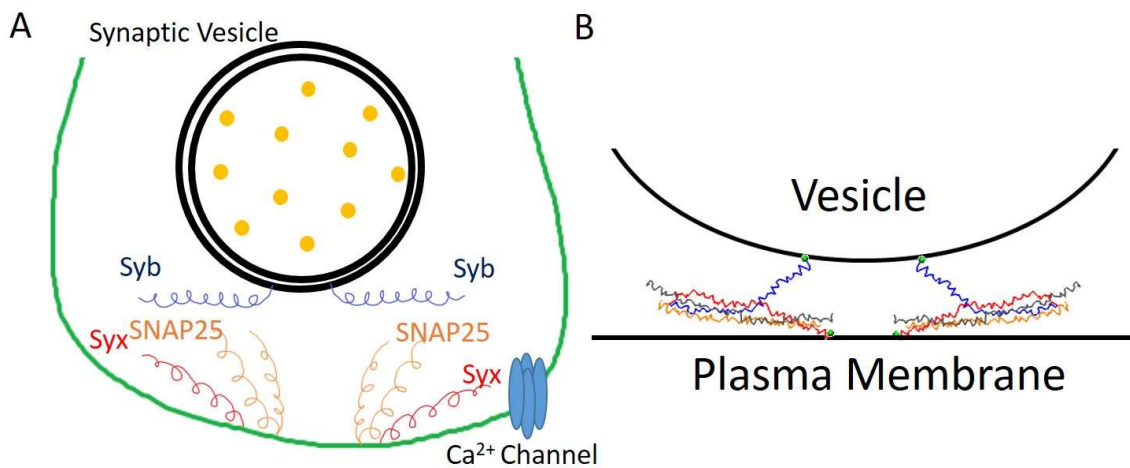


Figure 1.2 (A) A schematic of 2 SNAREs and the vesicle/membrane system is shown including Syb (*blue*), Syx (*red*), and SNAP25 (*orange*). (B) A schematic of the SNARE and the vesicle/membrane system as the vesicle approaches the membrane. In this view, Syb (*blue*), Syx (*red*), SN1 (*orange*), and SN2 (*gray*) have formed 2 SNARE bundles.

Synaptic transmission begins with an action potential traveling down the axon to the synapse causing calcium channels to open. In turn, vesicles that are docked at the plasma membrane are triggered to fuse and release neurotransmitters into the synaptic cleft⁴. It is highly debated as to how many SNAREs are necessary for this docking/fusion process. The only consensus is that the number of SNAREs is somewhere between 1 and 11⁵⁻⁸. To investigate how the number of SNAREs affects the docking/fusion process a coarse-grained (CG) model of the SNARE complex was developed, and simulations were conducted using Brownian Dynamics. In order to get a more complete picture of the docking/fusion process, the results were analyzed in conjunction with a vesicle/membrane model.

Very little work has been done on SNARE assembly. There has been an optical tweezers study, which our model was calibrated with, that did study the unfolding/folding of Syb during assembly⁹. A similar magnetic tweezers study was done that confirmed the Syb unfolding stages presented in the optical tweezers study¹⁰. However, not much has been done otherwise because experimentally this system is very complicated to study in great detail. To overcome these challenges, this system can be studied using simulations. However, long timescales of $\sim 1\mu\text{s}$ are required to study this problem which makes this a challenging system to study using AA techniques.

There are two models currently proposed for how SNARE assembly occurs. One model focuses on the role of the protein MUNC18, a chaperone of exocytosis and membrane tethering factor that aids in the initial vesicle to membrane contact¹¹. In this model, MUNC18, is required as a SNARE chaperone to serve as a template for SNARE assembly¹². A recent experimental study was performed where the x-ray crystal structure

of Vam3 and Vps33 (proteins that closely resemble Syx and MUNC18) and the x-ray crystal structure of Nyv1 and Vps33 (closely resembling Syb and MUNC18) were superimposed on one another and showed that MUNC18 holds SNARE in a mostly helical, half-zippered confirmation. The second hypothesis is that SNARE acts as its own template (“self-templating”) where once Syb interacts with Syx/SNAP25 there is a zippering effect promoting Syb helicity and bundle assembly from the C-terminus to the N-terminus of the bundle¹³. We use our SNARE CG model to study these two possible mechanisms.

A semi-analytical modeling methodology is used to study the internalization of the Ebola virus (EBOV). EBOV is extremely deadly and contagious. In the recent years it has been turning into an epidemic especially in the continent of Africa¹⁴. It is crucial that treatments and possible vaccines are developed in order to control outbreaks. In this work a simple model for the virus-host cell adhesion is developed to get a better understanding of the critical parameters for virus internalization. To infect a host cell, EBOV first attaches to the host cell using the cell’s own TIM-1 transmembrane proteins binding with the phosphatidylserine (PS) covering EBOV’s surface as shown in Fig. 1.3A¹⁵.

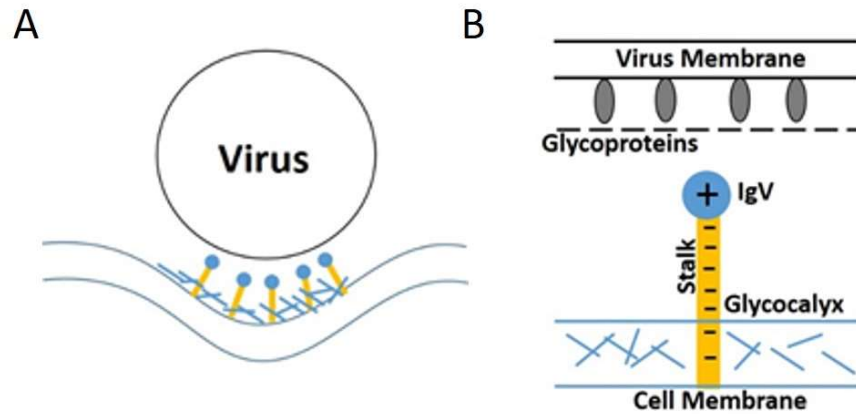


Figure 1.3 (A) Schematic of the adhesion of EBOV and the cell membrane is shown. (B) A schematic of the TIM-1 receptor coming into contact with the EBOV surface is shown.

After EBOV has attached to the cell, endocytosis occurs and it is internalized by the cell. This adhesive process is electrostatically driven by the positive charge on the TIM-1 head group, IgV, and the negative charge of the PS on EBOV as shown in Fig. 1.3B. In order to better understand the internalization process for future therapies, a simple model of the virus/host cell adhesive interaction has been developed. In particular, the model aims to relate parameters measured by single molecule force spectroscopy, such as binding free energy, to the question of whether adhesion is insufficient to enable viral engulfment.

1.2 Computational Modeling Scales

Computational modeling can be done at many different scales ranging from the subatomic to the macroscale shown in Fig. 1.4.

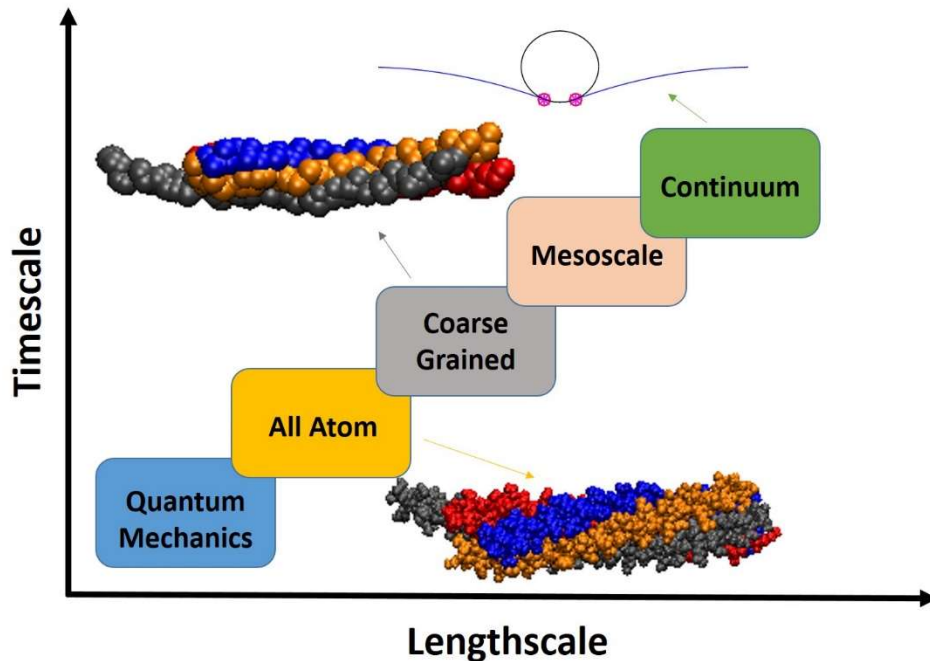


Figure 1.4 Computational modeling types are shown as a function of length scale and timescale including quantum level, all atom, coarse-grained, mesoscale, and continuum models.

The ideal model for a system should be chosen based on the minimum time and length scales that need to be represented for the system to address the questions being raised. For example, protein structure is usually modeled on the scale of several nanometers with timescales in the picoseconds-microsecond range, for which quantum mechanics would most likely be too detailed a method for the system. Quantum mechanics could be used to attain accurate information, but simulation speed would be prohibitively slow. Instead faster methods like all-atom or coarse-graining could be used.

Subatomic models include those governed by quantum mechanics such as density functional theory (DFT). At the subatomic level, Schrodinger's equations are solved and arguably this should be the most accurate level of modeling¹⁶. Realistically however,

computation time is always a concern and a finer resolution simulation will of course take more time due. Therefore, quantum level models should be used on systems with a lengthscale on the order of angstroms to a few nanometers and a timescale of femtoseconds where subatomic behavior is of great interest¹⁷.

In all-atom (AA) level modeling one usually uses classical molecular dynamics in which the position of every atom is represented. In these systems, the solvent is usually explicit as well. AA models are widely used for small biological and chemical systems to better understand the interaction between atoms. This modeling is typically done on the nanometer length scale and picosecond-microsecond time scale¹⁷. Up to microsecond long simulations can be achieved using supercomputing resources using commercial codes such as GROMACS or NAMD, which is valuable to cover a large range of molecular behaviors. However, the computational resources required for the explicit water calculation can make larger system sizes expensive to simulate.

In many phenomena in biological systems, such as those involving interaction of proteins and lipids, atomic level information is not particularly of interest. In many cases information on the amino acid level is desired which is ideal for coarse-graining (CG) techniques. In CG models, a group of atoms is chosen as a “bead” which interacts with other “beads”. The level of coarse-graining is variable; it can be anywhere from a group of atoms to a group of amino acids. In many cases techniques such as Brownian or Langevin dynamics are used in these systems, which have implicit water. The presence of implicit water greatly decreases the computational cost. There are commercial codes such as LAMMPS and MARTINI which are used for CG systems, however for some systems a “home-built” code is required. Based on the definition of a “bead”, interaction

potentials should be calibrated based on experimental data or higher resolution methods like AA. CG is usually used for length scales of 10s of nanometers and timescales of nanoseconds to milliseconds¹⁷.

For many materials systems, mesoscale modeling is of interest. This level of modeling is on the microsecond and larger timescales and micrometer length scales¹⁷. In mesoscale methods the Langevin equation and pseudo-particle dynamical approaches are often used¹⁷. On even larger scales, continuum modeling is used. In these systems there is not a “bead” or particle representation. Surfaces such as membranes, vesicles, etc. are modeled with a system of governing equations including terms such as bending, electrostatics, etc. to predict overall behavior. Continuum system calculations are often all done at equilibrium, from which kinetic information cannot be determined.

In many instances multiple methods are used to solve one problem. Smaller length/time scale methods can be used to calibrate and validate larger length/time scale methods. The key is to minimize simulation time while still producing accurate and useful results. In some systems multi-level modeling can be used. For example, for a very large enzyme one may be interested in the conformation of the enzyme as well as the details of the enzyme’s active site. Atomistic detail may be required to understand the behavior of the binding site, but CG may be all that is necessary for the rest of the enzyme. Instead of using strictly AA techniques for the entire large enzyme, the binding site could be modeled with AA and the rest of the enzyme could be modeled with CG. In other instances, multi-scale modeling can refer to models at different length scales with reduced parameters as one ascends the length scale. Multiscale modeling in one form or another is used throughout this work. SNARE proteins are studied which were

successfully simulated using CG techniques. However the SNARE, vesicle/membrane system was of interest in some cases. So, a CG model of SNARE was used in combination with a continuum model of the vesicle/membrane to provide an overall understanding of the system while minimizing simulation time. The CG model was calibrated against experimental data and using AA simulations.

1.3 Simulation Techniques

There are a variety of simulation techniques that can be used for molecular dynamic simulations. Each technique has its own advantaged and disadvantages that should be weighed based on system size, characteristic lengths, timescales, and generally what level of behavior of the system one is trying to capture. All-atom simulations are usually conducted by solving Newton's equations of motion for each particle (atom) in the system, subjected to inter-particle potentials, external fields, boundary conditions, and controls such as thermostats or barostats. Two popular techniques that are used for CG models are Langevin and Brownian dynamics. In Langevin dynamics (LD), Newton's equation of motion

$$m \frac{d\vec{v}}{dt} = -\Gamma \vec{v} + \vec{R}(t) - \nabla E \quad (1.1)$$

is integrated at every timestep. where m is the mass of the particle, \vec{v} is the velocity of the particle, Γ is the damping constant, $\vec{R}(t)$ is the random force representing the bead's interaction with the liquid, and E is the potential energy of interaction with other particles.. The random force is connected to the viscous drag through the fluctuation-

dissipation theorem¹⁸. This is explained in more detail in the Appendix along with a derivation for the standard deviation of the random force. LD is an inexpensive simulation technique that can successfully simulate interacting particles in a fluid in many cases.

An even less computationally expensive technique is Brownian dynamics (BD), which is largely used in this thesis. In Brownian dynamics the acceleration term in equation (1.1) is neglected to give us

$$0 = -\Gamma\vec{v} + \vec{R}(t) - \nabla E \quad (1.2)$$

This assumption makes the equation easier to integrate as it can be solved for explicitly, unlike the Langevin equation which requires a half velocity method. However, the Brownian assumption does miss high frequency behavior. This is acceptable for systems with low masses and low spring constants, k , which satisfy

$$\Gamma \gg 2\sqrt{km} \quad (1.3)$$

A derivation of this criterion is given in the Appendix.

Dissipative particle dynamics¹⁹ (DPD) is a third technique based on the Langevin equation that can be used. Random forces are not truly entirely decoupled; they come in pairs. Every random force on a bead or particle has a resulting opposite random force. DPD thus conserves momentum (unlike BD and LD) which yields a better approximation of hydrodynamic behavior¹⁹. Unfortunately this makes these simulations more computationally expensive. For long time scales it is generally accepted that BD and LD will produce similar behavior.

A fourth technique is Stokesian dynamics (SD)²⁰ which is also based on the Langevin equation. In this technique the hydrodynamic forces are handled in a more complex fashion, incorporating multi-particle interactions. In BD and LD the hydrodynamic force on each particle is isolated and independent. Stokesian dynamics is mainly used for nonequilibrium suspensions where particles are much larger than solvent particles. Again this technique is more computationally expensive than LD and BD due to how the hydrodynamic forces are handled.

For SNARE CG simulations, we mostly look at near-equilibrium behavior on the nanosecond scale not requiring more advanced techniques such as SD and DPD. Because our system also satisfies equation (1.3), we used BD to optimize simulation speed.

1.4 SNARE Optical Tweezers Experiment

The SNARE CG model that was developed for the majority of this thesis was calibrated partly by AA simulations and partly by an optical tweezers experiment reported by Gao et al.²¹ entitled “Single Reconstituted Neuronal SNARE Complexes Zipper in Three Distinct Stages.” In this experiment, the authors expressed and purified Syb, Syx, and SNAP25 proteins. Biologically the C-terminal end of Syb has a transmembrane domain that is extended into the vesicle membrane and the C-terminal end of Syx has a transmembrane domain that is extended into the plasma membrane. However these transmembrane domains were not included in their experiment. SNAP25 is associated with the plasma membrane as well, but is not attached in the same manner. The ternary SNARE complex/bundle was first made in solution overnight. The N-terminal ends of

Syb/Syx were tethered with a disulfide bond. Then the C-terminal end of Syb (VAMP2) was attached to a 2,260-bp DNA handle that was attached to Dig and the optical bead, as shown in Fig. 1.5A, and the C-terminal end of Syb was attached to Biotin and an optical bead.

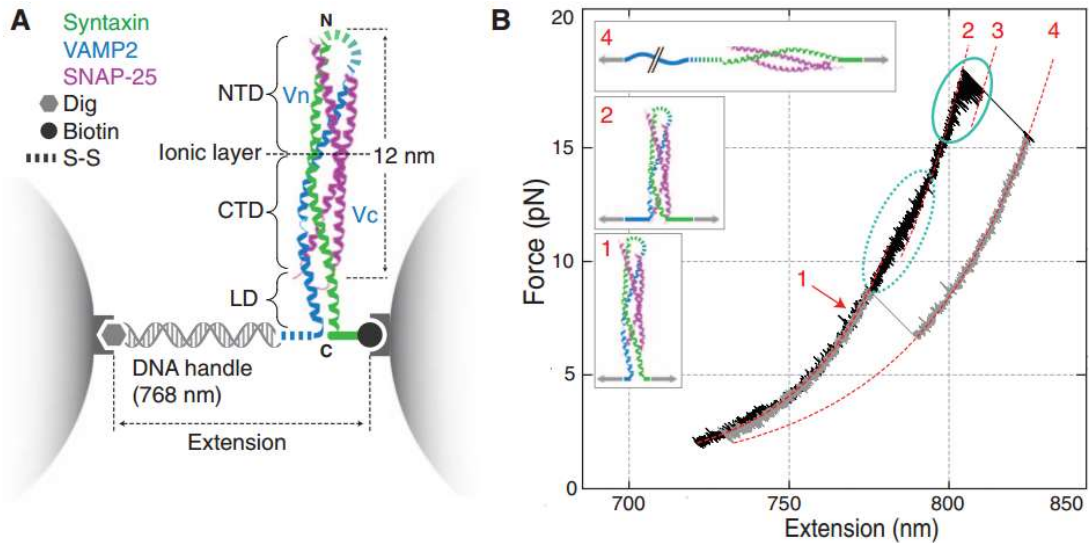


Figure 1.5 (A) Diagram of the optical tweezers setup in Gao et al.'s⁹ experiment. The ternary SNARE complex comprises Syb (*blue*), Syx (*green*), and SNAP25 (*purple*). The C-terminal end of Syb was attached to a DNA handle attached to Dig attached to an optical bead. The C-terminal end of Syx was attached to Biotin attached to an optical bead. Syb and Syx were linked at their N-terminal ends. The N-terminal domain (*NTD*), C-terminal domain (*CTD*) and the linker domain (*LD*) of the SNARE bundle are indicated. (B) Force extension curve for SNARE unzipping (*black*) and zippering (*gray*). The worm-like-chain model fits for the four unzipping stages are shown (1,2,3,4, *red*). Figures 1.5A and 1.5B were published by Gao et al.⁹ and copyright permission was obtained prior to the submission of this document.

Optical tweezers experiments were done by increasing the distance between the two optical beads using an optical trap. From this a force extension curve was determined where the extension was the distance between Dig and Biotin as shown in Fig. 1.5B. From the force extension data, they were able to predict that the SNARE bundle went through multiple folding stages during unzipping. This was determined by the fact the

force extension curve could be fit by 4 different worm-like-chain models depending on the applied force. The models differ by how much the proteins have unfolded. The stages are:

- (1) (0 – 12pN) Fully folded SNARE complex
- (2) (12pN – 17pN) Linker domain of Syb/Syx unfolded
- (3) (17pN – 20pN) Linker domain of Syx is unfolded and Syb is unfolded up to ionic layer
- (4) (20pN +) Linker domain of Syx is unfolded and Syb is completely unfolded.

The worm-like chain model is given as^{22,23}

$$F = \frac{k_B T}{P} \left(\frac{1}{4 \left(1 - \frac{x}{l}\right)^2} + \frac{x}{l} - \frac{1}{4} \right) \quad (1.4)$$

where k_B is the Boltzmann constant, T is temperature, P is the persistence length, l is the contour length, and x is the extension. Equation (1.4) is used to relate the applied force to x for the DNA linker. Equation (1.4) is used separately to relate the applied force to x for the SNARE bundle. However, l changes for SNARE depending on which of the 4 stages the molecule is in, a fully helical SNARE will have a shorter contour length than a SNARE molecule where Syb has been completely unraveled. The total extension, X , which is plotted in Fig. 1.5B is

$$X = x_{DNA} + x_{SNARE} + h \quad (1.5)$$

where the extension of the DNA and SNARE are x_{DNA} and x_{SNARE} , and h is the state-dependent extension of the SNARE complex.

For the transition from state (2) to state (3) the probability of unfolding of Syb was determined as shown in Fig. 1.6.

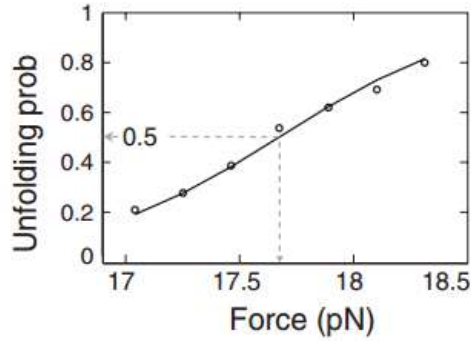


Figure 1.6 The unfolding probability of Syb (up to the ionic layer) is shown as a function of force. Figure 1.6 was published by Gao et al.⁹ and the copyright permission was obtained prior to the submission of this document.

This optical tweezers experiment was invaluable in the calibration of our SNARE coarse-grained model. The peak unzipping force was used to calibrate helix-helix interaction potential strength. Our force-dependent Syb unfolding model was built around the unfolding probabilities given in Fig. 1.6.

1.5 Appendix

1.5.1 Derivation of the Standard Deviation of the Random Force in Brownian/Langevin Dynamics^a

The Brownian Dynamics equation is given as

$$0 = -\Gamma \vec{v} + \vec{R}(t) - \nabla E \quad (\text{A1.1})$$

^a This derivation was partially written by Mr. Pankaj Singh (Cornell University).

where \vec{v} is the velocity of the particle, Γ is the damping constant, $\vec{R}(t)$ is the random force representing the bead's interaction with the liquid, and E is the potential energy of interaction with other particles. The random force has two properties:

- a) $\langle \vec{R}(t) \rangle = 0$ meaning that the force is completely random in all directions
- b) $\langle \vec{R}(t) \cdot \vec{R}(t') \rangle = c\delta(t - t')$ meaning that the random forces at any two instances are not correlated in time (c is a parameter that will be determined in this derivation)

In order to solve equation (A1.1) for \vec{v} , we find the homogeneous solution of equation (A1.1) to be

$$\vec{v} = \vec{v}_0 e^{-\frac{\Gamma}{m}t} \quad (\text{A1.2})$$

We assume a particular solution of the type

$$\vec{v}_p = e^{-\frac{\Gamma}{m}t} \vec{w}(t) \quad (\text{A1.3})$$

The particular solution is then plugged into equation (A1.3) and integrated to obtain

$$\vec{w}(t) = \frac{1}{m} \int_0^t e^{\frac{\Gamma}{m}\tau} \vec{R}(\tau) d\tau \quad (\text{A1.4})$$

When combined with the homogeneous solution in equation (A1.2), this yields a complete solution of

$$\vec{v} = \vec{v}_0 e^{-\frac{\Gamma}{m}t} + \frac{1}{m} e^{-\frac{\Gamma}{m}t} \int_0^t e^{\frac{\Gamma}{m}\tau} \vec{R}(\tau) d\tau \quad (\text{A1.5})$$

Next we determine the kinetic energy of a particle that, when combined with the two characteristics of the random force, yields

$$KE = \frac{1}{2} m \langle \vec{v} \cdot \vec{v} \rangle = \frac{1}{2} m \left[|\vec{v}_0|^2 e^{-2\frac{\Gamma}{m}t} - \frac{c}{2\Gamma m} e^{-2\frac{\Gamma}{m}t} + \frac{c}{2\Gamma m} \right] \quad (\text{A1.6})$$

At long timespans, equation (A1.6) simplifies to

$$KE = \frac{1}{2} m \langle \vec{v} \cdot \vec{v} \rangle = \frac{c}{4\Gamma} \quad (\text{A1.7})$$

For a particle in three dimensions, the average kinetic energy is $\frac{3}{2} kT$. When this is combined with equation (A1.7), the constant c is determined to be

$$c = 6\Gamma kT \quad (\text{A1.8})$$

When this is combined with the second characteristic of the random force, we get the relation

$$\langle \vec{R}(t) \cdot \vec{R}(t') \rangle = 6\Gamma kT \delta(t - t') \quad (\text{A1.9})$$

In order to determine the relationship between c and the standard deviation of the random force, we do a dimensional analysis for equation (A1.9)

$$\text{LHS} \Rightarrow [\langle \vec{R}(t) \cdot \vec{R}(t') \rangle] = [M^2 L^2 T^{-4}]$$

$$[\Gamma] = [MT^{-1}]$$

$$[kT] = [ML^2 T^{-2}]$$

$$\text{RHS} \Rightarrow \left[\frac{6\Gamma kT}{\Delta t} \right] = [M^2 L^2 T^{-4}]$$

where M is a unit of mass, L is a unit of length, and T is a unit of time. From this dimensional analysis it can be said that in three dimensional space that

$$\vec{R}(t) = \sqrt{\frac{6\Gamma kT}{\Delta t}} \hat{n} \quad (\text{A1.10})$$

where $\sqrt{\frac{6\Gamma kT}{\Delta t}}$ is the standard deviation of the random force.

1.5.2 Derivation of Brownian Dynamics Criteria

In order to determine the conditions for which Brownian Dynamics is valid, we start with a simple system of one bead attached to a spring at 0 K. The Langevin equation can be written as a function of time, t , as

$$m\ddot{x}(t) + \gamma\dot{x}(t) + kx(t) = 0 \quad (\text{A1.11})$$

where m is the mass, $\ddot{x}(t)$ is the acceleration, γ is the coefficient of friction, $\dot{x}(t)$ is the velocity, k is the spring constant, and $x(t)$ is position. The homogeneous solution for equation (1.11) is

$$-m\omega^2 e^{i\omega t} + \gamma i\omega e^{i\omega t} + k e^{i\omega t} = 0 \quad (\text{A1.12})$$

that simplifies to

$$\omega^2 - \frac{\gamma i}{m}\omega + \frac{k}{m} = 0 \quad (\text{A1.13})$$

When equation (A1.13) is solved for ω , we get

$$\omega = \frac{i\gamma}{2m} \pm \frac{\sqrt{-\frac{\gamma^2}{m^2} + \frac{4k}{m}}}{2} \quad (\text{A1.14})$$

The corresponding Brownian equation to equation (A1.11) is

$$\gamma\dot{x}(t) + kx(t) = 0 \quad (\text{A1.15})$$

that does not contain an acceleration term. Therefore, for BD to be valid, according to equation (A1.12), the first term must be negligible. For this to occur, according to equation (A1.14), the condition

$$\frac{\gamma^2}{m^2} \gg \frac{4k}{m} \quad (\text{A1.16})$$

must be satisfied. Under the equation specified in (A1.16), there are two solutions for ω according to equation (A1.14):

$$\omega = 0 \quad (\text{A1.17})$$

$$\omega = \frac{i\gamma}{m} \quad (\text{A1.18})$$

For the condition in equation (A1.17), the acceleration term will become zero. For the condition in equation (A1.18), $e^{i\omega t}$ will decay to zero very quickly, therefore it is negligible. For the SNARE system, typical values are

$$\gamma = 2.295 \times 10^{-11} \frac{kg}{s}$$

$$m = 1.975 \times 10^{-25} kg$$

$$k = 0.1685 \frac{N}{m}$$

When these values are plugged into equation (A1.16), we get

$$\frac{\gamma^2}{m^2} = 1.350 \times 10^{28} s^{-2}$$

$$\frac{4k}{m} = 3.413 \times 10^{24} s^{-2}$$

that satisfies the condition for BD.

1.6 References

1. Nobelprize.org. The 2013 Nobel Prize in Physiology or Medicine - Advanced Information. *Nobel Media AB 2014* (2014). Available at: http://www.nobelprize.org/nobel_prizes/medicine/laureates/2013/advanced.html.
2. Söllner, T., Bennett, M. K., Whiteheart, S. W., Scheller, R. H. & Rothman, J. E. A protein assembly-disassembly pathway in vitro that may correspond to sequential steps of synaptic vesicle docking, activation, and fusion. *Cell* **75**, 409–418 (1993).
3. Rothman, J. E. Mechanisms of intracellular protein transport. *Nature* **372**, 55–63 (1994).
4. Südhof, T. C. The synaptic vesicle cycle: a cascade of protein-protein interactions. *Nature* **375**, 645–653 (1995).
5. Han, X., Wang, C.-T., Bai, J., Chapman, E. R. & Jackson, M. B. Transmembrane segments of syntaxin line the fusion pore of Ca²⁺-triggered exocytosis. *Science* **304**, 289–292 (2004).
6. van den Bogaart, G. & Jahn, R. Counting the SNAREs needed for membrane fusion. *J Mol Cell Biol* **3**, 204–205 (2011).
7. Sinha, R., Ahmed, S., Jahn, R. & Klingauf, J. Two synaptobrevin molecules are sufficient for vesicle fusion in central nervous system synapses. *Proc Natl Acad Sci U S A* **108**, 14318–14323 (2011).
8. Mohrmann, R., de Wit, H., Verhage, M., Neher, E. & Sørensen, J. B. Fast vesicle fusion in living cells requires at least three SNARE complexes. *Science* **330**, 502–505 (2010).

9. Gao, Y. *et al.* Single reconstituted neuronal SNARE complexes zipper in three distinct stages. *Science (80-.)*. **337**, 1340–1343 (2012).
10. Min, D. *et al.* Mechanical unzipping and re-zipping of a single SNARE complex reveals hysteresis as a force-generating mechanism. *Nat Commun* **4**, 1705 (2013).
11. Baker, R. W. & Hughson, F. M. Chaperoning SNARE assembly and disassembly. *Nat. Rev. Mol. Cell Biol.* **17**, 465–479 (2016).
12. Baker, R. W. *et al.* A direct role for the Sec1/Munc18-family protein Vps33 as a template for SNARE assembly. *Science (80-.)*. **349**, 1111–1114 (2015).
13. Ellena, J. F. *et al.* Dynamic structure of lipid-bound synaptobrevin suggests a nucleation-propagation mechanism for trans-SNARE complex formation. *Proc Natl Acad Sci U S A* **106**, 20306–20311 (2009).
14. CDC. 2014 Ebola Outbreak in West Africa. *Centers Dis. Control Prev.* 1 (2014).
15. Moller-Tank, S., Albritton, L. M., Rennert, P. D. & Maury, W. Characterizing functional domains for TIM-mediated enveloped virus entry. *J. Virol.* **88**, 6702–13 (2014).
16. Shell, S. Coarse Graining and Multiscale Techniques. (2009). Available at: <https://engineering.ucsb.edu/~shell/che210d/Multiscale.pdf>.
17. Raabe, D. *et al.* Multi-Scale Modeling in Materials Science and Engineering. Available at: https://www.mpg.de/36458/cpt01_MultiscaleModeling-basetext.pdf.
18. Kubo, R. The fluctuation-dissipation theorem. *Reports on Progress in Physics* **29**, 255–284 (2002).
19. Frankel, D. & Smit, B. *Understanding Molecular Simulation*. (2002).
20. Brady, J. F. & Bossis, G. Stokesian Dynamics. *Annu. Rev. Fluid Mech.* **20**, 118–

157 (1988).

21. Gao, Y. *et al.* Single Reconstituted Neuronal SNARE Complexes Zipper in Three Distinct Stages. *Science* **337**, 1340–1343 (2012).
22. Marko, J. F. & Siggia, E. D. Stretching DNA. *Macromolecules* **28**, 8759–8770 (1995).
23. Bustamante, C., Marko, J. F., Siggia, E. D. & Smith, S. Entropic elasticity of lambda-phage DNA. *Science* **265**, 1599–1600 (1994).

Chapter 2: Coarse-Grained Model of SNARE Mediated Docking^b

Synaptic transmission requires that vesicles filled with neurotransmitter molecules be docked to the plasma membrane by the SNARE protein complex. The SNARE complex applies attractive forces to overcome the long-range repulsion between the vesicle and membrane. To understand how the balance between the attractive and repulsive forces defines the equilibrium docked state we have developed a model that combines the mechanics of vesicle/membrane deformation with a new coarse-grained model of the SNARE complex. The coarse-grained model of the SNARE complex is calibrated by comparison with all-atom molecular dynamics simulations as well as by force measurements in laser tweezer experiments. The model for vesicle/membrane interactions includes the forces produced by membrane deformation and hydration or electrostatic repulsion. Combining these two parts, the coarse-grained model of the SNARE complex with membrane mechanics and electrostatics, we study how the equilibrium docked state varies with the number of SNARE complexes. We find that a single SNARE complex is able to bring a typical synaptic vesicle to within a distance of about 3 nm from the membrane. Further addition of SNARE complexes shortens this distance, but an over-docked state of more than 4-6 SNAREs actually increases the equilibrium distance.

^b This work has been published as: Fortoul, N., Singh, P., Hui, C. Y., Bykhovskaia, M. & Jagota, A. Coarse-grained model of SNARE-mediated docking. *Biophys. J.* **108**, 2258–2269 (2015). Copyright permissions were obtained prior to the submission of this document.

2.1 Introduction

The SNARE (soluble NSF-attachment protein receptors) ^{1,2} complexes are the core protein machinery involved in synaptic vesicle docking and fusion. SNARE proteins form a link between vesicles and the plasma membrane, providing a mechanism for zippering the two together. The transmembrane vesicle associated protein synaptobrevin (Syb or v-SNARE) forms a four-helical bundle with the proteins SNAP-25 and the transmembrane protein syntaxin (Syx), which are attached to the neuronal plasma membrane and termed the “t-SNARE”. SNAP-25 contributes two helices (SN1 and SN2) to the bundle, while both Syx and Syb contribute one helix each ^{3,4}. During exocytosis the vesicles are first tethered or targeted towards the plasma membrane ($>25\text{nm}$ ⁵), then they are docked at the plasma membrane with the help of the adhesive forces provided by SNAREs. After docking, priming occurs which finally leads up to vesicle to membrane fusion ¹. The zippering of the SNARE bundle is thought to provide the necessary force to bring the vesicle in proximity to the plasma membrane by overcoming the hydration or electrostatic repulsion between the two.

The process of synaptic vesicle docking and fusion can be viewed as deformation of a mechanical system, in which a synaptic vesicle, a nearly spherical lipid bilayer shell, is brought in proximity to the plasma membrane, a nearly flat lipid bilayer, under the influence of the attractive forces exerted by the SNARE complex. Key structural characteristics of the SNARE bundle have been determined experimentally, including its x-ray crystal structure⁶ and the location of the layers thought to be essential to SNARE's function⁷, which has been confirmed through single molecule force experiments⁸. All-atom

simulations have been performed to analyze the structural aspects of the SNARE bundle including detailed interactions between the different helices⁹ as well as to investigate the effects of oxidation and reduction of the SNAP25 linker domain on the formation of the SNARE bundle¹⁰. Some all-atom simulation work has been done on the unzipping of the SNARE bundle¹¹, however, time constraints prevent simulations for large displacements and longer time scales. In an effort to overcome timescale limitations, some coarse-grained (CG) simulations have been performed^{12,13}. Force-fields for CG simulations have been developed¹⁴. However, to suit a wide range of applications, these force fields still need to be refined¹⁵. Relatively little has been done on coupling the SNARE unzipping process to the vesicle-plasma membrane behavior to address questions including that of how docking depends on the number of SNAREs. This problem is difficult because it must capture large length scale deformations and electrostatics in the vesicle-plasma membrane system as well as amino acid-level chemical specificity that are essential to the functioning of the SNARE bundle.

There is significant debate about how many SNARE complexes are required to make synaptic fusion happen. Earlier studies suggested that 5 to 8 SNARE complexes form the fusion pore¹⁶. However, recent studies suggest a smaller number of SNARE complexes. Thus, it was suggested recently that a single SNARE complex can trigger fusion,¹⁷ while stating the fact that the fusion rate increases with the number of SNARE's. In¹⁸, it has been proposed that two Syb units are required for fusion, based on fluorescence response of tagged Syb. The work done in¹⁹ suggests that three SNARE units are needed to carry out the fusion, on the basis of fusion rate. At the same time, studies performed on model systems *in vitro* suggest numbers ranging between 5-11²⁰.

To investigate how the number of SNARE complexes affects vesicle docking, we developed a continuum model of the lipid bilayers and combined it with a CG model for the SNARE which includes chemical specificity. Specifically, the proteins in the SNARE bundle are represented by an alpha-carbon based CG model that includes both structural and chemical specificity by employing an elastic network model (ENM)^{21,22} and Miyazawa and Jernigan (MJ) contact energies²³⁻²⁵, respectively. The SNARE CG model is calibrated to match the peak unzipping force determined by Gao et al.⁸, and is used to calculate a force displacement curve for the unzipping process, along with snapshots of corresponding structures that provide information about the unzipping pathway. The continuum model for bilayer deformation^c is based on lipid membrane theory developed in Jenkins et al.²⁶ and is an extension of work done in Long et al.²⁷. It computes the force required to counter the vesicle-membrane repulsion, bringing the vesicle to a given distance from the membrane while taking full account of the vesicle and membrane deformation. Balancing the SNARE-induced attraction against the vesicle-membrane hydration or electrostatic repulsion provides us with information about the equilibrium gap between the two membranes for a given number of SNAREs. Based on this information we study the effect of the number of SNAREs from the point of view of the mechanics of the process.

^c The continuum model for bilayer deformation was developed by Mr. Pankaj Singh (Cornell University).

2.2 Materials and Methods

2.2.1 All Atom Simulations

We conducted all-atom molecular simulations of SNARE helices in order to obtain some of the parameters for the SNARE CG model. AA simulations of the four individual helices as well as the full SNARE bundle were performed using the GROMACS molecular simulation package²⁸ and the CHARMM22 forcefield²⁹. The starting structures for the 4 individual helices and the full SNARE bundle were extracted from the final timestep of a 40 ns AA simulation with initial configuration given by the high resolution x-ray structure 1N7S^{7,11}. (See Appendix for a discussion.) For each set of runs, the corresponding structure was solvated in a waterbox (70 Å x 150 Å x 70 Å), and potassium ions were added to neutralize the overall charge. Additional potassium and chloride ions were added so that there was a 150mM concentration of KCl to mimic physiological conditions³⁰. All bonds were constrained. Dynamics were run at 300 K first using an NVT ensemble for 100 ps followed by NPT for 100 ps using the Parrinello-Rahman barostat. Five sets of 40 ns-long runs were conducted with a timestep of 2 fs for Syb, Syx, SN1, SN2, and the SNARE bundle. Computations were performed at the Texas Advanced Computing Center (TACC) through XSEDE resources.

2.2.2 SNARE Coarse-Grained Model

A principal result of this work is the development of a CG model for the SNARE complex. Our goal has been to make it as simple as possible while still retaining the identity of

individual residues. As shown in Fig. 2.1A, in our SNARE model every residue is represented by a bead located at the alpha carbon of that residue.

The size and mass of each bead are equivalent to the Van der Waals radius³¹ and mass³¹ of the bead's corresponding residue. Two major types of interactions were accounted for in this CG model, those within individual helices and those between them. An elastic network model (ENM)^{21,22} is used to represent the intra-helical bonds and interactions that maintain the individual helical structure as shown in Fig. 2.1A. Pairs of beads within the cutoff distance, R_c , on the same helix are said to be “in contact” and are connected by a harmonic spring with the energy potential

$$u_{spring} = \frac{1}{2} k_s (r - r_0)^2 \quad (2.1)$$

where k_s is the spring constant, r is the distance between the two beads, and r_0 is the natural length of the spring. From the 40 ns long individual helix AA simulations, it was observed that the natural state of each individual helix was a relatively straight conformation compared to the helices in the SNARE x-ray crystal structure. (The mean curvature of the helices in the SNARE bundle (3.11×10^7 1/m) is three times as large as that of the individual helices (1.03×10^7 1/m), see Appendix). Because these straightened-out conformations represent the ‘natural’ or relaxed state of the helices, they were used to construct the ENM. This is important because, as the helices unzip from the main bundle and break their helix-helix contacts, they revert back to their natural straight conformation, releasing elastic energy.

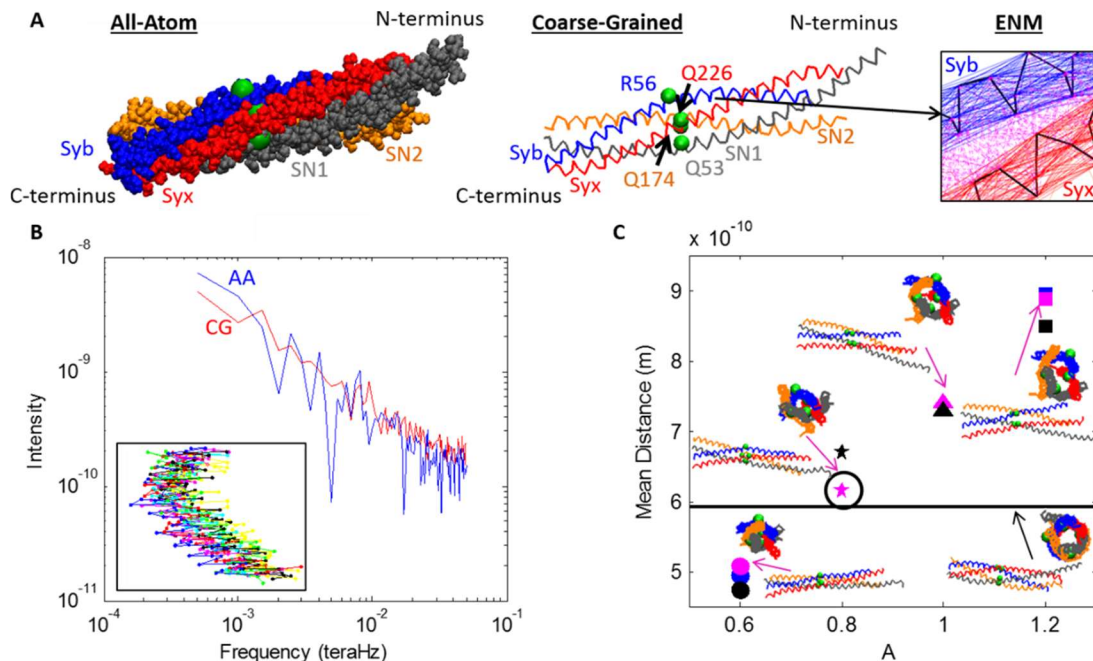


Figure 2.1 (A) The AA (*left*) and CG (*middle*) representations of the SNARE bundle are shown. Both models include helices Syb, Syx, SN1, and SN2 with each helix contributing one residue to the ionic layer (*beads*): R56, Q226, Q53, and Q174 respectively. The C-terminal ends of Syb and Syx play an integral role in the fusion process in that they attach to the vesicle (Syb) and plasma membrane (Syx). The ENM spring network (*right*) that maintains the individual helical structure is shown for Syb and Syx where the thick lines represents the $C\alpha$ backbones and the thin lines represent ENM springs. The Miyazawa and Jernigan contacts between Syb and Syx are also represented (*dotted lines*). (B) The spectra used to compare the fluctuations of the AA and CG models are shown for Syb. Values for k_s of 0.0963 N/m and R_c of 20 Å were used for the CG model. The inset shows 10 snapshots of Syb during the corresponding AA simulation. (C) Mean distance for different values of parameter A along with snapshots of the SNARE bundle. The original crystal is represented by the black line. The version chosen for simulation is marked by the black circle.

The values of k_s for the ENM were chosen by matching the spectrum of fluctuations of the AA simulations and the CG model for each helix independently. For the analysis of individual AA helix simulations, the positions of the alpha carbons were extracted every 10 ps. For each alpha carbon a time series of distance from its average location was calculated. The fast Fourier transform (FFT) was then computed for each bead's time series

and averaged over all beads, yielding a single spectrum per helix. In order to make this comparison of the fluctuations, CG simulations were conducted for the 4 individual helices using Langevin dynamics at 300 K for a range of values of k_s . (Details on numerical implementation of the CG simulation are provided in Appendix.) The same FFT analysis was conducted for individual helix CG simulations as for the AA simulations. The time length of simulations required was determined by conducting a normal modes analysis (NMA) on the CG model of the crystal structure, 1N7S, for all helices individually using different values of k_s . AA simulations were run for 2 ns, which is considerably longer than the characteristic time given as the inverse of the lowest natural frequency (See Table A2.1 in Appendix). In order to best match the fluctuations, the root mean squared deviation (RMSD) between the AA and CG spectra was found for each run. An example of the comparison of both spectra is shown in Fig. 2.1B for Syb with k_s value of 0.0963 N/m. For all helices k_s was varied between 0.00009 N/m and 0.4816 N/m and the resulting RMSD for all values of k_s are shown in the Appendix. Based on these data, a value of 0.0963 N/m was chosen for k_s for all four helices.

The second main category of interactions in the CG model is helix-helix interactions that require chemical specificity. These interactions are implemented by utilizing Miyazawa and Jernigan (MJ) contact energies that provide a scalable reference for residue-residue interactions²³⁻²⁵. Any beads on separate helices interact if they are within the MJ cutoff distance, R_{c_MJ} . To avoid checking the distance between every bead during every timestep, a neighborlist is built every 1000 steps. Any beads on different helices that are

within $1.5 * R_{c_MJ}$ of each other are added to the neighborlist. Contacts are determined from the pairs already chosen by the neighborlist.

Following Kim and Hummer³², the interaction energy ε_{ij} between residues i and j of the SNARE structure is scaled from the Miyazawa and Jernigan contact energies e_{ij} ³².

$$\varepsilon_{ij} = \lambda(e_{ij} - e_0) \quad (2.2)$$

Note that there is no self-interaction, i.e., equation (2.2) applies only for $i \neq j$. Also, these interactions operate only between residues on different helices, intra-helical interactions being already represented by the ENM. There are two tunable parameters, a scaling parameter, λ , and a shifting parameter, e_0 . Throughout the tuning of parameters, e_0 was set to 0. Although it was available as an extra parameter, it was not found necessary to match the SNARE structure and hence was not used in order to minimize the number of adjustable parameters.

Forces corresponding to the MJ contact energies are implemented using a slightly modified 6-12 LJ potential. The format of this potential varies depending on whether there is attraction or repulsion between these residues as well as if the distance between beads is greater than or less than that the distance at which the potential minimum occurs, r_{ij}^0 . The sign of ε_{ij} determines whether the interaction between the residues is attractive (negative) or repulsive (positive). The modified Lennard Jones potentials³² are

If $\varepsilon_{ij} < 0$:

$$u_{ij}(r) = 4|\varepsilon_{ij}| \left[\left(\frac{\sigma_{ij}}{r} \right)^{12} - \left(\frac{\sigma_{ij}}{r} \right)^6 \right] \quad (2.3)$$

If $\varepsilon_{ij} > 0$ & $r < r_{ij}^0$

$$u_{ij}(r) = 4|\varepsilon_{ij}| \left[\left(\frac{\sigma_{ij}}{r} \right)^{12} - \left(\frac{\sigma_{ij}}{r} \right)^6 \right] + 2\varepsilon_{ij} \quad (2.4)$$

If $\varepsilon_{ij} > 0$ & $r \geq r_{ij}^0$:

$$u_{ij}(r) = -4|\varepsilon_{ij}| \left[\left(\frac{\sigma_{ij}}{r} \right)^{12} - \left(\frac{\sigma_{ij}}{r} \right)^6 \right] \quad (2.5)$$

where r is the distance between the two beads and σ_{ij} is the interaction radii. Equation (2.4) contains a shift in the potential that ensures that repulsive pairs of beads will always repel each other.

The interaction radii is defined as the average of the Van der Waals radii of residues i and j

$$\sigma_{ij} = A * \frac{\sigma_i + \sigma_j}{2} \quad (2.6)$$

where A is available as a tuning parameter and σ_i and σ_j are the Van der Waals radii of residues i and j . In order to match both CG and AA behavior and structure, A was adjusted to match the SNARE bundle width, defined as the diameter of the tube shaped space inside the bundle that can be seen if one looks along the center axis of SNARE. The reference bundle width was found by computing the mean distance of all of the nearest MJ contacts from the SNARE crystal structure determined from 1N7S. These 21 nearest contacts represent the distances between the inner residues of the bundle and therefore the bundle width. Fig. 2.1C shows the mean distance for a few cases. The value of A is directly related to bundle width, and from Fig. 2.1C we chose a value of A as 0.8 to produce a

similar mean bundle width to the crystal structure. This value of A corresponds to interaction radii ranging from 3.6 Å for Gly-Gly and 5.44 Å for Trp-Trp³².

The remaining parameter, λ , controls the strength of inter-helical interactions and was determined by calibrating the results of simulated force-extension behavior of the SNARE complex by the recent experimental study by Gao et al.⁸, which provided characteristic forces for the unzipping of the 4 helix SNARE bundle pulled apart in an optical tweezer experiment. The value of λ was calibrated to match the measured peak force of 14 to 19 pN (specifically, 17.2 pN). For our unzipping simulation the C-terminal residues of Syx and Syb were each attached to a fixed bead by a spring with a spring constant k_{spb} . Displacement control was used on the bead attached to the C-terminal Syb bead as opposed to the actual Syb C-terminal bead in order to allow for rotation of the SNARE bundle. In order to see how much the orientation of the pulling force on the SNARE matters, the simulations were performed in two ways: by applying a displacement to pulling beads attached to Syb89 and Syx256 through a spring (as shown in the manuscript) and by directly applying displacements to Syb89 and Syx256. (The pulling beads allow for rotation of the SNARE bundle during the simulation and are hence less restrictive.) The results of these simulations were quite similar. To mimic the experimental setup in which the N-termini of Syx and Syb are connected, a FENE bond connecting the N-terminal residues of Syb and Syx was incorporated in the model to represent the additional residues and the N-terminal disulfide bridge that Gao et al.'s⁸ experiment included. The potentials used to implement the FENE bond are

If $r(t) < r_{c_FENE}$:

$$u_{FENE}(t) = -\frac{1}{2}k_F r_0^2 \ln\left(1 - \left(\frac{r(t) - \Delta}{r_0}\right)^2\right) \quad (2.7)$$

If $r(t) \geq r_{c_FENE}$:

$$u_{FENE}(t) = -\frac{1}{2}k_F (r(t) - \Delta)^2 \quad (2.8)$$

where r is the distance between two bonds at t , r_0 is the maximum bond length, Δ is the resting bond length or, in this case, the original distance between the two beads³³, and r_{c_FENE} is $0.9 * \Delta$. The value of r_0 was determined by the number of residues that the spring represents, 8 for Syb and 5 for Syx, times the maximum extension per residue, 3.65 \AA ⁸. The FENE spring constant, k_F , used was the same as k_s for the ENM of 0.0963 N/m .

Before beginning the CG displacement control simulations, the SNARE structure was relaxed for 10^6 timesteps under quasi-static conditions, i.e., at 0 Kelvin. This relaxation was performed on the SNARE structure extracted from the final timestep of the 40 ns AA simulation in order to ensure that the initial structure was fully equilibrated. After this relaxation period, the C-terminal beads were separated under displacement control using the two pulling beads that were discussed previously. The bead attached to the Syx C-terminus was held fixed, and all displacements were applied to the bead attached to the C-terminal Syb bead. For each displacement, this bead was moved 1 \AA along the vector between the two pulling beads. After each displacement was applied, the structure was relaxed for 10^5 timesteps in order to allow it to equilibrate. At the end of the relaxation period, the forces on both pulling beads were nearly identical, and these forces were recorded as a function of displacement (See Fig. A2.4 in Appendix).

Displacement control runs were conducted with eleven different values of λ between 0.16 and 0.72. This parameter directly adjusted the magnitude of the force, so it was used to match the peak unzipping force reported by Gao et al.⁸ of between 14 pN and 19 pN. On this basis, a value of 0.3 was chosen to produce a peak force in the experimentally measured range of 17.2 pN.

2.2.3 Continuum Model of the Vesicle and Plasma Membrane^d

The vesicle and plasma membrane are subjected to forces from the SNARE complex drawing them together and distributed distance-dependent electrostatic and hydration repulsion. During this process, the vesicle and plasma membrane both deform considerably and the task of the continuum model is to obtain a consistent solution of the deformed shape subject to these forces. The continuum calculations are based on the formulation of Jenkins et al.²⁶ and its extension to SNARE-mediated fusion by Long et al.²⁷. The current axisymmetric continuum model extends these formulations to include concentrated forces due to the SNARE molecules and the electrostatic forces due to the charges on the membranes or hydration repulsion.

The axisymmetric geometry is shown schematically in Fig. 2.2. We use a cylindrical coordinate system (r, θ, z) where θ is the angle of revolution about the z axis. Owing to the axisymmetric assumption, the forces exerted by the zipping of the SNARE complexes are represented by a circle of line force of magnitude F on a spherical vesicle of radius R

^d Work involving the continuum model of the vesicle and plasma membrane was done by Mr. Pankaj Singh (Cornell University).

(see Fig. 2.2B) as well as on the plasma membrane. This line force counters the repulsive forces between the vesicle and the plasma membrane. As shown in Fig. 2.2B, the line force acts along a latitude of the undeformed vesicle and is constrained to remain normal to the deformed surface. The location of the latitude is specified by the arc length S_0 of a cross-section in the reference configuration, which is taken to be a spherical vesicle. Because the plasma membrane is very large compared to the vesicle radius, its reference configuration is taken to be a flat circular membrane of radius L under pretension, T_0 . The SNARE forces act on a circle of radius S_0 in the reference configuration, have the same magnitude F , and are always directed opposite to the force on the vesicle (Fig. 2.2B and C).

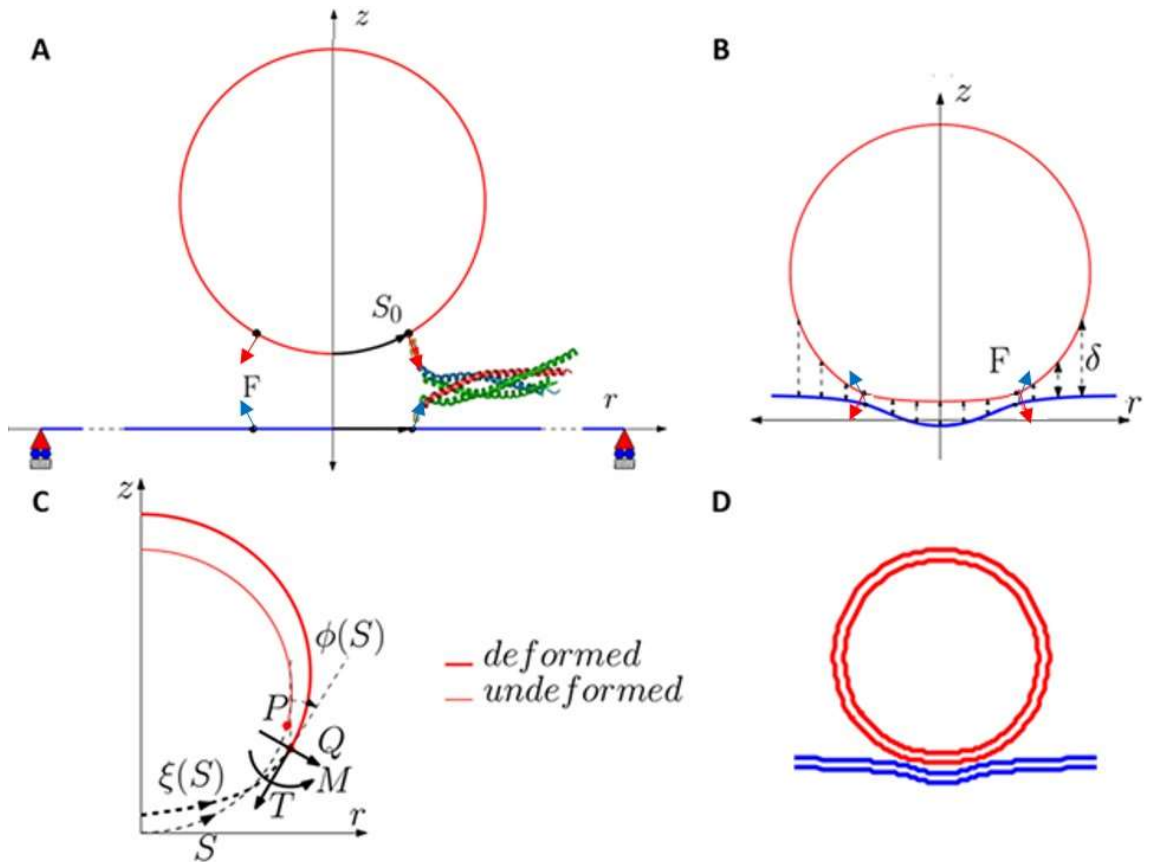


Figure 2.2 (A) A schematic of the axisymmetric model in the undeformed configuration, showing the location of SNARE and direction of force applied. (B) The repulsive forces (shown by the dotted lines) act on the deformed configuration of the vesicle as does the SNARE force, F . (C) The figure shows the convention for shear force (Q), in-plane tension (T), and moment (M) acting on the cross-section of the membrane a location $\xi(S)$, where $\phi(S)$ is the tangent angle in the undeformed configuration measured from the vertical. (D) Example of a deformed vesicle-plasma membrane complex for a 20-nm diameter vesicle docked by 15 SNAREs.

In our model, the repulsive force depends only on the local separation δ , as shown schematically in Fig. 2.2. Following Bykhovskaia et al.¹¹, electrostatic and hydration repulsion between the vesicle and plasma membrane are calculated using Derjaguin's approximation³⁴ in which interaction between curved surfaces is estimated assuming that the surfaces are locally flat. This approximation is valid if the length scale over which

forces decay is much smaller than the radius of curvature of the vesicle. The applicable range of separations prior to vesicle to membrane fusion is 2-4 nm. In this range, the principal repulsive forces are due to electrostatics and hydration.

The functional form of both the electrostatic and hydration repulsion is approximately the same, an exponential decay. Electrostatics has the large decay length (typically 1 nm under physiological conditions) and smaller prefactor³⁵. The decay length for hydration repulsion is in the 1-4 Å range³⁵⁻³⁸. Consequently, hydration dominates for small separation and electrostatics for larger separation. Much of the previous work suggests that the cross-over distance beyond which electrostatics dominates is about 1.5 nm^{35,37}. However, recent work of Aeffner et al.³⁶ suggests that hydration repulsion exceeds electrostatic repulsion for distances upto about 3 nm. Based on the work of Aeffner et al.³⁶, we have performed calculations taking hydration repulsion to be the dominant repulsive interaction. However, given some uncertainty regarding the relative importance of electrostatics and hydration, we have also computed results for the case where electrostatic repulsion is assumed to dominate. The hydration pressure takes on the form of an exponential decay:

$$P(d_w) = P_0 \exp(-d_w / \lambda_h) \quad (2.9)$$

where d_w is the lipid bilayer separation, P_0 is the hydration pressure amplitude, and λ_h is the decay length. According to Aeffner et al.³⁶, the prefactor, P_0 , ranges from 0.24 – 4.13 GPa and λ_h ranges from 2.3 – 3.7 Å. We chose to use a value of 0.43 GPa for P_0 and a λ_h of 3.22 Å based on the parameters suggested for a synaptic vesicle corresponding to experiments performed in a physiologically relevant DOPC/Chol 70:30 mixture³⁶.

Local electrostatic interaction is determined by solving the Debye-Huckel equation for two infinite parallel planes separated by δ . We consider two limiting scenarios,

1) The membranes have fixed charge density throughout the process of docking. This corresponds to the case when the lipid molecules are completely ionized and have a fixed charge.

2) The membranes have fixed surface potential. This is achieved by adjusting the surface charge density of the ions in the Stern layer of the membrane or by varying the degree of ionization of the polarizable lipid molecules.

For the constant surface charge densities, the repulsive force along the z direction per unit area is given by

$$F_e = \frac{\sigma_1^2 + \sigma_2^2 + 2\sigma_1\sigma_2 \cosh(\delta/l_D)}{2\epsilon\epsilon_0 \sinh^2(\delta/l_D)} \quad (2.10)$$

where σ_1 and σ_2 are the surface charge densities of the vesicle and neuron base respectively, l_D is the Debye length, ϵ is the relative permittivity of water and ϵ_0 is the permittivity of vacuum. The choice of surface charge σ_1 is based on the electrophoretic measurement by Ohsawa et al.³⁹ and force-displacement measurement by Marra et al.³⁸. The reported value of surface charge is in the range 0.01 – 0.03 C/m². Also, assuming the same surface charge density on the outer leaflet of the plasma membrane and based on the observation by Pekker et al.⁴⁰ that a charge density difference of only ~ 0.0001 C/m² between the inner and outer leaflet is necessary to maintain the resting potential difference of 70 mV for the neuron cell, we choose the value of $\sigma_1 = \sigma_2 = -0.025$ C/m².

For the case of constant surface potential, the force per unit area is

$$F_e = \frac{l_D^2}{2\epsilon\epsilon_0} \frac{-\varphi_1^2 - \varphi_2^2 + 2\varphi_1\varphi_2 \cosh(\delta/l_D)}{\sinh^2(\delta/l_D)}. \quad (2.11)$$

When the two membrane structures are far away from each other, they have charge density given as $\sigma_1 = \sigma_2 = -0.025C/m^2$. The potential on an isolated surface and charge density are related by,

$$\varphi = \frac{l_D\sigma}{\epsilon\epsilon_0} \quad (2.12)$$

The value of surface potential for the bilayers $\varphi_1 = \varphi_2 = -25\text{mV}$, is evaluated using equation 2.12. As the vesicle approaches the membrane, the surface potential is held constant and equation 2.11 is used to obtain the force between the membranes. A similar approach was followed in ¹¹. However, in that work the mechanics of SNARE opening was not coupled to the electrostatic repulsion, and the SNARE-end opening was picked at 1 nm, whereas here the minimum separation of SNARE-ends is taken to be 2 nm. Primarily for this reason, the repulsive electrostatic forces in the present work are in the range of tens of pN instead of the hundreds of pN quoted in ¹¹. Relevant parameters for modeling electrostatic forces are listed in Table A2.3 (Appendix).

2.2.4 Governing Equations for the Continuum Membrane Model and Their Solution

The vesicle-membrane system has been modeled under axisymmetry in an (r, θ, z) coordinate system. In the undeformed configuration, the vesicle is modeled as a sphere with radius R , whereas the undeformed plasma membrane is a circular disc of radius $L \gg R$. As shown in Fig. 2.2, S refers to the undeformed arc length, whereas in the

deformed configuration, the arc length is denoted by ξ . The tangent to the membrane makes an angle ϕ with the z axis and the mean curvature of the membrane surfaces is denoted by H .

The forces in the membranes are shear force, Q , and the in-plane tension, T , as shown in Fig. 2.2C. The osmotic pressure inside the synaptic vesicle is represented by p_0 . As shown in Fig. 2.2B, the repulsive electrostatic force per unit area, F_e in equations (2.9) and (2.10), acts on both membranes, along the z direction. The force due to SNARE bundles is represented as line loads acting on the circles over the undeformed geometry of vesicle and plasma membrane (denoted by vectors F and $-F$, as shown in Fig. 2.2B). On the vesicle, the radius of this circle, r_0 , is determined by the geometrical compatibility condition which is based on the width of SNARE helix, d , and number of SNARE bundles, as,

$$r_0 = \frac{(\text{number of SNAREs}) \times d}{2\pi}. \quad (2.13)$$

The assumption here is that the packing of SNAREs is limited by steric hindrance between them and equation (2.13) represents the smallest radius that would accommodate the given number of bundles. The equivalent arc length value for load application is given by $S_0 = \sin^{-1}(r_0/R)$. This arc length is same for both the vesicle and the membrane.

We assume that the strain energy density W of both membranes is given by,

$$W = cH^2, \quad (2.14)$$

and by variation of total energy, the governing equations for the vesicle-membrane system are obtained in Eqs. S11. These equations represent equilibrium in the normal (equation.

A2.11a) and tangential (equation. A2.11f) directions at each point on the membranes. The geometrical constraints can be used to obtain equation. A2.11b-e. These governing equations form a non-linear system of ODE's. By specifying the input geometric parameters (R, L) and the force parameters $(F, S_0, F_e$ and $p_0)$, this system of ordinary differential equations (ODE's) can be solved numerically to obtain an equilibrium configuration of the membrane system. We use the non-linear boundary value problem solver `bvp4c` in MATLAB© to solve the ODE's.

2.3 Results

2.3.1 Force-Displacement Response of the Vesicle-Membrane Interaction

The equal and opposite forces on the Syx and Syb C-termini are transmitted to the plasma membrane and vesicle, respectively, as forces attracting the two together. Below separations separations of ~ 2.5 nm attractive forces are resisted primarily by hydration repulsion. A characteristic force-separation curve can be obtained for the vesicle-membrane system using the formulation described in section 2.2.3. By specifying the number of SNARE bundles attached to the vesicle-membrane system, the location of the line load can be determined using equation (2.13). The effect of zipping of SNARE bundle is simulated by varying the strength of the line load in small steps. For each increment in force, an equilibrium configuration of the membrane system is obtained, and hence we determine the separation between the two load points on vesicle and plasma membrane, respectively. This separation is the distance between residues Syb89 and Syx256. By

varying the number of SNAREs, a series of force-separation curves can be obtained as shown in Fig. 2.3A.

2.3.2 SNARE Force-Separation Curve

Fig. 2.3B shows the results of a simulation in which the SNARE bundle has been pulled apart for a total end-to-end separation of 20 nm between the C-terminal Syb and Syx end beads.

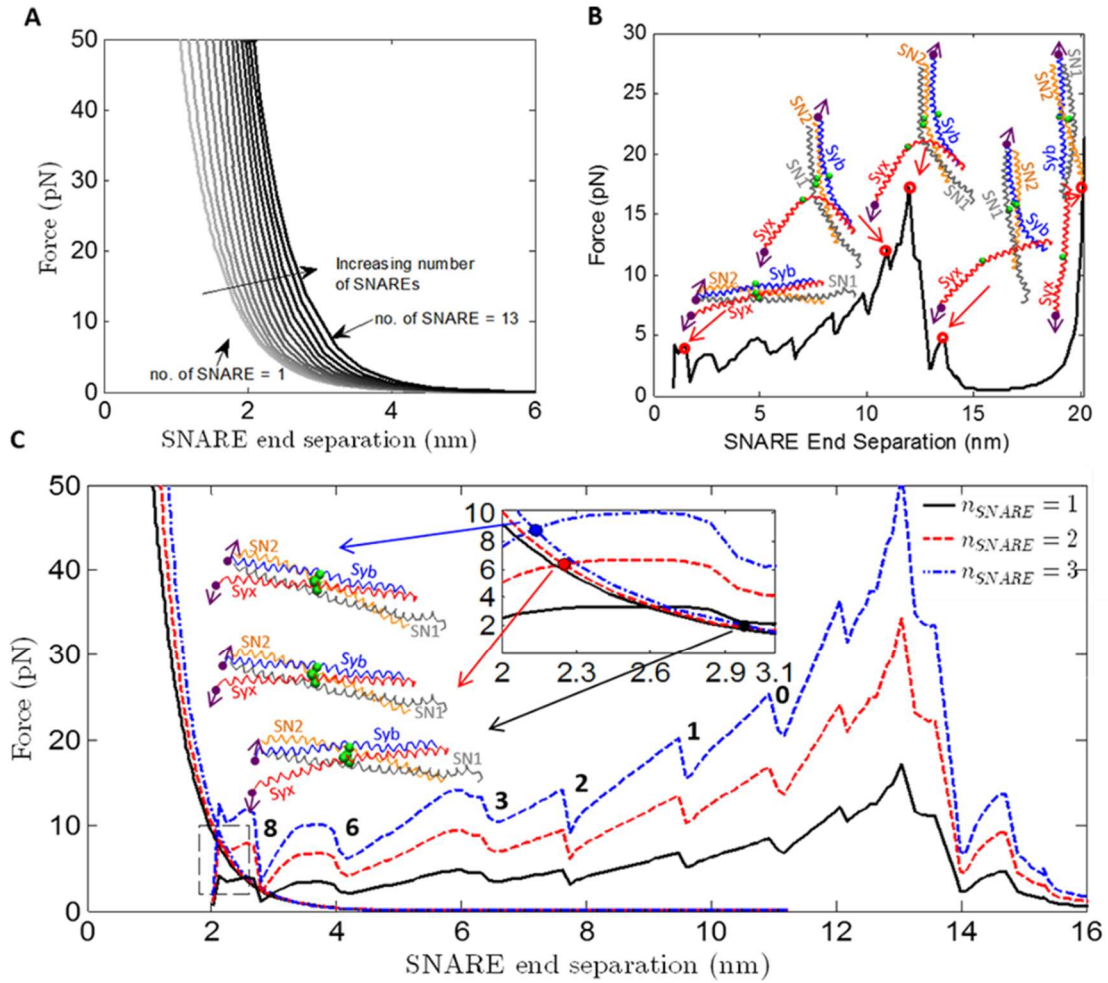


Figure 2.3 (A) Force versus SNARE end separation for the vesicle-membrane system for different numbers of SNAREs for the hydration repulsion case. (B) The force during separation of the ends of the SNARE bundle using λ of 0.30 for the CG model of SNARE along with snapshots of the SNARE bundle at the corresponding C-terminal end separation. The end separation is defined as the distance between the Syb and Syx C-terminal beads. Syb, Syx, the ionic layer residues (*beads*), and the C-terminal residues (*beads with arrows*) that are attached to pulling beads are shown in each SNARE snapshot. The purple arrows correspond to the direction along which the C-terminal beads are being pulled. (C) The force as a function of Syb-Syx C-terminal distance is shown for the vesicle-membrane (the exponentially decreasing curves) and SNARE. One (*solid line*), two (*dash line*), and three (*dash-dot line*) SNAREs are shown in this plot. Intersections between the vesicle-membrane and SNARE force-displacement responses represent equilibrium states. There are a number of instabilities represented by load-drops. These correspond to separation of individual layers and have been so labeled.

Each drop in the force-displacement plot (Fig. 2.3B) represents the system overcoming a barrier where there is a strong interaction between the SNARE bundles. Two examples are the snapshots at 10.9 nm and 11.9 nm in Fig. 2.3B. With an increase of only 1.0 nm in displacement and little visible change in structure there is a significant (5.1 pN) increase in force to a peak value of 17.2 pN, after which the force immediately drops to about 2 pN. (Because a significant amount of the linker domain was not present in the crystal structure of SNARE that was used to build the CG model, the first force jump seen by Gao et al.⁸ at 3 nm and 8-13 pN is not present in these results.) The CG model is able to capture the experimentally determined precipitous force-drop after which the remaining interactions holding the SNARE bundle together are relatively weak and are therefore not measurable in a force-controlled experiment. The subsequent increase in force is associated with stretching of the linkage between the N termini of Syx and Syb, and presumably would not be present in a physiological setting. It is included here because this feature is also present in the experiments of Gao et al.⁸. For simplicity, in the version of the elastic network model used here, we do not allow the helices to unravel, justified by the following facts. As the results of the next section show, the equilibrium separation for all the cases studied in this paper is about 3 nm or less. At these separations the force on each SNARE is < 5 pN. Based on the work of Gao et al.⁴¹ the first unwinding event occurs at ~10-12 pN. Thus our simplifying assumption (which will be relaxed in future work) that helices remain unfolded is justifiable for the range of openings and displacements representative of the equilibrium docked state. We have checked the sensitivity of our results to this assumption by allowing small portions of the unzipped region to unfold as shown in Appendix.

2.3.3 Combined SNARE and Vesicle-Membrane Results

In the previous two sections we have independently obtained force-separation results for the vesicle-membrane system (Fig. 2.3A) and for the SNARE (Fig. 2.3B). Before combining the two results, we first accounted for the fact that the distance between outer surfaces of the membranes is larger by about 2 nm than the distance between Syb89 and Syx256, the SNARE residues that we move apart (see Appendix). Specifically, we shifted the SNARE force displacement curve to the right by 2 nm in order to obtain this consistency. Clearly, in the combined SNARE-vesicle-membrane system there is a single force and corresponding displacement. Applying this consistency condition between the two results determines equilibrium. Moreover, we can determine how equilibrium depends on the **number** of SNARES.

For systems with 1, 2, and 3 SNAREs, the information from Fig. 2.3A and Fig. 2.3B is combined to produce Fig. 2.3C. Because it has been shown that SNAREs mediate vesicle to membrane fusion in a synchronous way, we assume that the force required to unzip two SNAREs would simply be twice the force required to unzip one SNARE, and so on^{42,43}. In all three cases, the curves intersect at an equilibrium SNARE end separation of between 2 nm and 3 nm suggesting that even 1-3 SNAREs are sufficient to overcome hydration repulsion and allow the vesicle to dock at the plasma membrane. The corresponding structures for the intersection points for all three cases, shown in Fig. 2.3C, also suggest there is no important conformational difference between the three structures other than a difference in the number of residues that have been unzipped.

It is instructive next to consider the energy landscape corresponding to the force-separation results shown in Fig. 2.3. For this purpose, the SNARE (positive) and vesicle-membrane (negative) force-separation results are integrated numerically. Fig. 2.4B shows the results corresponding to the force-separation results shown in Fig. 2.3. Note that because the SNARE force-displacement response contains unstable jumps, the entire energy landscape is not represented in Figs. 2.4B-C. Because of the nature of the displacement control simulations, there are several instabilities present in the original SNARE force separation curve. An example of one of these instabilities is the drop at 7.5 nm as shown in the SNARE curves in Fig. 2.3C. Integrating across these instabilities makes the total energy of the system slightly more negative than it should be (see Appendix). Figs. 2.4B-C show contour plots of interaction energy as a function of the number of SNAREs and end-to-end separation. Fig. 2.4B shows the results for a vesicle with radius of 20 nm, representing a synaptic vesicle. The gray circles represent the global energy minimum for each value of number of SNAREs, corresponding to force equilibria in Fig. 2.3. An example of how these minima were determined is shown in Fig. 2.4A that was used to determine the global energy minimum for 1 SNARE for the hydration repulsion case. It is striking that a single SNARE produces a distinct energy minimum at ~ 3 nm. As the number of SNAREs increases to 4 SNAREs the equilibrium SNARE end separation decreases. For 4-8 SNAREs there is little difference in the equilibrium separation. For 5 SNAREs the total energy per SNARE is ~ -17 kT which is quite consistent with the 13 – 27 kT range reported by Zorman et al.⁴⁴. With increase in the number of SNAREs over 8, the equilibrium SNARE separation slowly increases; the minimum separation (~ 2.1 nm) is achieved with 4 bundles. Thus, we may conclude that 4-8 SNAREs

are sufficient to complete the zippering process and to bring the membrane and the vesicle at a distance of 2.1 nm. Importantly, a larger number of SNARE bundles does not bring the vesicle closer to the membrane, because steric hindrance pushes them out to a larger radius.

We next explored how electrostatics would affect the vesicle to plasma membrane repulsion. We recalculated the continuum model results using a fixed surface charge of -0.025 C/m^2 on the vesicle and the membrane with electrostatic repulsion as shown in Fig. A2.9B. For this case for one SNARE the end separation is $\sim 2.4 \text{ nm}$ which is smaller than the 3 nm seen for the hydration repulsion case. However, when more than one SNARE is added to the system, the equilibrium SNARE end separation is constant at $\sim 2 \text{ nm}$ for 2-13 SNAREs. In this case, the equilibrium configuration of the SNARE bundle would be a nearly completely zipped conformation. For this case with 4 SNAREs the total energy per SNARE is $\sim -14 \text{ kT}$ which again within the range of 13 – 27 kT reported by Zorman et al.⁴⁴.

We next explored how the vesicle size would affect the number of SNAREs required to dock a vesicle to the membrane. Figs. A2.10 *B* and *D* show the results for the case of a vesicle that is 100 nm in radius, corresponding to vesicles in neurosecretory cells. For the hydration repulsion case, there is a considerable difference between the 20nm and 100nm vesicles. For the 100nm case the minimum separation is also reached with 4 SNAREs, however that minimum separation is $\sim 2.5 \text{ nm}$ as opposed to $\sim 2.1 \text{ nm}$ for the 20nm vesicle. For the case of electrostatic repulsion with a constant surface charge, the only difference between the two cases is for 1 and 2 SNAREs. For the 100nm vesicle case the equilibrium separation is $\sim 3.4 \text{ nm}$ as opposed to $\sim 2.4 \text{ nm}$ for the 20nm vesicle. Additionally for 2

SNAREs there is also a larger separation for the 100nm vesicle of 3nm as opposed to 2nm for the 20nm vesicle. However for 3 or more SNAREs there is little difference between the two vesicle sizes because both SNARE configurations are nearly completely zippered.

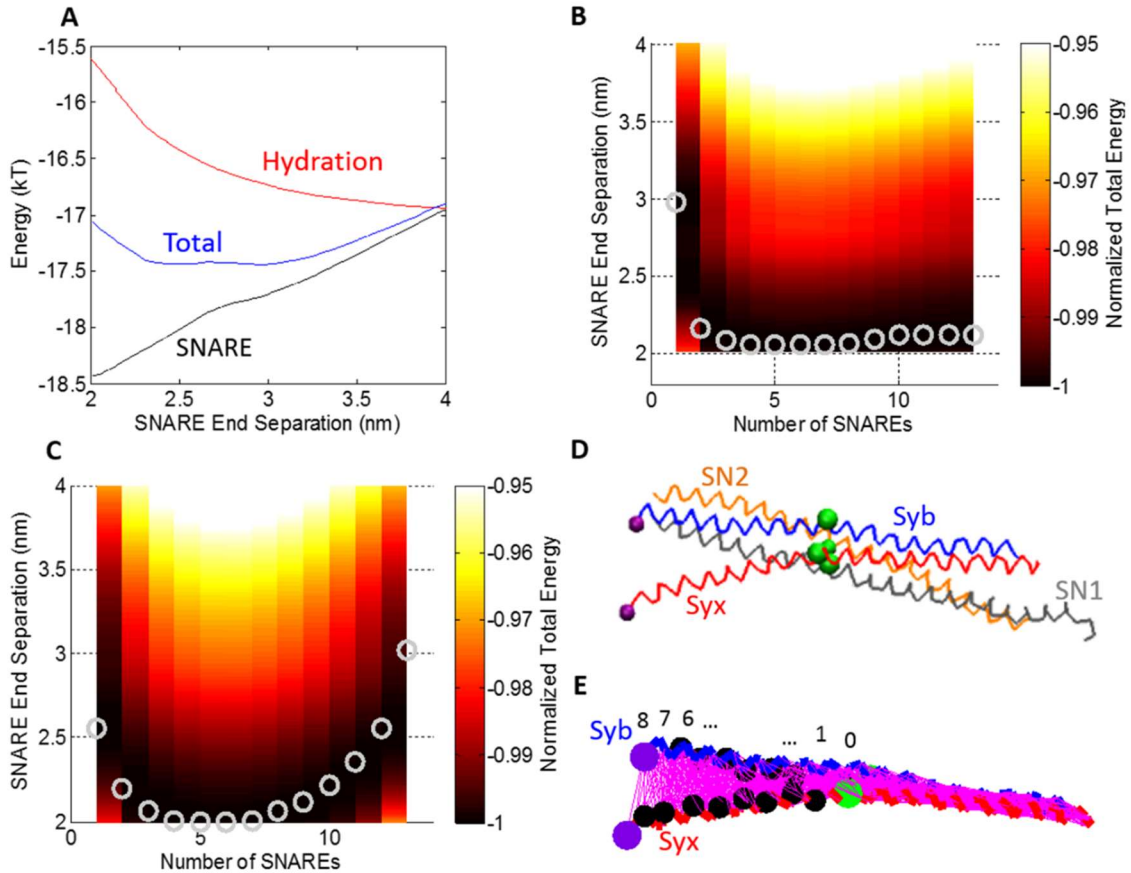


Figure 2.4 (A) Energy as a function of SNARE end separation when repulsion between the vesicle and plasma membrane is dominated by hydration repulsion. The energetic contributions from SNARE (attractive), hydration (repulsive), and the total (their sum) are shown. The hydration repulsion has been shifted vertically by -17 kT for clarity. (B) Contour plot of total energy as a function of SNARE end separation distance for different numbers of SNAREs under hydration repulsion. Circles correspond to global energy minima representing the equilibrium SNARE end separation for a given number of SNAREs. Vesicle radius is 20 nm. (C) Contour plot of total energy as a function of SNARE end separation distance for different numbers of SNAREs under electrostatic repulsion for a fixed charge of -0.025 C/m^2 on the vesicle and the membrane in the limit of high tension in the vesicle and plasma membrane. For this case, minimum lateral separation between the SNARE bundles has been increased from 3 nm to 4nm. (D) The structure of SNARE corresponding to the case shown in Fig. 4 B, number of SNAREs=1. Syb, Syx, SN1, SN2

are shown with the ionic layer residues indicated as large beads. (E) The same structure as in Fig. 4 D but showing only Syb and Syx for clarity. All contacts for residues within 2σ of each other are indicated with thin lines.

Fig. 2.4B and C represent results for an optimized set of parameters describing molecular details and electrostatic forces. To judge the robustness of the conclusions gleaned from these results, we explored several variations of parameters including (1) allowing a portion of Syb to melt with the surface charge held constant, (2) holding the surface potential constant instead of surface charge, (3) high osmotic pressure in the vesicle and low pretension in the plasma membrane, and (4) the limit of high tension in both the vesicle and plasma membranes. These variations in the modeling assumptions generally make little difference in the conclusions drawn from Fig. 2.4 (see Appendix for details). The main conclusion that 4-8 SNAREs bring the vesicle to the minimum distance away from the membrane still holds. Because the equilibria of interest for the problem addressed in this work occur at relatively small separation and forces, in our model we have not allowed the helices to unravel. In order to see the potential effect of unraveling, the first two helical turns of Syb were melted and the force displacement curve for SNARE was calculated from Fig. 2.3B. The resulting energy surface for this case for a 20 nm vesicle with hydration repulsion is shown in Fig. A2.11 A. 4-10 SNAREs brings the vesicle within a minimal distance of the plasma membrane. However, that minimal distance is ~ 2.4 nm as opposed to the ~ 2.1 nm for the case where Syb is not permitted to unravel.

In an effort to compare to the experimental prefusion structures of the vesicle and plasma membrane as shown by Malsam et al.⁴⁵ and Hernandez et al.⁴⁶, the continuum model was calculated using high osmotic pressure in the vesicle and low pretension in the

plasma membrane. However, the resulting energy surface for this modification to the base cases shown in Fig. 2.4 has little effect on the results because the repulsive force is dominated by hydrostatic repulsion as shown in Fig. A2.14.

The limit of high tension in both the vesicle and plasma membrane was studied using an analytical model described in the Appendix. In order to test the sensitivity of the solution to the location of the SNAREs, calculated using equation (2.13), the diameter of the SNARE bundle was varied from 2 nm, Fig. A2.17 A, to 4nm, whereas the base case used 3nm. This variation seems to have the most significant effect on the solution. Decreasing the size of the SNARE bundle still yields similar results in that for more than one SNARE the bundle is nearly completely zipped shut. On the other hand when the size of the SNARE bundle is increased, instead of having a nearly fully zippered bundle, there is a minimum separation that occurs at 4 SNAREs. With the addition of more than 5 SNAREs the equilibrium separation again begins to increase all the way up to ~3nm with 13 SNAREs.

Fig. 2.4D and E show the equilibrium structures of SNARE at a 2.1 nm separation for the case shown in Fig. 2.4B. SN1 and SN2 were removed from the structure for clarity in Fig. 2.4E, and the residues of Syb and Syx that were “in contact” were determined. Because the Miyazawa and Jernigan forces greatly decrease after a separation of $\sim 2^* \sigma$, that distance was used as the criteria for 2 residues being in contact. At the start of the displacement control simulation, Syb and Syx had 574 contacts between them. After a 2.1 nm separation, only 449 contacts remained. The removed contacts begin to create a crack-like defect separating the helices. After the 2.1 nm separation, residues 89 (Trp) of Syb and

256 (Lys) of Syx were still in contact. These residues are still far away from the ionic layer showing that the SNARE bundle had not yet unzipped to that point.

2.4 Discussion and Conclusion

The docking of vesicles onto the plasma membrane of a neuron involves interplay between the SNARE complexes that provide attractive forces, long-range repulsion between the vesicle and membrane, and deformation of all three components. Although each of these components has previously been investigated in detail, to understand the biophysics and mechanics of vesicle docking it is imperative to combine them. We report here the first model which couples chemical specificity of the SNARE complex with hydration, electrostatic, and mechanical forces imposed on the vesicle and plasma membrane. Such a model can serve as a tool to investigate how mutations in the SNARE complex could affect the docking and fusion process.

We have developed separate coarse-grained models for the deformation of the SNARE complex and of the vesicle-membrane assembly. The vesicle-membrane model is based on a continuum description of membrane deformation subjected to either hydration or electrostatic repulsion and forces from the SNARE complexes. The fusion of lipid bilayers have been extensively modeled⁴⁷ to capture the intermediate states of fusion, including stalk formation, and to understand their energetics. Our goal in this study was to understand the forces produced by membrane bending and hydration or electrostatic repulsion that need to be overcome by the SNARE complexes to dock a vesicle to the membrane. The continuum membrane model was coupled with a coarse grain model of the SNARE

complex. The SNARE forces are represented in the continuum membrane model as an axisymmetric line force, an assumption that is increasingly accurate for increasing number of SNAREs. (A single SNARE at the axis of symmetry also presumably results in axisymmetric deformations of the vesicle/membrane.) For a given number of SNAREs, the model holds fixed their anchor points in the vesicle and plasma membrane. This constraint potentially affects our results. However, we note that the position of the SNARE anchor points does vary as we change the number of SNAREs (equation (2.13)). The number of SNAREs was varied from 1-13. Usually, for 2 or more SNAREs there is little difference in the equilibrium separation, suggesting that the model results probably will not vary much if we remove the constraint of holding the positions fixed.

The CG SNARE model is based on an elastic-network representation of each of the helices combined with Miyazawa-Jernigan potentials to capture inter-helical interactions. It is a minimalistic model that still represents residue-specificity. Its few parameters are calibrated either by comparison with all-atom MD simulations of individual SNAREs, or by comparison to experimentally measured forces to separate a single SNARE complex, Gao et al.⁸ Specifically, we match the experimentally observed peak force of 17.2 pN force. Each of the two models separately yields a force-separation relationship. Enforcing consistency between the two yields equilibrium configurations for the SNARE-vesicle-membrane complex, for a given number of SNAREs.

As the first application of our model, we explored here the effect of the number of SNARE complexes on the mechanics of vesicle docking and the prefusion state of the SNARE complex. It is still a matter of debate as to how many SNARE complexes need to assemble prior to the fusion process. High concentration of Syb on the vesicle (~70

copies⁴⁸), as well t-SNARE clusters at docking sites⁴⁹ suggest that *in vivo* fusion may be mediated by multiple SNARE complexes. At the same time, experiments and model systems suggest that one⁵⁰, two¹⁸, or three^{19,51,52} could be sufficient. Other studies, however, suggest a larger number of SNARE complexes per fusion, ranging between 5 and 11^{16,20,53}. Finally, recent studies suggest that the number of assembled SNARE complexes may determine the release efficiency⁵⁴ and that it may vary⁵⁵. Thus, how vesicle docking might depend on the number of SNARE complexes remains an open question, previously not addressed from the biophysical and biomechanical point of view.

We find that one SNARE complex is sufficient to dock the vesicle onto the membrane. As few as 2-3 SNAREs are sufficient to bring the distance between the membrane and vesicle to the minimum and thus to complete the docking process. Interestingly, there is a point of diminishing returns such that a larger number of SNAREs (i.e., an over-docked state) does not further reduce the vesicle-membrane separation. The corresponding predicted SNARE end-to-end separation is in the range 2-3 nm^{56,57} but one can expect significant fluctuation about the equilibrium state because the energy profile is relatively shallow (Fig. 2.4A). This picture of a partially zippered docked state is consistent with the conclusions of an *in-vivo* toxin cleavage assay in crayfish neuromuscular junctions. In this work, we only model docking, not fusion. That is, we calculate the equilibrium separation between the vesicle and plasma membrane during docking. The lower bound of ~2 nm separation between the vesicle and plasma membrane is based on the steric hindrance of having to fit the SNARE bundles between the two surfaces. This distance is probably a bit too large for fusion to occur, which suggests that some additional mechanism other than SNARE zippering must act for fusion.

Several variations in the model including calculations under fixed charge, fixed surface potential, high vesicle pressure and high membrane tension, and varying vesicle radius have all shown similar results.

Our results are consistent with the view that a pre-fusion state involves a partially assembled SNARE complex⁵⁸⁻⁶⁰ which keeps the vesicle at a short distance from the plasma membrane in anticipation of Ca^{2+} -induced fusion rather than the alternative view that SNARE zippering represents a final step of exocytosis and rapidly progresses once nucleated⁶¹. Specifically, our model robustly predicts an equilibrium separation between the vesicle and the membrane to be on the order of 2.0-3.0 nm corresponding to opening of at most layer 8.

2.5 Appendix

2.5.1 Coarse-Grained Simulations: Solution Procedure

CG simulations were conducted for the 4 individual helices using Langevin dynamics at 300 K for a range of values of k_s . The Langevin equation⁶² includes an inertial term, a viscous term, a random force term, and a potential energy term, respectively, in the form

$$m\ddot{x}(t) = -\gamma\dot{x}(t) + R(t) - \nabla E \quad (\text{A2.1})$$

where m is the mass of each bead, $\ddot{x}(t)$ is the bead's acceleration at time t , γ is the damping constant, $\dot{x}(t)$ is the bead's velocity at t , $R(t)$ is a random force that represents the protein's interaction with the surrounding fluid, and E is the potential energy governing the solute

that includes ENM forces. The fluctuation-dissipation theorem⁶³ connects the random force and viscous drag

$$\langle R(t) \cdot R(t') \rangle = 6\gamma k_B T \delta(t - t') \quad (\text{A2.2})$$

where k_B is Boltzman's constant, T is temperature, $R(t')$ is the random force applied at t' , and $\delta(t - t')$ is the Dirac delta function. Written as a system of equations for all beads, the Langevin equation takes the form

$$[M]\{\ddot{u}(t)\} = -\gamma\{\dot{u}(t)\} + \{R(t)\} - [k]\{u(t)\} \quad (\text{A2.3})$$

where $[M]$ is a diagonal mass matrix, $\{\ddot{u}(t)\}$, $\{\dot{u}(t)\}$, and $\{u(t)\}$ are column vectors containing the accelerations, velocities, and positions in the x, y, and z directions for each bead, $\{R(t)\}$ is a column vector containing the random force in the x, y, and z directions for each bead, and $[k]$ is a stiffness matrix.

The standard deviation of the random force is derived from equations (A2.2) and (A2.3) to be

$$SD = \sqrt{\frac{2m\gamma k_B T}{\Delta t}} \quad (\text{A2.4})$$

where Δt is the timestep. The friction coefficient is dependent on the bead type as well

$$\gamma = \frac{6\pi\eta a}{m} \quad (\text{A2.5})$$

where a is the Van der Waals radius of the bead and η is the viscosity of water. The timestep used for Langevin dynamics was based on the characteristic time, τ , that is defined as

$$\tau = \sqrt{\frac{m}{k_s}} \quad (\text{A2.6})$$

where m is the maximum bead mass. The timestep was adjusted to match the diffusion of a bead attached to a spring. Using this technique, the timestep was determined to be 43.4 fs or $\tau/20$.

In order to model the dynamics of the coarse-grained model, the Langevin dynamics equation was solved using a generalized Verlet algorithm ⁶²

$$\dot{x}^{n+1/2} = \dot{x}^n + m^{-1} \frac{\Delta t}{2} \left[-\nabla E(x^n) - \gamma M \dot{x}^n + R^n \right] \quad (\text{A2.7})$$

$$x^{n+1} = x^n + \Delta t \dot{x}^{n+1/2} \quad (\text{A2.8})$$

$$\dot{x}^{n+1} = \dot{x}^{n+1/2} + m^{-1} \frac{\Delta t}{2} \left[-\nabla E(x^{n+1}) - \gamma M \dot{x}^{n+1} + R^{n+1} \right] \quad (\text{A2.9})$$

where n is the timestep. The position is calculated from the half velocity, and then the position and half velocity are both used to calculate the full velocity.

2.5.2 ENM Reference State

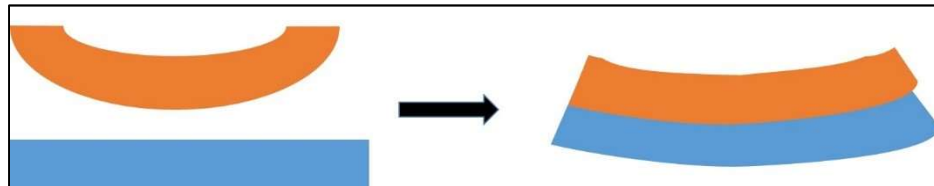


Figure A 2.1 A model showing two beams. The reference or zero energy state for both beams is when they are separated from each other. When the beams form a bundle, mutual interactions deform them into some shape with associated stored energy that will be released when the beams are separated.

For each of the helices there exists a relaxed, natural, or reference state, and we maintain that the relaxed state of the springs that comprise the elastic network model should be defined in this reference state. This idea is illustrated in the figure above. Say we have

two helices (orange and blue) with two different reference states (bent and straight). When the two helices come into contact with each other, they will both deform to form an equilibrium structure. If we assume the energy of the system to be 0 on the left, some energy is required to bend both helices to form the combined structure on the right. In our model we use our reference states, like those on the left, to help us calculate the energy stored in the bundle that can be released as the bundle is pulled apart.

The existence of such a reference state is not contingent upon its viability as a stable state for an actual isolated helix. Although Syb by itself is largely unstructured, we can still define the Syb helix by itself, i.e., removed from the other SNARE helices. It is a notional state used merely to obtain the frozen or stored elastic energy in the SNARE bundle. That is, all that is required is that the helical forms be stable as a bundle and that we have a systematic procedure by which to define springs on a relaxed state, again, regardless of whether the relaxed state actually exists.

We recognize that in many sources in the literature it is noted that Syb is largely unstructured when not in the presence of the SNARE bundle. We conducted 40 ns all-atom simulation of the individual SNARE helices, starting with a configuration extracted from the crystal structure. We found that this timescale was more than sufficient to allow all of the helices to straighten into relatively straight rod-like conformations. It was also short enough that each rod retained its helical structure. Because of this separation of time scales – time to relax an individual helix \ll time required for it to lose its structure – we were able to define the natural or reference state of each helix on which to construct the elastic spring network.

2.5.3 Determining the Cut-Off Distance and Spring Constant in the Elastic Network Model for SNARES

Coordinates from the straightened out helical structures were extracted from the individual AA simulations, and the connectivity and natural length of the ENM springs for each helix were determined based on these structures. If the cutoff distance is too small, the proteins will denature. If it is too large, simulation speed will be compromised with no significant improvement in representation. In order to find an optimal value, this distance was adjusted and a histogram was created for each helix to show the total number of springs that were connected to each bead. The minimum criterion for the number of springs was that each bead should be connected by a spring to all of its nearest neighbors. It was concluded that a cutoff distance of a minimum of 10 Å yielded at least 4 springs per bead, which satisfied this criteria. After further investigation, it was determined that R_c was required to be at least 20 Å in order to maintain the helical structure of each helix during AA simulations. The histogram for the final value of R_c , 20 Å, for the helix Syb is shown in Fig. A2.2. The histograms for the other three helices are similar.

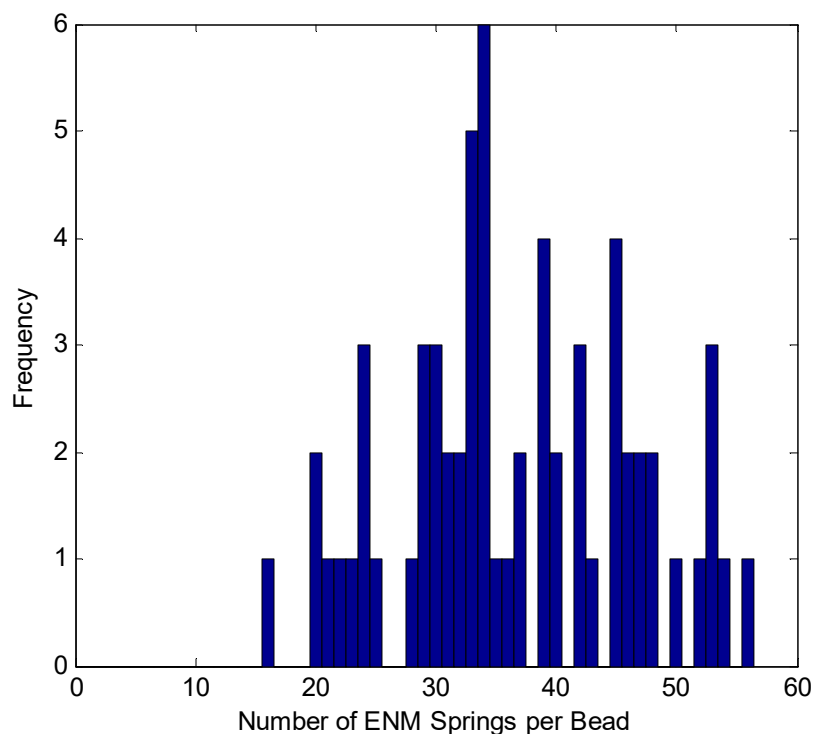


Figure A 2.2 A histogram for the number of ENM springs per bead is shown for Syb with a value of 20 Å for R_c .

The values of k_s for the ENM were chosen by matching the spectrum of fluctuations of the AA simulations and the CG model. For the analysis of individual AA helix simulations, the positions of the alpha carbons were extracted every 10 ps. For each alpha carbon a time series of distance from average location was calculated. The fast Fourier transform (FFT) was then evaluated for each bead's time series. The average was taken over all beads yielding a single spectrum per helix. In order to make this comparison of the fluctuations, CG simulations were conducted for the 4 individual helices using Langevin dynamics at 300 K for a range of values of k_s . The time length of simulations required was determined by conducting a normal modes analysis (NMA) on the CG model of the crystal structure,

1N7S, for all helices individually using different values of k_s . AA simulations were run for 2 ns, which is considerably longer than the characteristic time given as the inverse of the lowest natural frequency. The results for Syb are shown in Table S1.

Table A 2.1 The lowest natural frequencies and characteristic times for Syb determined are shown below for different values of k_s

k_s (N/m)	Lowest Natural Frequency Squared (1/ns) ²	Time (ns)
0.0963	4.53	4.70E-01
0.1926	9.05	3.32E-01
0.2889	1.36	2.71E-01
0.3853	1.81	2.35E-01
0.4816	2.26	2.10E-01

For Syb, as was seen for all helices, the characteristic times are significantly less than 1 ns. As a result the AA simulations were analyzed for the first 2 ns of the trajectories, and the CG test simulations were conducted for 2 ns and analyzed with data collected every 2 ps. In order to best match the fluctuations, the root mean squared deviation (RMSD) between the AA and CG spectra was found for each run. An example of the comparison of both spectra is shown in Fig. A2.3 for Syb with k_s value of 0.0963 N/m. The RMSD for all helices for all values of k_s are shown in Table A2.2 with the minimum RMSD values shaded in grey.

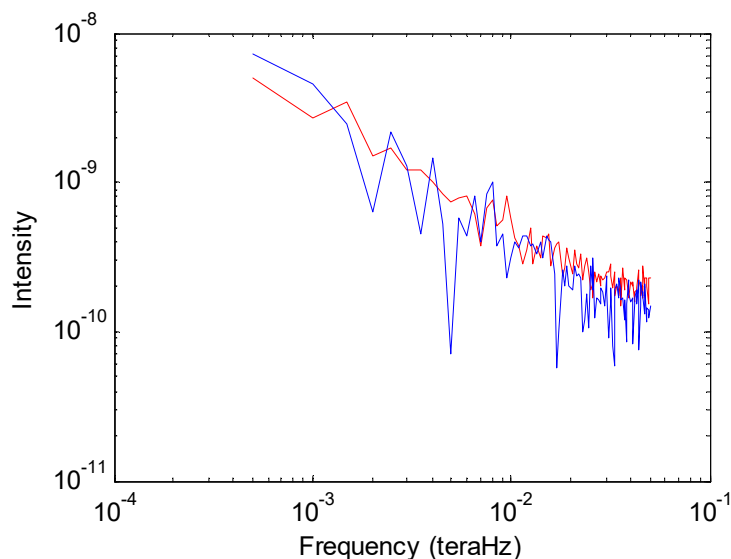


Figure A 2.3 The spectra used to compare the fluctuations of the AA (*blue*) and CG (*red*) models are shown for Syb for 2 ns. Values of k_s as 0.0963 N/m and R_c of 20 Å were used for the CG model. An RMSD of 4.7E-10 was found.

Table A 2.2 The RMSD values between the AA and CG fluctuation spectra are shown below for all helices for a range of values of k_s . The minimum RMSD values are shaded in grey.

k_s (N/m)	Syb RMSD	Syx RMSD	SN1 RMSD	SN2 RMSD
0.0001	9.6450e-09	1.0532e-08	1.2658e-08	9.5905e-09
0.0009	4.9432e-09	5.5075e-09	6.7327e-09	4.6640e-09
0.0096	1.4341e-09	1.1056e-09	1.5941e-09	1.7538e-09
0.0481	7.4334e-10	1.4651e-09	8.5729e-10	1.6778e-09
0.0963	4.7077e-10	4.3346e-10	1.3671e-09	2.3080e-09
0.1444	7.2271e-10	9.9229e-10	1.5680e-09	1.1604e-09
0.1926	1.4341e-09	1.1064e-09	1.5941e-09	1.7539e-09
0.2889	1.2019e-09	1.5654e-09	2.7382e-09	3.0644e-09
0.3853	1.7372e-09	2.0310e-09	3.2207e-09	3.3413e-09
0.4816	2.4969e-09	2.8429e-09	3.2951e-09	3.5652e-09

Based on the data in Table S2, a value of 0.0963 N/m was chosen for k_s for all four helices.

For Syb and Syx, this corresponds to the value of k_s with the smallest RMSD. For SN1 and

SN2 however, the minimum RMSD occurs either a little above or below k_s of 0.0963 N/m. Because the RMSD is still very small for these two helices with that value of k_s , it was chosen to use a consistent value of k_s for all helices.

2.5.4 Calibration of λ and Displacement Orientation

As described in the SNARE CG model portion in the methods section, the value of λ was adjusted in order to match the peak force reported by Gao et al. ⁸ of 14 – 19 pN. We conducted a series of displacement control simulations at 0K for a set of λ values ranging from 0.30 to 0.72. Displacement was applied in steps and the system allowed to relax. Relaxation to equilibrium was monitored by tracking the forces acting on the C-terminal beads of Syb and Syx as shown in Fig. A2.4. Each force spike corresponds to a displacement being applied to the C-terminal bead of Syb. After 10^5 timesteps, both forces relax to nearly the same value, which is taken as the equilibrium force for that displacement, and the next displacement step is then applied.

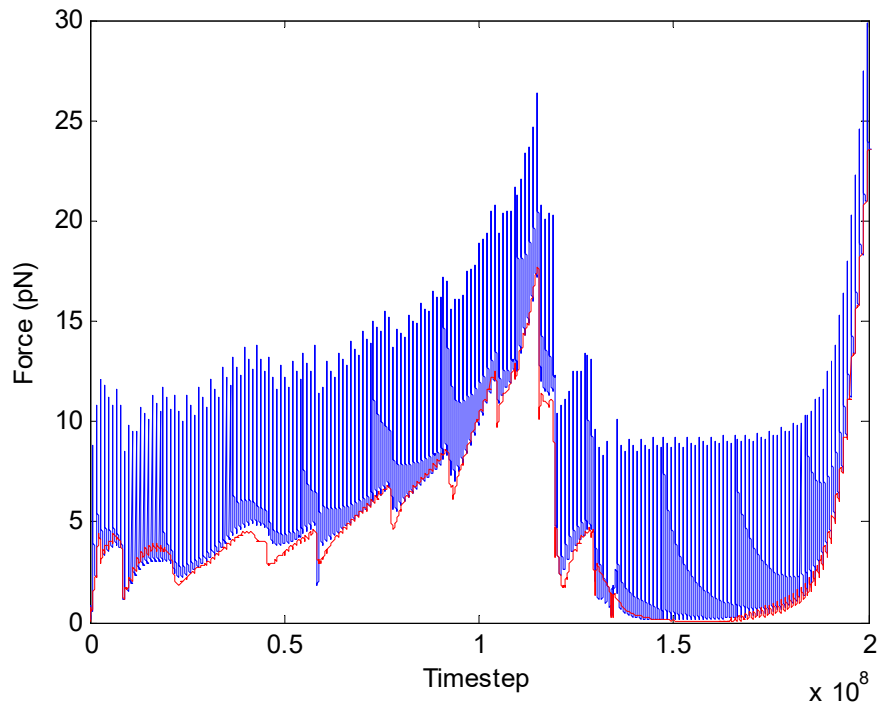


Figure A 2.4 The force as a function of timestep is shown for a displacement control run with λ set to 0.30. The forces on the C-terminal beads of Syb (*blue*) and Syx (*red*) are shown. Each spike in the Syb force corresponds to application of a new displacement step. A total displacement of 20 nm is shown.

The resulting force displacement curves for a few of these runs for varying λ are shown in Fig. A2.5.

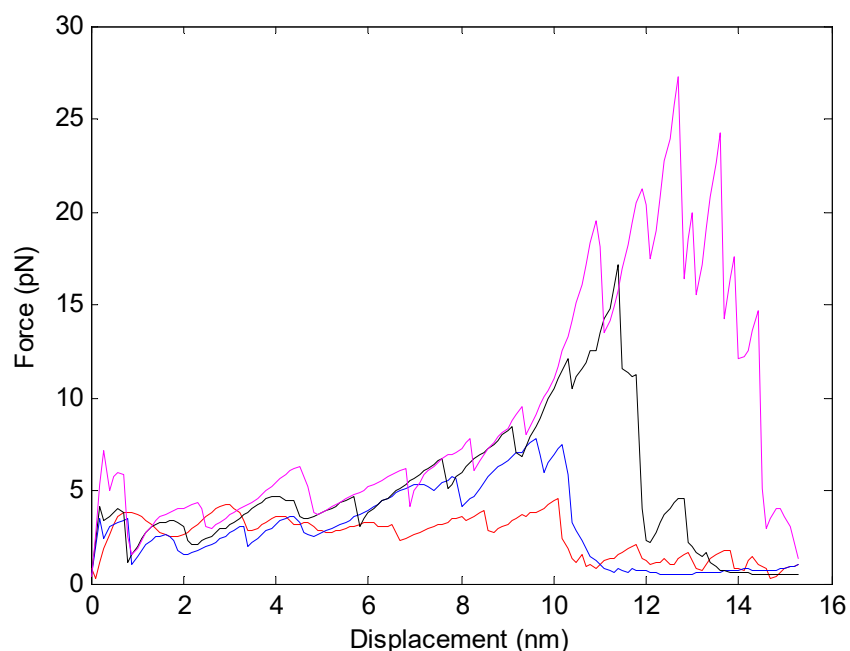


Figure A 2.5 Force displacement curves are shown for displacement control simulations done using λ values of 0.16 (*red*), 0.24 (*blue*), 0.30 (*black*), and 0.40 (*magenta*).

It was clear that as λ was increased, the peak force increased as well. By choosing its value to be 0.3, we attained a peak force of 17.2 pN that lies in the experimentally measured range.

2.5.5 SNARE Force Displacement Instabilities and Their Effect on Energy

There are several mechanical instabilities in the force-separation curve of the SNARE, for example at 7.5 nm in Fig. 2.3C. These usually correspond to “breaking” of one of the layers. When the system jumps from one stable point to the next, it does not follow the equilibrium force-separation relationship between these two points; instead, it lies above it. When we integrate the force-separation curve to obtain energies, we consequently

compute a slightly larger magnitude (more negative) than it should be. This does not affect any of the predictions about stable equilibria.

2.5.6 Continuum Governing Equations and Their Solution^e

The axisymmetric deformation of the vesicle-membrane system can be reduced to the solution of a set of ordinary differential equations. The undeformed configuration of the vesicle is a sphere of radius R with arc-length in a cross-section denoted by S whereas, the plasma membrane occupies the interior of a circle of radius $L > R$. We introduce the notation ϕ to denote the angle made by the tangent to a point on the cross-section of the deformed membrane in the (r, z) plane with the z axis (see Fig. A2.5 A). Briefly, the equations describing the deformation involve the shear force Q , the angle ϕ , the mean curvature H , the deformed arc length ξ , the deformed coordinates of a generic material point (r, z) which has an arc length coordinate S in the undeformed configuration. To expedite the analysis, we introduce the following normalized variables:

$$\begin{aligned} \bar{S} &= \frac{S}{R}, \quad \bar{r} = \frac{r}{R}, \quad \bar{z} = \frac{z}{R}, \quad \bar{H} = RH, \quad \bar{\xi} = \frac{\xi}{R}, \\ \bar{Q} &= \frac{QR^2}{c}, \quad \bar{d} = \frac{dR^2}{c}, \\ \bar{p}_0 &= \frac{p_0 R^3}{c}, \quad \bar{F}_e = \frac{F_e R^3}{c}, \quad \bar{F}_n = \frac{F_n R^3}{c}, \quad \bar{F}_t = \frac{F_t R^3}{c}, \end{aligned} \tag{A2.10}$$

where,

^e This work was done by Mr. Pankaj Singh.

p_0 is the osmotic pressure of the vesicle,

d is an integration constant resulting from integrating the tangential force equilibrium equation (see the Appendix for details),

F_e is the electrostatic force per unit area of the membrane and is always along z direction,

F_t is the tangential component of the concentrated load at the material point S_0 in the deformed membrane,

F_n is the normal component of the concentrated load at the material point S_0 deformed membrane.

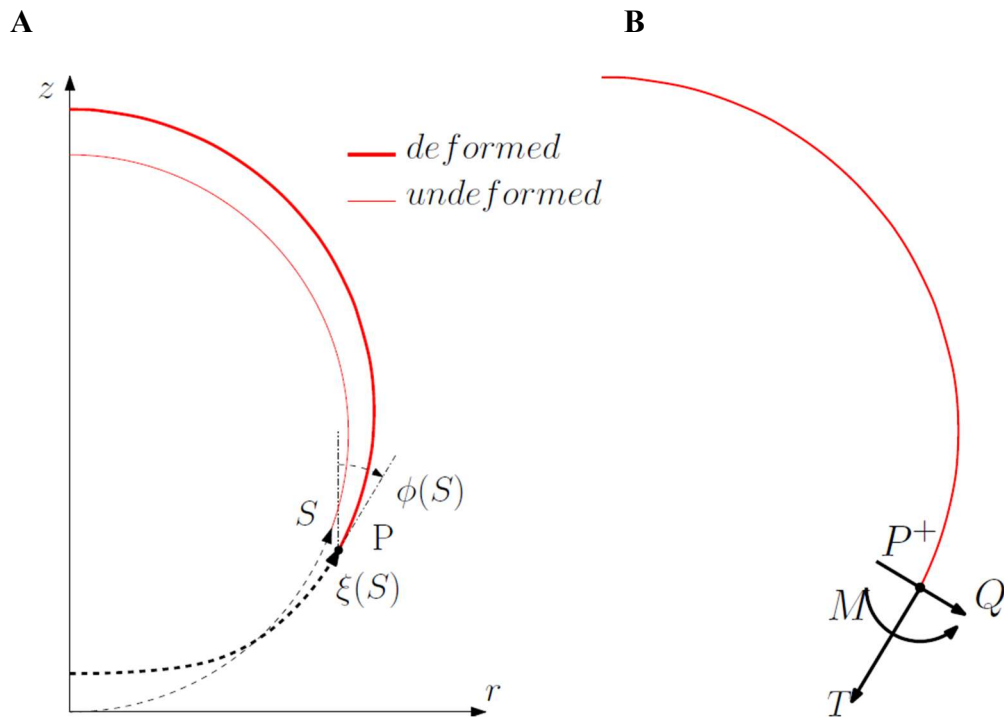


Figure A 2.6 (A) Arc length and tangent angle over the membrane, (B) Forces and moment along the cut in the membrane.

As shown above non-dimensionalization of all the length scales is done by the radius of the undeformed vesicle, R . As c has units of energy, we use it to non-dimensionalize force per unit length quantities i.e. in-plane tension, T and out of plane shear, Q by c / R^2 . Also force per unit area quantities, p_0, F_e, F_t and F_n are made dimensionless by c / R^3 .

Also, in both the loading conditions it has been assumed that the F_t for vesicle is always zero. There are six ordinary differential equations governing the deformation of the vesicle membrane, they are:

$$\begin{aligned}
\dot{\bar{Q}} &= -\frac{\bar{Q}}{\bar{r}} \dot{\bar{\xi}} \sin \phi - 2\bar{H} \dot{\bar{\xi}} \left[\bar{d} + \bar{H}^2 + \left(2\bar{H} + \frac{\cos \phi}{\bar{r}} \right) \frac{\cos \phi}{\bar{r}} \right] + \dot{\bar{\xi}} \bar{p}, \\
\dot{\phi} &= \dot{\bar{\xi}} \left(2\bar{H} + \frac{\cos \phi}{\bar{r}} \right), \\
\dot{\bar{H}} &= \dot{\bar{\xi}} \bar{Q}, \\
\dot{\bar{r}} &= \dot{\bar{\xi}} \sin \phi, \\
\dot{\bar{z}} &= \dot{\bar{\xi}} \cos \phi, \\
\dot{\bar{d}} &= \left(\bar{F}_e \cos \phi + \bar{F}_t \right) \dot{\bar{\xi}}
\end{aligned} \tag{A2.11a-A2.11f}$$

where, the dot denotes differentiation with respect to the normalized undeformed arc length

\bar{S} , and

$$\dot{\bar{\xi}} \equiv \frac{\sin \bar{S}}{\bar{r}}. \tag{A2.11g}$$

The normalized normal force acting on the deformed membrane surface, \bar{p} in equation A2.11a is related to the osmotic pressure of the vesicle, \bar{p}_0 , the electrostatic force per unit area, \bar{F}_e and the normal component of the concentrated load applied at $\bar{S} = \bar{S}_0, \bar{F}_n$ by,

$$\bar{p} = \bar{p}_0 + \bar{F}_e \sin \phi + \bar{F}_n \delta(\bar{S} - \bar{S}_0) \quad (\text{A2.11h})$$

where, $\delta(\bar{S} - \bar{S}_0)$ is the Dirac delta function.

These differential equations are supplemented with the boundary conditions:

$$\begin{aligned} \phi(\bar{S} = 0) &= \frac{\pi}{2}, \\ \bar{Q}(\bar{S} = 0) &= 0, \\ \bar{r}(\bar{S} = 0) &= 0, \\ \phi(\bar{S} = \pi) &= -\frac{\pi}{2}, \\ \bar{Q}(\bar{S} = \pi) &= 0, \\ \bar{r}(\bar{S} = \pi) &= 0, \end{aligned} \quad (\text{A2.12a-A2.12f})$$

The boundary conditions defined above essentially represent the symmetry in the vesicle geometry. About the symmetry axis, the curve has zero slope and out of plane shear \bar{Q} is zero, at both $\bar{S} = 0$ and π . Also, for the continuity of the geometry, we impose $\bar{r} = 0$ at both $\bar{S} = 0$ and π .

The notation for positive shear force and tension is described in Fig. A2.6. Finally, the expression for the in-plane tension in both the vesicle and plasma membrane is given by,

$$\bar{T} = \frac{TR^2}{c} = \frac{R^2}{c} \left(-d - cH^2 - cH \frac{\cos \phi}{r} \right). \quad (\text{A2.13})$$

The governing equations for the deformation of the plasma membrane is very similar, except that equation (A2.11g) must be replaced by,

$$\dot{\xi} = \frac{\dot{\bar{S}}}{\bar{r}} \quad (\text{A2.14})$$

This change is due to the difference between the reference configurations. The boundary conditions are:

$$\begin{aligned}
\phi(\bar{S}=0) &= \frac{\pi}{2}, \\
\bar{Q}(\bar{S}=0) &= 0, \\
\bar{r}(\bar{S}=0) &= 0, \\
\phi\left(\bar{S}=\frac{L}{R}\right) &= \frac{\pi}{2}, \\
\bar{z}\left(\bar{S}=\frac{L}{R}\right) &= 0, \\
\bar{T}\left(\bar{S}=\frac{L}{R}\right) &= \left[-\bar{d} - \bar{H}^2 - \bar{H} \frac{\cos\phi}{\bar{r}}\right]_{\bar{S}=\frac{L}{R}} = \bar{T}_0 \equiv \frac{T_0 R^2}{c}
\end{aligned} \tag{A2.15a-A2.15f}$$

The boundary conditions at $\bar{S} = 0$ is due to axisymmetry. Equation (A2.15f) states that the tension in the plasma membrane approaches the pretension at the boundary. This boundary condition allows the neuron membrane to deflect. Had we replaced this boundary condition with a clamped condition, the deflection everywhere would be zero because of area incompressibility.

The coupled ODE's in equations (A2.11 – A2.15) with the boundary conditions are solved using the MATLAB® bvp4c solver. The input parameters for the solver are the osmotic pressure p_0 across the vesicle membrane which remains fixed throughout the deformation, SNARE-machinery force parameters (S_0 and magnitude F), electrostatic force and pretension (T_0) in the plasma membrane.

2.5.7 Example Problem of Continuum Model

Here we show an example of the results of the calculation of vesicle-membrane interaction.

In this example, the location of force application is fixed at $\bar{S}_0 = \frac{\pi}{6}$ on both the vesicle and neuron base, as shown in Fig. A2.7. This location of load application corresponds to the number of SNAREs of 21. Parameters used in the continuum model are shown in Table A2.3.

Table A 2.3 Parameters used for the continuum model of the vesicle and plasma membrane

Parameter	Value	Comment
Permittivity of vacuum, ϵ_0	$8.85 \times 10^{-12} \text{ Fm}^{-1}$	
Dielectric constant of water, ϵ	80	Dimensionless
Ion concentration inside neuron, c_0	200 mM ⁶⁴	(1-1) Electrolyte
Debye length, l_D	0.67nm	$l_D = \sqrt{\frac{\epsilon\epsilon_0 k_B T}{2q^2 z^2 c_0}}$
Synaptic vesicle radius, R	20nm ⁶⁵	
Surface charge of vesicle and inside of plasma membrane, σ_1 and σ_2	-0.025 Cm ⁻² , -0.025 Cm ⁻² <small>38,40,65</small>	
Surface potential of vesicle and inside of plasma membrane, φ_1 and φ_2	-25 mV, -25 mV	
Bending rigidity of lipid bilayer, c	$\sim 20 \text{ k}_B\text{T}$ ⁶⁶	$8.28 \times 10^{-20} \text{ J}$

The strength of the line force is varied in the range of 5 – 20 in dimensionless terms, which is equivalent to a net force between 66 – 266 pN. Fig. A2.7 shows the deformed shapes of the membranes for four different values of \bar{F} . The inset on the right shows the calculated relationship between applied force and separation between load application points. The force decreases rapidly with increasing separation, reflecting the steep decay of the electrostatic repulsion.

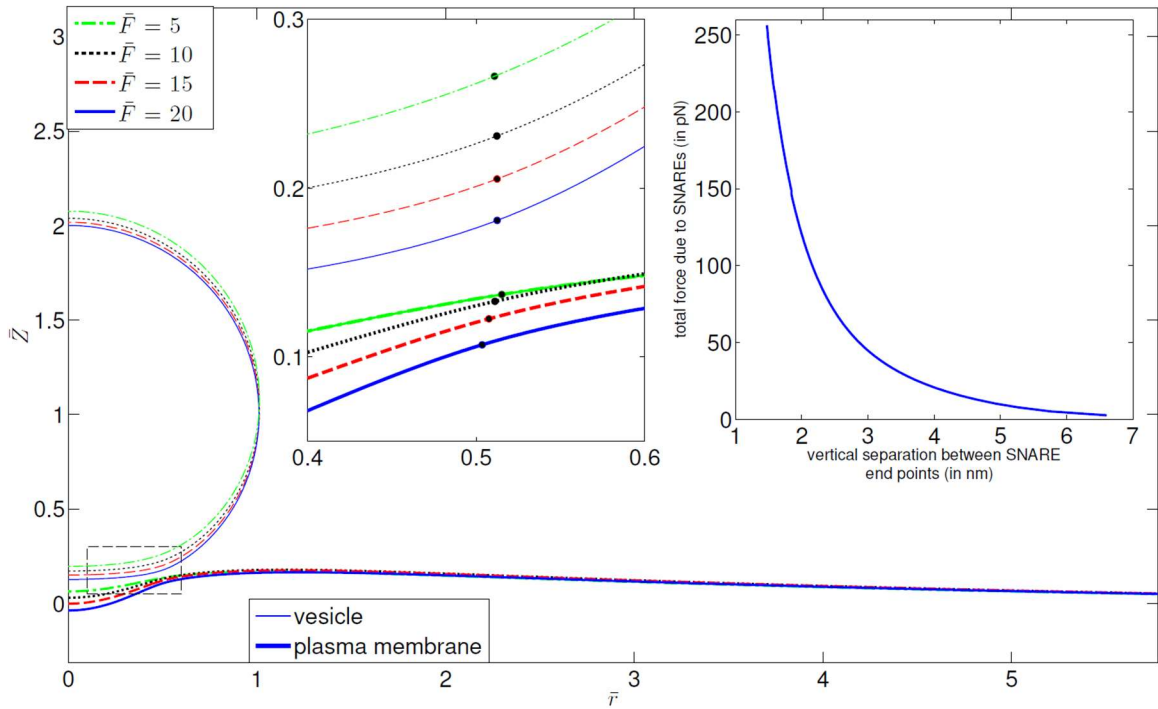


Figure A 2.7 Deformed geometry for different force magnitudes. The thick lines represent the neuron base and the thin lines represent the vesicle. The inset on the left shows the zoomed in section of the load application point (*shown as •*) and the inset on the right shows the vertical separation between the two ends of SNARE-machinery versus the net SNARE force. The parameters are for the analysis are: load application point, $\bar{s}_0 = \pi / 6$, pretension in plasma membrane, $\bar{T}_0 = 1$ and vesicle pressure. $\bar{p}_0 = 1$.

2.5.8 SNARE Force Separation Curve Shift

To compare the attractive force imposed by the SNARE bundle to the repulsive force on the vesicle, we need a consistent definition of separation. The distance connecting the final residue beads (Syb89 and Syx256) is shorter than the distance between the outside membrane surfaces due to the presence of other parts of the SNARE. To address this issue, we created a static coarse grained structure of a 20 nm vesicle and plasma

membrane with a partially opened SNARE at its equilibrium configuration as shown in the figure below. We found that distance between the outer surface of the membranes is actually about $\sim 1\text{nm}$ further apart than the distance between Syb89 and Syx256. We have therefore added this distance when comparing the attractive force on the SNARE to the repulsive force on the vesicle. Adding the initial separation between Syb89 and Syx256, the minimum distance allowed between the membranes at the point of force application is about 2nm . Another related effect is that inter-SNARE-bundle repulsion can increase the minimum lateral separation. We have considered two additional cases where we take lateral SNARE bundle width to be 2 and 4 nm (an additional Debye screening length increase in radius in the latter case). The larger lateral spacing makes the effect of number of SNAREs significantly stronger but the minimum separation and the number of SNAREs needed to achieve it does not change much.

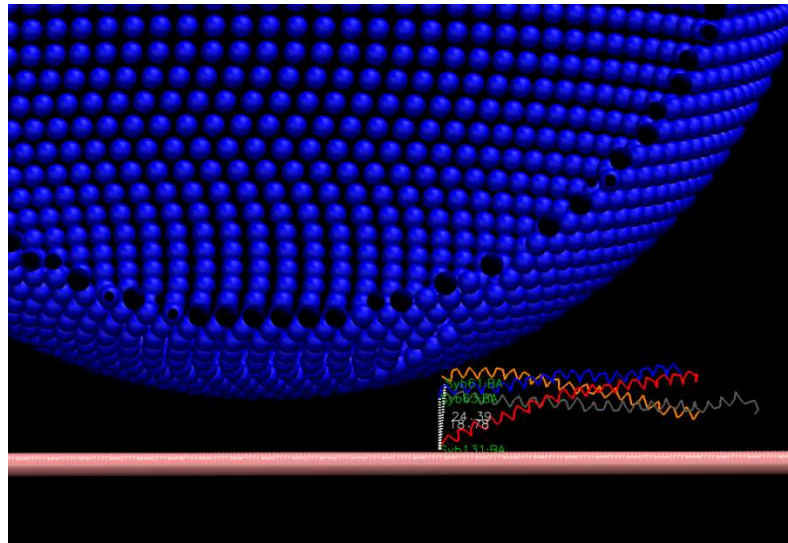


Figure A 2.8 Drawing of a vesicle near a plane along with a model for the SNARE bundle.

2.5.9 Choice of SNARE Model

The CG simulation model was built using the SNARE X-ray crystal structure 1N7S that includes Syb (27-89), Syx (189-256), SN1 (5-83), and SN2 (139-204). We recognize that this structure only includes part of the Syb linker domain (85-95) and none of the linker domain of Syx (256-266). However, we believe that our choice of placing the membrane outer surface at residues 89 and 256 is correct. Our choice is based on the following papers^{67,68} that show Syb insertion in the membrane starts at Trp 89. Specifically, they show that 89-94 is unstructured but is inserted in the membrane. Similarly, the following paper shows that for Syx, residues after 261 are in the lipid bilayer. Specifically, 261-266 are unstructured but inside the lipid bilayer⁶⁹. The following study⁷⁰ also concludes that the linker domains (256-266) and (85-95) are buried in the top layer of the membrane. Because the reference distance from the hydration repulsion is the outer surface of the membrane, to be consistent we believe that it is quite appropriate to define SNARE displacement from 88 for Syb to 256 for Syx, within some uncertainty of a just a few residues.

Whether or not the linker domains have unraveled is debatable. It was shown in Gao et al's optical tweezer experiment that the Syb linker domain unravels at 10-13 pN. Because the equilibrium SNARE end-end distances of interest in this work are (~ 3 nm), our maximum force only reaches (<5 pN) and neglecting helix unraveling in our model is justifiable. Nevertheless, in order to check the robustness of our solution against

unraveling, we did melt two helical turns of Syb (including up to residue 91). The principal effect is that the minimum equilibrium separation increases from 2 nm to 2.5 nm for both hydration and electrostatic repulsion with a constant charge.

2.5.10 Robustness of Model Results

To judge the sensitivity of our main conclusions on the various assumptions we have made, we carried out a number of other simulations. Our main conclusion is that the principal results of our model are quite robust with respect to uncertainty in the assumptions made.

Electrostatics: We explored how electrostatics would affect the vesicle to plasma membrane repulsion. Fig. A2.9 shows results for the case where hydration repulsion is replaced by electrostatics using a fixed surface charge of -0.025 C/m^2 on the vesicle and the membrane. Evidently, with these parameters the electrostatic repulsion is weaker than the hydration repulsion. For one SNARE the end separation is $\sim 2.4 \text{ nm}$, which is smaller than the 3 nm seen for the hydration repulsion case (Fig. 2.4B). However, when more than 1 SNARE is added to the system, the equilibrium SNARE end separation is constant at $\sim 2 \text{ nm}$ for 2-13 SNAREs, that is, it would be completely zippered shut.

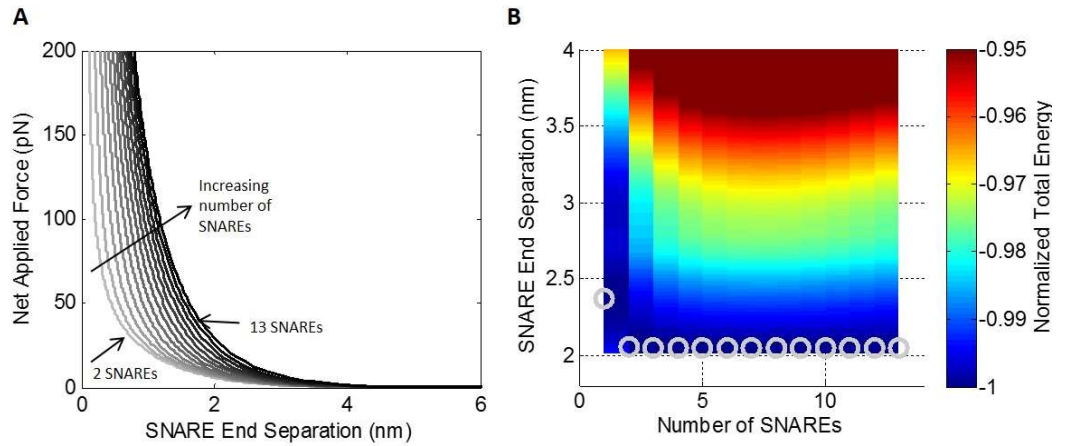


Figure A 2.9 (A) The force in the membrane/vesicle system is shown as a function of SNARE end separation for a vesicle radius of 20nm with electrostatic repulsion with a fixed surface charge. (B) The corresponding contour plot of total energy as a function of SNARE end separation distance and the number of SNAREs. Gray circles correspond to global energy minima representing the equilibrium SNARE end separation for a given number of SNAREs.

Larger vesicles: Although our primary interest is in the smaller synaptic vesicles, the model can also be applied to study larger vesicles. Fig. A2.10 shows results for the case of a 100 nm vesicle.

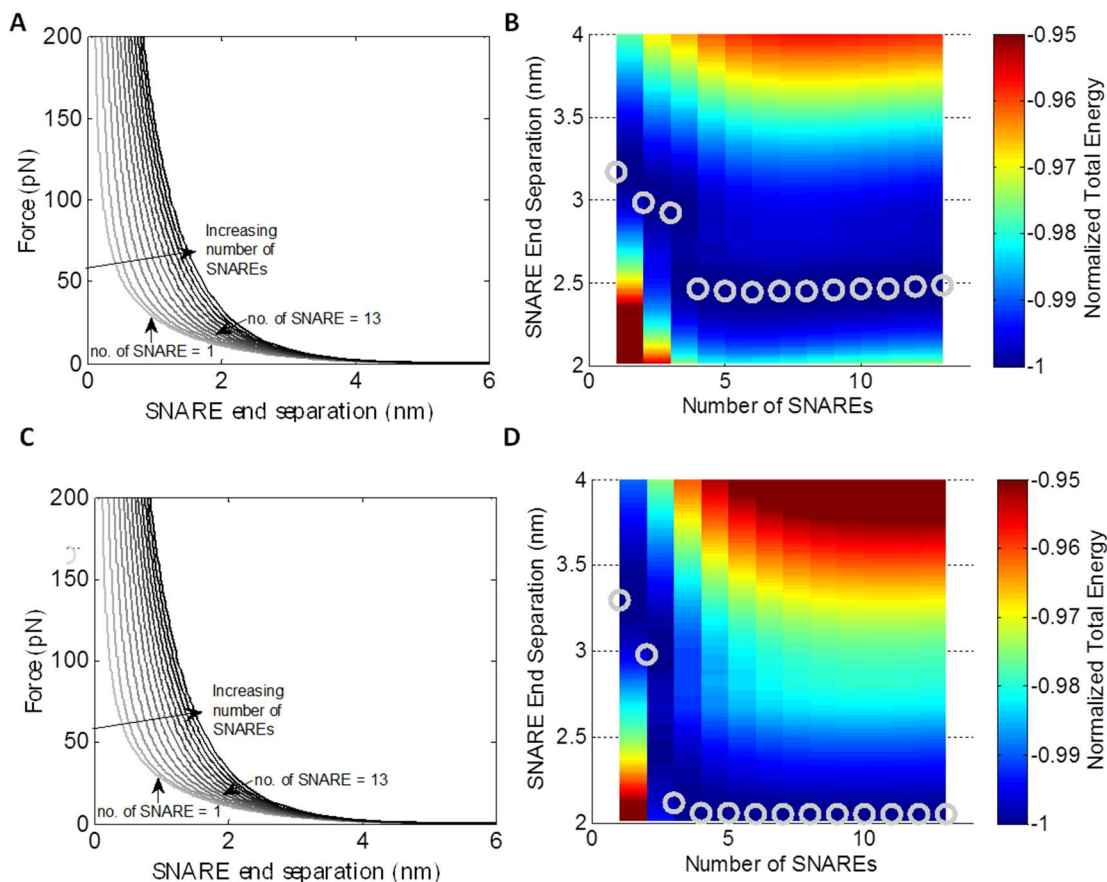


Figure A 2.10 The force in the membrane/vesicle system is shown as a function of SNARE end separation for a vesicle radius of 100nm with (A) hydration repulsion and (C) electrostatic repulsion with a fixed surface charge. Contour plots of total energy as a function of SNARE end separation distance and the number of SNAREs are shown for a vesicle radius of 100nm with (B) hydration repulsion and (D) electrostatic repulsion with a fixed surface charge. Gray circles correspond to global energy minima representing the equilibrium SNARE end separation for a given number of SNAREs.

For the hydration repulsion case the minima are significantly larger than those found for the 20nm case shown in Fig. 2.4B. For four or more SNAREs the equilibrium separation is ~ 2.5 nm which is different from the 20nm case where the separation is ~ 2 nm and the SNARE bundle can be nearly fully zippered. For the case of electrostatic repulsion, for

larger number of SNAREs the repulsion is still insufficient to open the SNARE except when there is are three or fewer SNAREs.

Fixed Potential: We also carried out computations assuming a fixed potential of -25 mV on the vesicle and on the membrane as opposed to the fixed surface charge case that was assumed in the majority of the paper. The resulting force separation curves for the 20nm and 100nm vesicle cases are very similar to the case of fixed charge. This is not unexpected because the electrostatic force for fixed charge versus fixed potential cases becomes nearly the same for separations greater than the Debye screening length.

Unraveling of Syb: Several other modifications were made to the cases shown in Fig. 2.4. There is some question about whether part of the syb helix unravels. We have argued that the forces are small enough that the helical structure should be preserved. However, to test the effect on our prediction of potential unraveling, we allowed 2 helical turns to unravel and be represented by elasticity of a worm-like chain coil. Because the Syb helix touches the membrane at residue 91 and the CG model only contains up to residue 89, an extra 2 residues were added to the unraveled portion of Syb. The force displacement curve for the melted portions of Syb were modeled using a worm like chain model following Gao et al.⁸ The force extension relationship was calculated using the Marko-Siggia formula^{71,72}

$$F = \frac{k_B T}{P_{melt}} \left[\frac{1}{4 \left(1 - \frac{x_{melt}}{L_{melt}} \right)^2} + \frac{x_{melt}}{L_{melt}} - \frac{1}{4} \right] \quad (A2.16)$$

where P_{melt} is the persistence length of the melted segment (0.6 nm) and x_{melt} is the end to end distance of the melted segment. L_{melt} , the maximum end to end distance of the melted segment, was calculated assuming a 0.365 nm contour length per residue⁸ which totaled to 1.3 nm due to ~2 helical turns being melted. The master force displacement curve was slightly adjusted by deleting the portions of the curve that corresponded to the 7 residues that are now accounted for using the WLC model. The SNARE end separation, x_{SNARE} , was defined by

$$x_{SNARE}(F) = x_{melt}(F) + x_{bundle}(F) + BW \quad (A2.17)$$

where x_{melt} is the end to end distance of the melted portion of Syb, x_{bundle} is described using the manipulated master force curve described in this section, and BW is the width of the SNARE bundle or the distance between the Syb and Syx C-termini when no external force is being applied. The corresponding results are shown in Fig. A2.11A for a 20nm vesicle with hydration repulsion and Fig. A2.12A for a 20nm vesicle with electrostatic repulsion and a fixed surface charge.

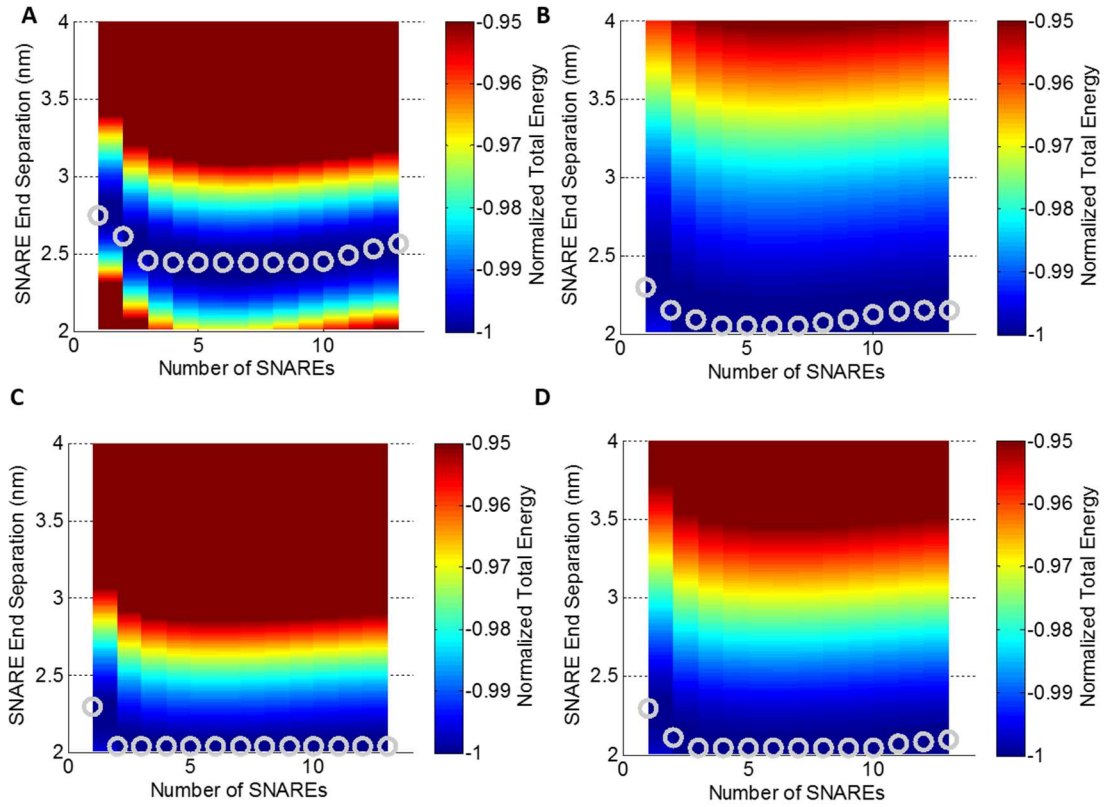


Figure A 2.11 For a 20nm vesicle with hydration repulsion, contour plots of normalized total energy as a function of SNARE end separation distance and the number of SNAREs are shown. Gray circles correspond to energy minima representing the equilibrium SNARE end separation for a given number of SNAREs. Several cases are shown: (A) 2 helical turns unraveled, (B) Syx frozen, (C) SNAP25 frozen, and (D) Syx and SNAP25 frozen.

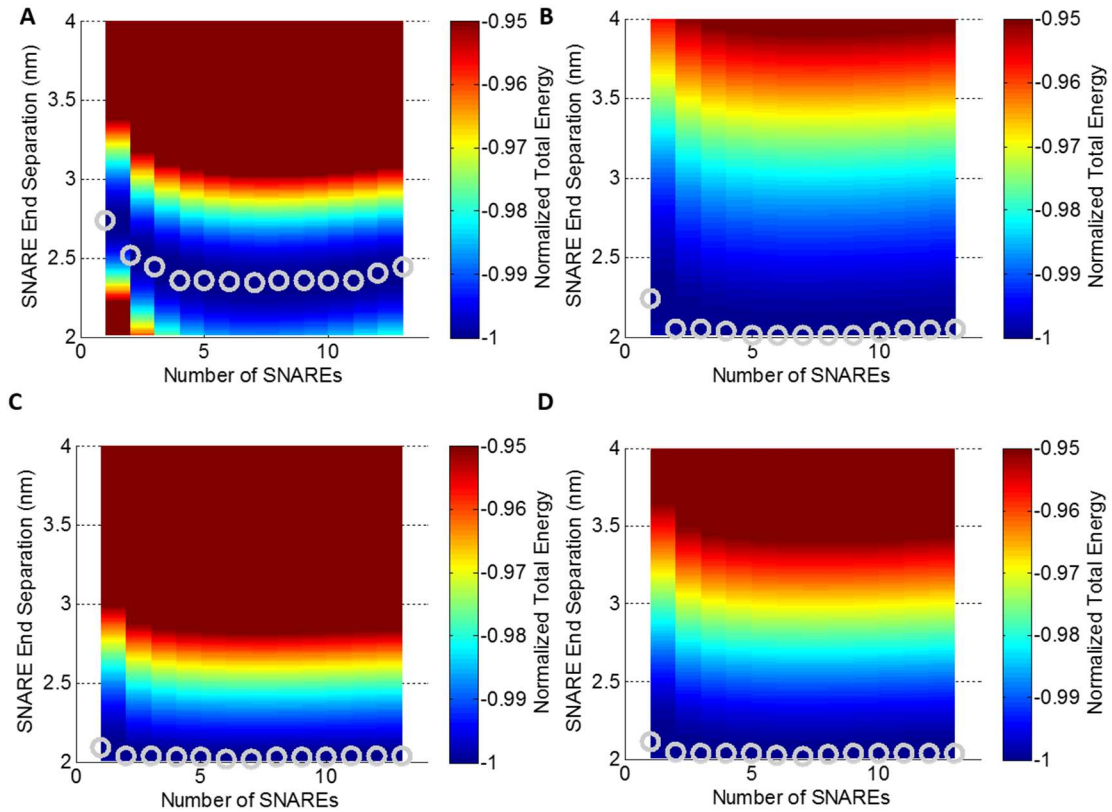


Figure A 2.12 For a 20nm vesicle with electrostatic repulsion assuming a fixed surface charge, contour plots of normalized total energy as a function of SNARE end separation distance and the number of SNAREs are shown. Gray circles correspond to energy minima representing the equilibrium SNARE end separation for a given number of SNAREs. Several cases are shown: (A) 2 helical turns unraveled, (B) Syx frozen, (C) SNAP25 frozen, and (D) Syx and SNAP25 frozen.

In both cases, the results differ from those seen in Fig. 2.4 when unraveling was not permitted. For the case of hydration repulsion, the minimum separation is somewhat larger (~2.4 nm) than that shown in Fig. 4 B (~2.1 nm). There is a similar difference for the case of electrostatic repulsion.

Freezing SNAP25 or Syx: In our simulations we allowed SNAP25 helices to be free to adjust their orientation. This mimics the optical tweezers experiment used to calibrate our model. However, the situation *in vivo* is likely different with SNAP25 and/or Syx constrained against motion. In order to see the effects of the positioning of SNAP25 in relation to the SNARE bundle we studied three variations: freezing Syx, freezing SNAP25, and freezing both Syx and SNAP25. When Syx was frozen, SNAP25 still remained associated with Syb. Anytime that SNAP25 was frozen at all, it remained associated with Syx. The energy calculations were repeated for the hydration repulsion case (Fig. A2.11) and the electrostatic repulsion case with fixed surface charge (Fig. A2.12). The freezing of helices in all of these cases has little effect on the minimum distance and number of SNAREs. The principal difference occurs for the one-SNARE case where the equilibrium distance reduces significantly.

High Osmotic Pressure and Low Pretension Limit

Figs. 2.2 and A2.7 show cases of low osmotic pressure and plasma membrane tension where the plasma membrane bulges near the axis of symmetry because the attractive forces draw the two membranes to each other at their point of application but near the axis of symmetry only repulsion acts. Experiments suggest that prior to vesicle to membrane fusion, the vesicle retains its spherical shape while the plasma membrane surface conforms when the two are in contact^{45,46}. The continuum model was recalculated using high osmotic pressure in the vesicle and low pretension in the plasma membrane with constant potential. The resulting structures are shown for 10 and 15 SNAREs in Fig. A2.16.

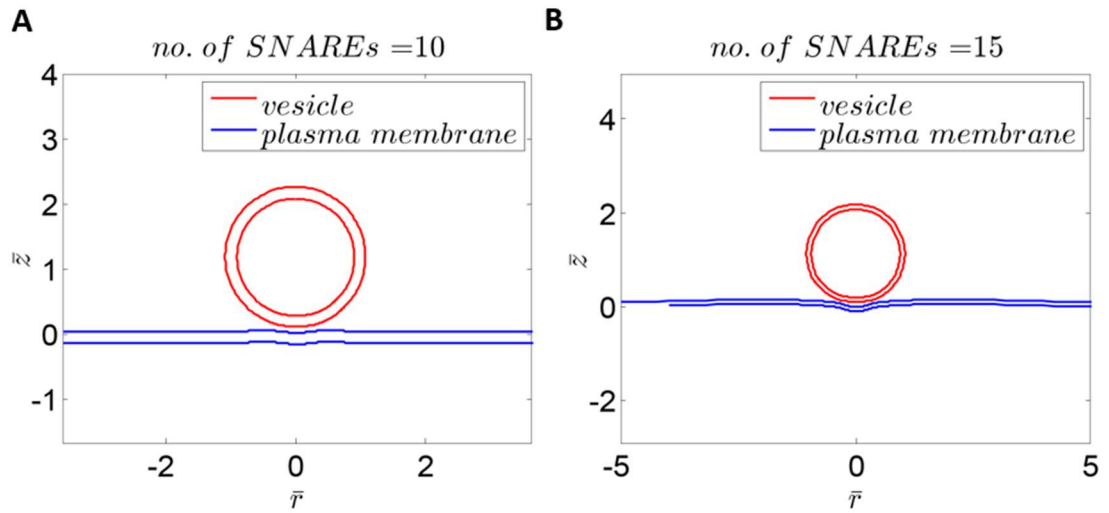


Figure A 2.13 For a 20nm vesicle with high osmotic pressure and low pretension in the plasma membrane with constant potential the vesicle and plasma membrane structures are shown including their bilayer thickness for (A) 10 SNAREs and (B) 15 SNAREs.

Under the conditions of high osmotic pressure and low pretension when 10 SNAREs are present there is little bulging of the plasma membrane and the vesicle remains spherical when the vesicle and plasma membrane are brought together. The separation is relatively constant which is consistent with the Malsam et al.⁴⁵ and Hernandez et al.⁴⁶. As the number of SNAREs is increased to 15, there is some bulging in the plasma membrane at the axis of symmetry. The vesicle has retained its spherical shape while the plasma membrane bends to conform to it.

The energy surface for this case is shown in Fig. A2.14. We note that there is little difference between these and those of Fig. 2.4B. This suggests that our model is robust with respect to this uncertainty. (In particular, the value of vesicle osmotic pressure is difficult to estimate.)

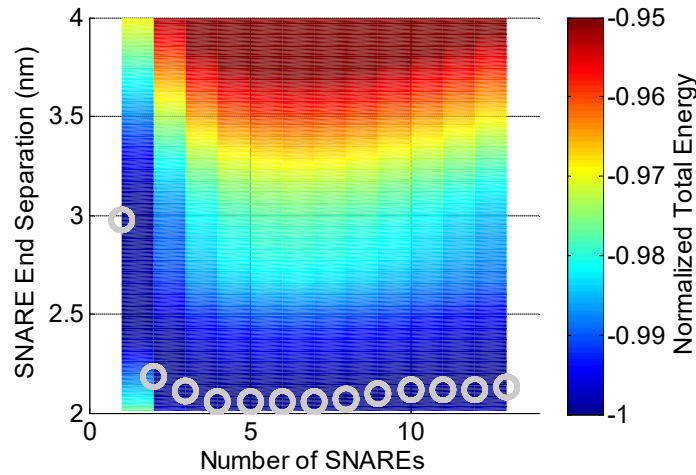


Figure A 2.14 Contour of normalized total energy as a function of SNARE end separation and number of SNAREs for a 20nm vesicle with high osmotic pressure and low pretension in the plasma membrane, and with constant potential on the vesicle and plasma membrane. White circles correspond to energy minima representing the equilibrium SNARE end separation for a given number of SNAREs.

High Vesicle Pressure, High Membrane Tension Vesicle-Membrane Model

In order to display the effects of the deformation considered in the continuum model, a more simplified analytical model of the Vesicle-Membrane system based on Bykhovskaia et al.¹¹ was calculated. The parameters used in the analytical model were consistent with those used in the continuum model as described in Section 2.2.3. Consider the case in which vesicle pressure P_0 and the membrane tension T are sufficiently large such that neither the vesicle nor the membrane deform as they approach each other. In this case Bykhovskaia et al.¹¹ have shown that the force between the vesicle and membrane is given by

$$F = \frac{2\pi R \varepsilon \varepsilon_0}{l_D} \left(\frac{2\varphi_1 \varphi_2}{\sinh\left(\frac{a}{l_D}\right)} - (\varphi_1^2 + \varphi_2^2) \left(\coth\left(\frac{a}{l_D}\right) - 1 \right) \right) \quad (\text{A2.18})$$

for fixed surface potential and

$$F = \frac{\pi R l_D}{\varepsilon \varepsilon_0} \left(\frac{2\sigma_1 \sigma_2}{\sinh\left(\frac{a}{l_D}\right)} + (\sigma_1^2 + \sigma_2^2) \left(\coth\left(\frac{a}{l_D}\right) - 1 \right) \right) \quad (\text{A2.19})$$

for fixed charge. The force separation curves are shown for the vesicle-plasma membrane for several cases using this model in Figs. A2.15 and A2.16.

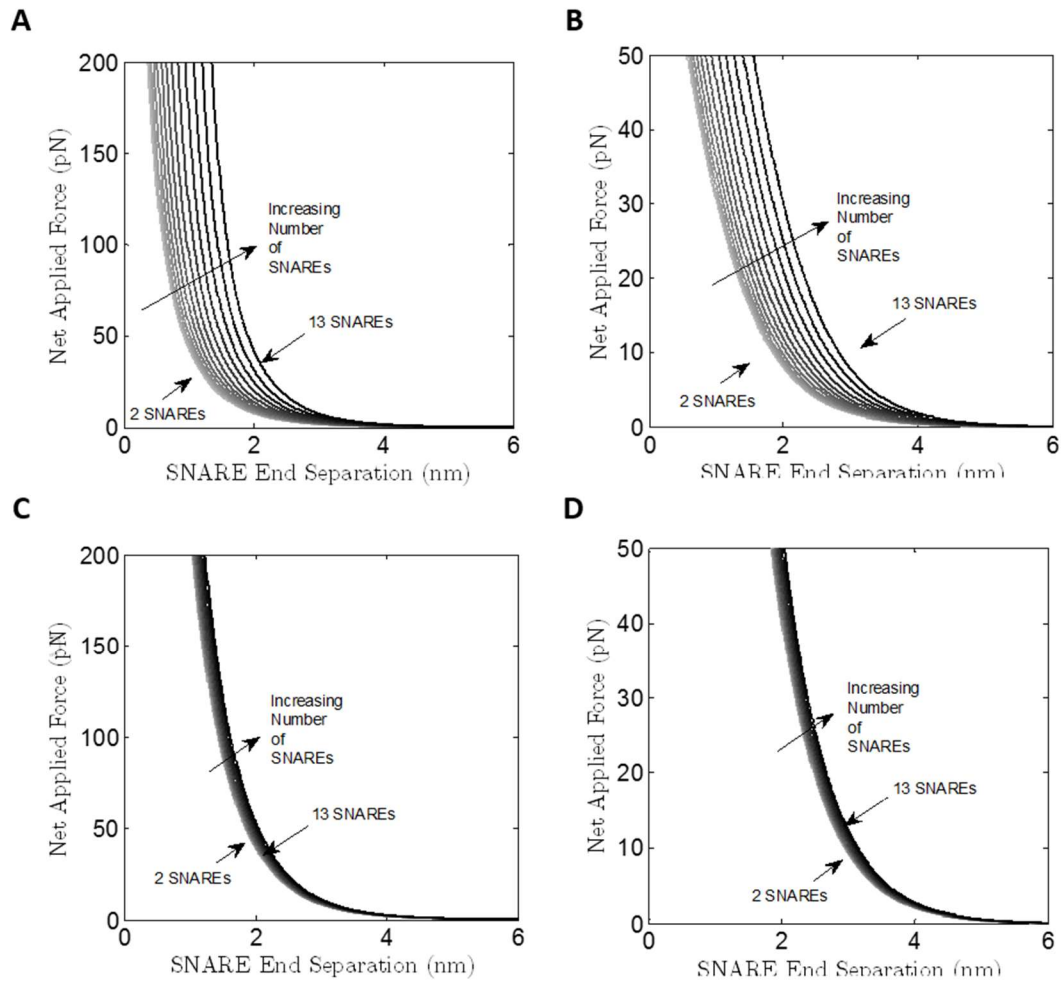


Figure A 2.15 For the high vesicle pressure high membrane tension limiting case, the net applied force in the membrane/vesicle system is shown as a function of SNARE end separation for a vesicle with a (A) 20nm radius with fixed charge, (B) 20nm radius with fixed surface potential, (C) 100nm radius with fixed charge, and (D) 100nm radius with fixed surface potential.

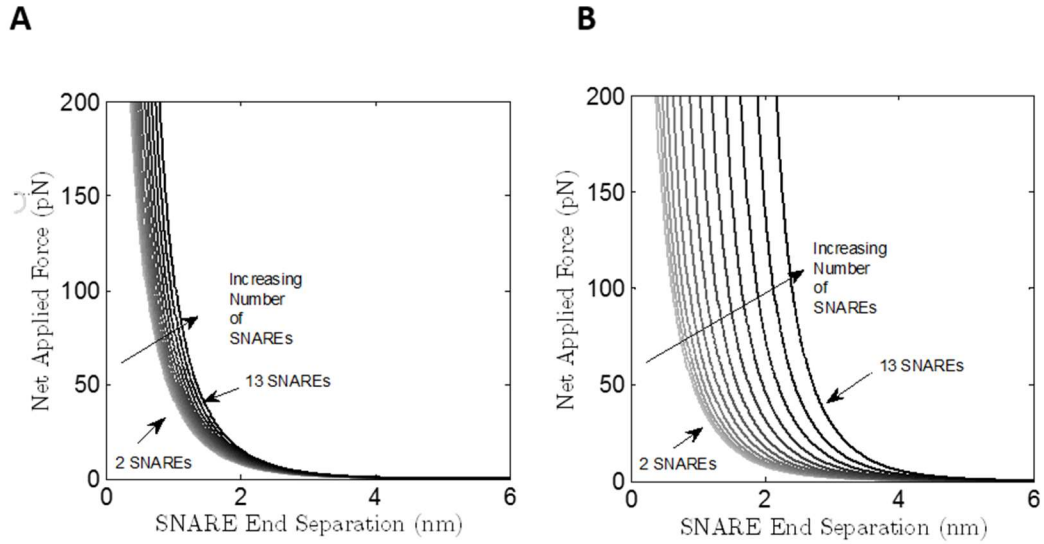


Figure A 2.16 For the high vesicle pressure high membrane tension limiting case, the net applied force in the membrane/vesicle system is shown as a function of SNARE end separation for a radius for a vesicle with a 20nm radius with fixed charge when (A) the SNARE bundle diameter is 2nm and (B) the SNARE bundle diameter is 2nm.

Effect of Lateral Bundle Width: Figure A2.17 shows results of a test of the sensitivity of the solution to the location of the SNAREs when the lateral size of the SNARE bundle was varied from 2nm in Fig. A2.17A to 4nm in Fig. A2.17B (the base case used is 3nm, Fig. 2.4B). Increasing the lateral width of the SNARE bundle seems to have a significant effect on the solution. There is a minimum separation at 4 SNAREs. With the addition of more than 5 SNAREs the equilibrium separation again begins to increase all the way up to ~3nm with 13 SNAREs.

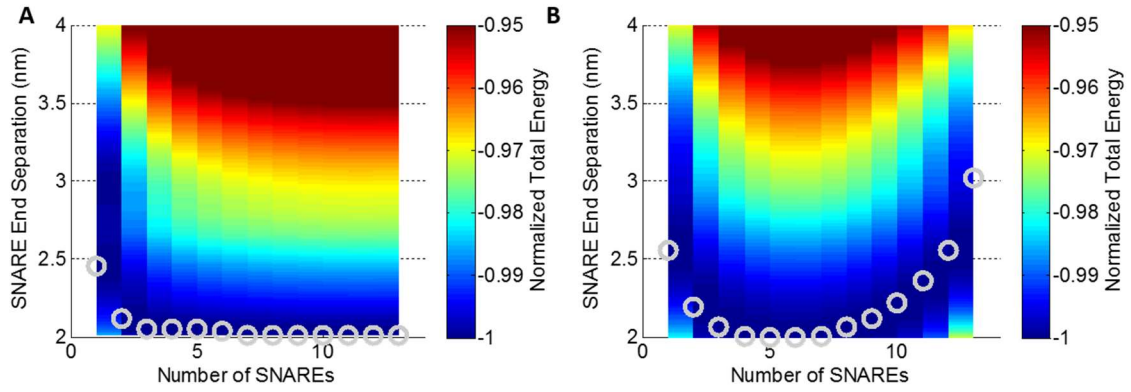


Figure A 2.17 For the high pressure high tension limiting case, contour plots of normalized total energy as a function of SNARE end separation distance and the number of SNAREs are shown. Gray circles correspond to energy minima representing the equilibrium SNARE end separation for a given number of SNAREs. Several cases are shown for the vesicle with a radius of 20nm and fixed charge. The size of the SNARE bundle was varied to (A) 2nm and (B) 4nm.

2.6 References

1. Südhof, T. C. The synaptic vesicle cycle: a cascade of protein-protein interactions. *Nature* **375**, 645–653 (1995).
2. Hanson, P. I., Heuser, J. E. & Jahn, R. Neurotransmitter release - four years of SNARE complexes. *Current Opinion in Neurobiology* **7**, 310–315 (1997).
3. Söllner, T., Bennett, M. K., Whiteheart, S. W., Scheller, R. H. & Rothman, J. E. A protein assembly-disassembly pathway in vitro that may correspond to sequential steps of synaptic vesicle docking, activation, and fusion. *Cell* **75**, 409–418 (1993).
4. Rothman, J. E. Mechanisms of intracellular protein transport. *Nature* **372**, 55–63 (1994).
5. Gracheva, E. O., Maryon, E. B., Berthelot-Grosjean, M. & Richmond, J. E. Differential regulation of synaptic vesicle tethering and docking by UNC-18 and TOM-1. *Front. Synaptic Neurosci.* (2010). doi:10.3389/fnsyn.2010.00141
6. Sutton, R. B., Fasshauer, D., Jahn, R. & Brunger, A. T. Crystal structure of a SNARE complex involved in synaptic exocytosis at 2.4 Å resolution. *Nature* **395**, 347–353 (1998).
7. Ernst, J. A. & Brunger, A. T. High resolution structure, stability, and synaptotagmin binding of a truncated neuronal SNARE complex. *J. Biol. Chem.* **278**, 8630–8636 (2003).
8. Gao, Y. *et al.* Single reconstituted neuronal SNARE complexes zipper in three distinct stages. *Science* **337**, 1340–3 (2012).
9. Durrieu, M.-P., Lavery, R. & Baaden, M. Interactions between neuronal fusion

- proteins explored by molecular dynamics. *Biophys. J.* **94**, 3436–3446 (2008).
10. Bock, L. V., Hutchings, B., Grubmüller, H. & Woodbury, D. J. Chemomechanical regulation of SNARE proteins studied with molecular dynamics simulations. *Biophys. J.* **99**, 1221–1230 (2010).
 11. Bykhovskaia, M., Jagota, A., Gonzalez, A., Vasin, A. & Littleton, J. T. Interaction of the complexin accessory helix with the C-terminus of the SNARE complex: molecular-dynamics model of the fusion clamp. *Biophys J* **105**, 679–690 (2013).
 12. Durrieu, M. P., Bond, P. J., Sansom, M. S. P., Lavery, R. & Baaden, M. Coarse-grain simulations of the R-SNARE fusion protein in its membrane environment detect long-lived conformational sub-states. *ChemPhysChem* **10**, 1548–1552 (2009).
 13. Lindau, M., Hall, B. A., Chetwynd, A., Beckstein, O. & Sansom, M. S. P. Coarse-grain simulations reveal movement of the synaptobrevin C-terminus in response to piconewton forces. *Biophys. J.* **103**, 959–69 (2012).
 14. Marrink, S. J., Risselada, H. J., Yefimov, S., Tieleman, D. P. & De Vries, A. H. The MARTINI force field: Coarse grained model for biomolecular simulations. *J. Phys. Chem. B* **111**, 7812–7824 (2007).
 15. Lamberg, A. & Taniguchi, T. Coarse-grained computational studies of supported bilayers: current problems and their root causes. *J. Phys. Chem. B* **118**, 10643–52 (2014).
 16. Han, X., Wang, C.-T., Bai, J., Chapman, E. R. & Jackson, M. B. Transmembrane segments of syntaxin line the fusion pore of Ca²⁺-triggered exocytosis. *Science* **304**, 289–292 (2004).

17. van den Bogaart, G. & Jahn, R. Counting the SNAREs needed for membrane fusion. *J Mol Cell Biol* **3**, 204–205 (2011).
18. Sinha, R., Ahmed, S., Jahn, R. & Klingauf, J. Two synaptobrevin molecules are sufficient for vesicle fusion in central nervous system synapses. *Proc Natl Acad Sci U S A* **108**, 14318–14323 (2011).
19. Mohrmann, R., de Wit, H., Verhage, M., Neher, E. & Sorensen, J. B. Fast vesicle fusion in living cells requires at least three SNARE complexes. *Science* (80-.). **330**, 502–505 (2010).
20. Karatekin, E. *et al.* A fast, single-vesicle fusion assay mimics physiological SNARE requirements. *Proc Natl Acad Sci U S A* **107**, 3517–3521 (2010).
21. Zhang, Z., Pfaendtner, J., Grafmuller, A. & Voth, G. A. Defining coarse-grained representations of large biomolecules and biomolecular complexes from elastic network models. *Biophys J* **97**, 2327–2337 (2009).
22. Chu, J. W. & Voth, G. A. Coarse-grained modeling of the actin filament derived from atomistic-scale simulations. *Biophys J* **90**, 1572–1582 (2006).
23. Miyazawa, S. & Jernigan, R. L. Estimation of effective interresidue contact energies from protein crystal structures: quasi-chemical approximation. *Macromolecules* **18**, 534–552 (1985).
24. Miyazawa, S. & Jernigan, R. L. Residue-residue potentials with a favorable contact pair term and an unfavorable high packing density term, for simulation and threading. *J. Mol. Biol.* **256**, 623–644 (1996).
25. Miyazawa, S. & Jernigan, R. L. Self-consistent estimation of inter-residue protein contact energies based on an equilibrium mixture approximation of residues.

- Proteins Struct. Funct. Genet.* **34**, 49–68 (1999).
26. Jenkins, J. T. Static equilibrium configurations of a model red blood cell. *J Math Biol* **4**, 149–169 (1977).
 27. Long, R., Hui, C. Y., Jagota, A. & Bykhovskaia, M. Adhesion energy can regulate vesicle fusion and stabilize partially fused states. *J. R. Soc. Interface* **9**, 1555–1567 (2012).
 28. Hess, B., Kutzner, C., Van Der Spoel, D. & Lindahl, E. GROMACS 4: Algorithms for highly efficient, load-balanced, and scalable molecular simulation. *J. Chem. Theory Comput.* **4**, 435–447 (2008).
 29. Foloppe, N. & Mackerell, A. D. All-Atom Empirical Force Field for Nucleic Acids : I . Parameter Optimization Based on Small Molecule and Condensed Phase Macromolecular Target Data. *J. Comput. Chem.* **21**, 86–104 (2000).
 30. Walter, A. J. L. R. R. *Molecular Biology of the Cell.* (2002).
 31. Creighton, T. E. *Proteins: structures and molecular properties.* (W. H. Freeman and Company, 1993).
 32. Kim, Y. C. & Hummer, G. Coarse-grained Models for Simulations of Multiprotein Complexes: Application to Ubiquitin Binding. *J. Mol. Biol.* **375**, 1416–1433 (2008).
 33. Cooke, I. R. & Deserno, M. Solvent-free model for self-assembling fluid bilayer membranes: Stabilization of the fluid phase based on broad attractive tail potentials. *J. Chem. Phys.* **123**, (2005).
 34. Argento, C., Jagota, A. & Carter, W. C. Surface formulation for molecular interactions of macroscopic bodies. *J. Mech. Phys. Solids* **45**, 1161–1183 (1997).

35. McIntosh, T. J., Magid, A. D. & Simon, S. A. Interactions between charged, uncharged, and zwitterionic bilayers containing phosphatidylglycerol. *Biophys. J.* **57**, 1187–1197 (1990).
36. Aeffner, S., Reusch, T., Weinhausen, B. & Salditt, T. Energetics of stalk intermediates in membrane fusion are controlled by lipid composition. *Proceedings of the National Academy of Sciences* **109**, E1609–E1618 (2012).
37. McIntosh, T. J. & Simon, S. A. Hydration and steric pressures between phospholipid bilayers. *Annu. Rev. Biophys. Biomol. Struct.* **23**, 27–51 (1994).
38. Marra, J. Direct measurement of the interaction between phosphatidylglycerol bilayers in aqueous electrolyte solutions. *Biophys. J.* **50**, 815–825 (1986).
39. Ohsawa, K., Murata, M. & Ohshima, H. Zeta potential and surface charge density of polystyrene-latex; comparison with synaptic vesicle and brush border membrane vesicle. *Colloid Polym. Sci.* **264**, 1005–1009 (2005).
40. Pekker, M. & Shneider, M. N. The surface charge of a cell lipid membrane. *arXiv Prepr. arXiv* 1401–1407 (2014).
41. Gao, Y. *et al.* Single Reconstituted Neuronal SNARE Complexes Zipper in Three Distinct Stages. *Science* **337**, 1340–1343 (2012).
42. Risselada, H. J., Kutzner, C. & Grubmüller, H. Caught in the act: visualization of SNARE-mediated fusion events in molecular detail. *ChemBiochem* **12**, 1049–55 (2011).
43. Risselada, H. J. & Grubmüller, H. How SNARE molecules mediate membrane fusion: Recent insights from molecular simulations. *Current Opinion in Structural Biology* **22**, 187–196 (2012).

44. Zorman, S. *et al.* Common intermediates and kinetics, but different energetics, in the assembly of SNARE proteins. *Elife* **3**, e03348 (2014).
45. Malsam, J. *et al.* Complexin arrests a pool of docked vesicles for fast Ca²⁺-dependent release. *The EMBO Journal* **31**, 3270–3281 (2012).
46. Hernandez, J. M. *et al.* Membrane Fusion Intermediates via Directional and Full Assembly of the SNARE Complex. *Science* **336**, 1581–1584 (2012).
47. Chernomordik, L. V & Kozlov, M. M. Mechanics of membrane fusion. *Nat. Struct. Mol. Biol.* **15**, 675–683 (2008).
48. Takamori, S. *et al.* Molecular Anatomy of a Trafficking Organelle. *Cell* **127**, 831–846 (2006).
49. Knowles, M. K. *et al.* Single secretory granules of live cells recruit syntaxin-1 and synaptosomal associated protein 25 (SNAP-25) in large copy numbers. *Proc. Natl. Acad. Sci. U. S. A.* **107**, 20810–20815 (2010).
50. van den Bogaart, G. *et al.* One SNARE complex is sufficient for membrane fusion. *Nat. Struct. Mol. Biol.* **17**, 358–364 (2010).
51. Hua, Y. & Scheller, R. H. Three SNARE complexes cooperate to mediate membrane fusion. *Proc. Natl. Acad. Sci. U. S. A.* **98**, 8065–8070 (2001).
52. Shi, L. *et al.* SNARE Proteins: One to Fuse and Three to Keep the Nascent Fusion Pore Open. *Science* **335**, 1355–1359 (2012).
53. Megighian, A. *et al.* Evidence for a radial SNARE super-complex mediating neurotransmitter release at the *Drosophila* neuromuscular junction. *J Cell Sci* **126**, 3134–3140 (2013).
54. Acuna, C. *et al.* Microsecond dissection of neurotransmitter release: SNARE-

- complex assembly dictates speed and Ca²⁺ sensitivity. *Neuron* **82**, 1088–1100 (2014).
55. Hernandez, J. M., Kreutzberger, A. J. B., Kiessling, V., Tamm, L. K. & Jahn, R. Variable cooperativity in SNARE-mediated membrane fusion. *Proc. Natl. Acad. Sci. U. S. A.* 1–6 (2014). doi:10.1073/pnas.1407435111
 56. Prashad, R. C. & Charlton, M. P. SNARE zippering and synaptic strength. *PLoS One* **9**, (2014).
 57. Hua, S. Y. & Charlton, M. P. Activity-dependent changes in partial VAMP complexes during neurotransmitter release. *Nat. Neurosci.* **2**, 1078–1083 (1999).
 58. Sørensen, J. B. *et al.* Sequential N- to C-terminal SNARE complex assembly drives priming and fusion of secretory vesicles. *EMBO J.* **25**, 955–966 (2006).
 59. Walter, A. M., Wiederhold, K., Bruns, D., Fasshauer, D. & Sørensen, J. B. Synaptobrevin N-terminally bound to syntaxin-SNAP-25 defines the primed vesicle state in regulated exocytosis. *J. Cell Biol.* **188**, 401–413 (2010).
 60. Li, F. *et al.* A half-zippered SNARE complex represents a functional intermediate in membrane fusion. *J. Am. Chem. Soc.* **136**, 2456–2464 (2014).
 61. Jahn, R. & Fasshauer, D. Molecular machines governing exocytosis of synaptic vesicles. *Nature* **490**, 201–207 (2012).
 62. Schlick, T. *Molecular modeling and simulation: an interdisciplinary guide.* (Springer, 2002).
 63. Kubo, R. The fluctuation-dissipation theorem. *Reports on Progress in Physics* **29**, 255–284 (2002).
 64. Bruce Alberts Julian Lewis Keith Roberts, and Peter Walter, Alexander Johnson,

- M. R. *Molecular Biology of the Cell*. (Garland Science, 2002).
65. Ohsawa, K., Ohshima, H. & Ohki, S. Surface potential and surface charge density of the cerebral-cortex synaptic vesicle and stability of vesicle suspension. *Biochim Biophys Acta* **648**, 206–214 (1981).
 66. Deserno, M. Fluid lipid membranes – a primer.
 67. Kweon, D. H., Kim, C. S. & Shin, Y. K. The membrane-dipped neuronal SNARE complex: A site-directed spin labeling electron paramagnetic resonance study. *Biochemistry* **41**, 9264–9268 (2002).
 68. Kweon, D.-H., Kim, C. S. & Shin, Y.-K. Regulation of neuronal SNARE assembly by the membrane. *Nat. Struct. Biol.* **10**, 440–447 (2003).
 69. Kim, C. S., Kweon, D. H. & Shin, Y. K. Membrane topologies of neuronal SNARE folding intermediates. *Biochemistry* **41**, 10928–10933 (2002).
 70. Stein, A., Weber, G., Wahl, M. C. & Jahn, R. Helical extension of the neuronal SNARE complex into the membrane. *Nature* **460**, 525–528 (2009).
 71. Marko, J. F. & Siggia, E. D. Stretching DNA. *Macromolecules* **28**, 8759–8770 (1995).
 72. Bustamante, C., Marko, J. F., Siggia, E. D. & Smith, S. Entropic elasticity of lambda-phage DNA. *Science* **265**, 1599–1600 (1994).

Chapter 3: Coarse-Grained Model of SNARE Shows that Partial Assembly and Helicity are Required for Quick Zippering

Neurotransmission is a highly regulated and dynamic process. Neuronal transmitters are released via the fusion of synaptic vesicles with the presynaptic membrane. Vesicles become attached to the membrane by the SNARE complex (soluble N-ethylmaleimide-sensitive factor attachment protein receptor) the primary molecular machinery driving adhesion between vesicles and the membrane. The SNARE complex represents a four helical bundle, and its full assembly is thought trigger the fusion of the synaptic vesicle and the release of transmitters. One of central problems in understanding the transmitter release is the dynamics of SNARE assembly. We investigated SNARE assembly using a coarse grained model of the SNARE complex with chemical specificity that is calibrated using single molecule experiments and all atom molecular dynamics simulations. Simulations of SNARE unzippering, steered under force control and calibrated by experimental data, were used to set up initial disassembled SNARE states. From these states the assembly process was simulated. We found that the time required for SNARE assembly depends non-linearly on the degree of initial unraveling, and it grows approximately exponentially with the increased number of separated layers of the SNARE complex. This finding supports the idea that the SNARE complex in its pre-fusion state is partially zippered, possibly by means of molecular chaperones.

3.1 Introduction

Neurotransmission, the primary method by which neurons communicate, occurs sequentially after the docking and fusion of synaptic vesicles at the synaptic membrane¹. In order for this process to occur, i.e., for the vesicle to dock and then to fuse with the plasma membrane, there must be some adhesive machinery in place to overcome the electrostatic and hydration repulsion between the two. SNARE (soluble N-ethylmaleimide-sensitive factor attachment protein receptor)^{2,3} proteins are predominantly responsible for providing this adhesive force. SNARE proteins comprise a 4 helix bundle of the vesicle bound Synaptobrevin (Syb or v-SNARE) and the plasma membrane bound t-SNARE which includes Syntaxin (syx) and SNAP-25; the latter is itself made up of two helical domains (SN1) and (SN2)^{4,5}. When t-SNARE and v-SNARE interact with one another, they zipper together to form a parallel four-helix bundle. This zippering force provides adhesive forces and energies between the vesicle and the membrane to overcome their otherwise mutual repulsion.

While this SNARE bundle is the core conserved motif, there are many other molecular players that contribute to the process of neurotransmission from vesicle docking to fusion and exocytosis, and the overall process is significantly more complicated. Because this process is indispensable to neuron function, there have been many experimental and simulation studies on the sequence of events and factors that mediate vesicle tethering, docking, and fusion^{1,6-8}. Membrane tethering factors including coiled-coil homodimers and multisubunit tethering complexes (MTCs) are responsible for bringing vesicles and membranes close to one another in preparation to fuse (also known as “tethering”)^{1,9-11}.

After vesicle to membrane tethering has been established, the vesicle is docked at the membrane or brought within 1-4nm of the synaptic membrane² in order to prepare for fusion with the help of MTCs, SM proteins (Sec1-Munc18), and SNAREs¹.

Although the main molecular players have been established, our knowledge of the mechanistic details of how they work remains unclear. For instance, it is still unclear how SNARE assembly actually occurs. The x-ray crystal structure¹² as well as the position of several crucial adhesive layers within the SNARE bundle^{13,14} have been confirmed. Experiments have been done to determine the structure of individual helices¹⁵. Some studies have been conducted on the disassembly/unzippering pathway of SNARE including optical and magnetic tweezers experiments^{6,16}, all-atom unzippering simulations⁷, and coarse-grained (CG) simulations⁸. Optical and magnetic tweezers experiments provide crucial overall experimental details regarding the assembly process. However, these experiments do not reveal details and sometimes display kinetics that are very different in rates than those observed *in vivo*. Therefore, there is a strong opportunity for molecular simulation studies to contribute to our understanding of these processes.

A recent study suggested that Munc18 may act as a template for the SNARE assembly process¹⁷. It is known that during the docking process, Syx interacts with Munc18¹⁸. Syx can take on two conformations: a “closed” state in which the helix folds back onto itself, forms a 3 helix bundle, and is unable to bind with Syb and an “open” state where Syx is bound to SNAP25 and is capable of forming the SNARE bundle with Syb^{18,19}. Recently two x-ray structures were reported including SM proteins that shed some light on their interaction with the SNARE assembly process¹⁷. The first X-ray structure is that of Qa-SNARE Vam3 and the SM protein Vps33 which closely resembles the interaction between

Munc18 and Syx¹⁷. The second x-ray structure is that of R-SNARE Nyv1 and the SM protein Vps33 which closely resembles the interaction between Munc18 and Syb¹⁷. The helical hairpin of Vps33 (Munc18) that would normally bind to R-SNARE (Syb) is bent up back onto itself when Qa-SNARE (Syx) is bound in its “closed” state in order to prevent steric hindrances with the 3 helix bundle¹⁷. However, it is hypothesized that when Qa-SNARE (Syx) is in its “open” state, this helical hairpin would be free to bind with R-SNARE (Syb) due to Syx having a more linear confirmation¹⁷. When these two X-ray structures were superimposed onto one another, Syb and Syx were positioned so that SNARE bundle formation would be favorable because the bundle would be in the half zippered position¹⁷. In addition to serving as a template for SNARE assembly, Syb and Syx association with Munc18 would also provide an explanation for how Syb forms a helix despite the fact that by itself, i.e., when it is not associated with the SNARE, it is known to be highly unstructured²⁰.

Qa-SNARE, Vps33, Nyv1, and R-SNARE have aided in the hypothesis that Munc18 serves as a template for SNARE assembly, but this is far from the end of the story. In the work of Baker et al.¹⁷ there is no single X-ray structure of Munc18, Syb, and Syx demonstrating a “snapshot” of this assembly process. In order to ensure that Munc18 is necessary for SNARE assembly, additional experiments including the Qa-SNARE, Vps33, Nyv1, and R-SNARE would need to be completed in order to show that the Qa-SNARE/Vps33 and the R-SNARE/Nyv1 can be combined in vitro or in vivo. There is also an alternate mechanism for SNARE assembly that has been proposed in which the small helical fragments of Syb serve as nucleation sites for Syb folding and bundle formation²¹.

This model we will discuss as the “self-templating” model in this work. In it the assembly of SNARE largely depends on the formation of the Syb helix.

Gao et al.⁶ studied the relationship between SNARE helicity and SNARE unzipping/zippering in depth. The SNARE bundle was unzipped at the C-termini of Syb/Syx using optical tweezers, and the reverse process was used to study the SNARE zippering process, also producing accompanying force-displacement relationships. From this study, Gao et al.⁶ determined that SNARE unzipping/zippering takes place in stages that are highly dependent on the helicity of Syb and found the distribution of probabilities for Syb unraveling/raveling as a function of applied force. These SNARE unzipping/zippering stages were confirmed by a magnetic tweezers study¹⁶.

Kinetics of SNARE assembly are difficult to study because the process is dynamic and occurs at timescales of $< 1\mu\text{s}$, making visualization quite difficult. Therefore, molecular simulations can prove very useful. We have previously developed a CG model of the SNARE complex that has been calibrated by experimental and all-atom simulation results²². This model was previously combined with a continuum model of the synaptic vesicle and membrane and used to determine the number of SNAREs required for synaptic vesicle to membrane docking. Steered simulations of separating the SNARE complex under displacement control were used to unzip the SNARE bundle and determine a force displacement relationship. Because of its CG nature and reduced degrees of freedom, our model can easily access the microsecond timescales required and can be adjusted to incorporate the experimentally determined probabilities of helix ‘melting’ as determined by Gao et al.⁶. In this work we use our CG model of the SNARE complex to study the assembly process. Implementing experimental knowledge of the SNARE unzipping

process we produce various initial states for SNARE-assembly simulations, as mimics of Munc18 presence and self-templating. Thus we address the question of whether the presence of a chaperone, such as Munc18, or SNARE self-templating are required for SNARE bundle assembly.

3.2 Materials and Methods

3.2.1 Simulation Methods

CG MD simulations of the SNARE bundle were conducted using Brownian dynamics (BD) (Refer to Chapter 1 and Chapter 2 for more details on this method). The CG model of SNARE, shown in Fig. 3.1, is protein-residue based, each one being represented by a bead at the location of its alpha carbon.

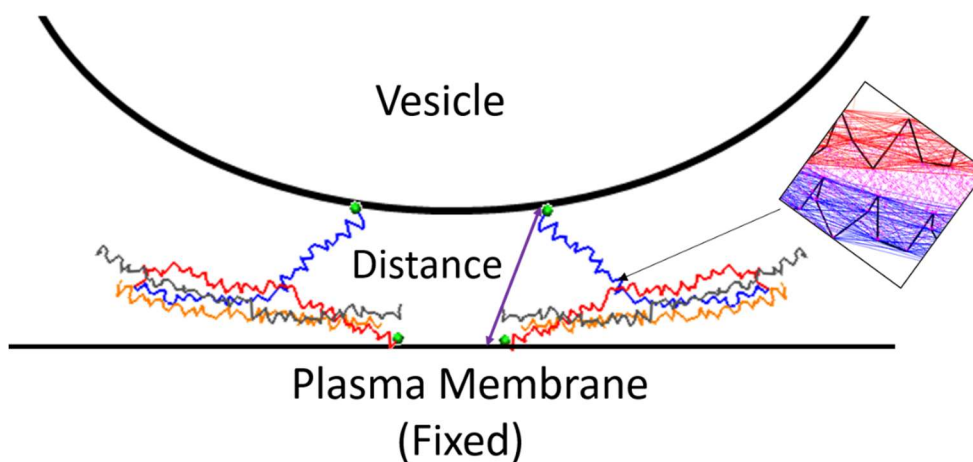


Figure 3.1 A schematic in which the synaptic vesicle and plasma membrane are shown along with the CG model of SNARE including Syb (*blue*), Syx (*red*), SN1 (*gray*), and SN2 (*orange*). The pulling beads (*green*) for Syb and Syx are indicated where the Syx pulling bead is held fixed. An example of the ENM springs are shown in the inset for a portion of Syb (*blue*) and Syx (*red*) along with the MJ interactions between the two helices (*pink*). The Syb-Syx C-terminal distance is indicated as well (*purple double arrowed line*).

Interhelical interactions were modeled using an elastic network model (ENM)^{23,24} and intrahelical interactions were modeled using Miyazawa and Jernigan (MJ) forces²⁵⁻²⁷. This set of interhelical and intrahelical interactions provide chemical specificity and were calibrated using AA simulations and experimental results. The CG model used is described in detail in Chapter 2 and Fortoul et al.⁸ Several adjustments to its force-field parameters were made specifically because most of the work in Chapter 2 and Fortoul et al.²² was done at 0 K whereas here we conduct simulations at 300 K (see Appendix for more information). A critical enhancement of the model is the ability to capture transitions between helical and random coil states by removal or reinstatement of the elastic network bonds (the backbone is always retained), based on single-molecule stretching experimental data.

In all simulations performed the initial configuration was determined using the x-ray structure 1N7S^{7,13,22} that was simulated for 40 ns using all-atom AA MD in NAMD⁷. This AA structure was coarse-grained and relaxed for 20 ns using BD as described above. After the 20 ns BD relaxation, a fixed bead was attached to the C-terminal bead of Syx, and a second fixed bead was attached to the C-terminal bead of Syb. The SNARE structure with the two fixed beads was then relaxed using BD for another 20 ns. All simulations were performed using the initial configuration determined by the final timestep of the 20 ns BD run with fixed beads (see Appendix for more information).

3.2.2 First Step: Separating Syb from the SNARE Under Force Control

In this study steered dynamics under force control (FC) simulations were used to unzipper the SNARE bundle to set up initial states for SNARE assembly studies. A fixed bead was

attached to the C-terminal end of Syx and a pulling bead was attached to the C-terminal end of Syb, as shown in Fig. 3.1, with an applied force of $5.6E-2$ pN/ns along the vector connecting the two beads. This forcing rate was chosen by running simulations with decreasing forcing rate until it was slow enough that the system was close to equilibrium as determined by agreement between mean forces on the two pulling beads (Appendix, Fig. A3.2).

It was assumed in the model that, because Syx, SN1, and SN2 are associated with one another throughout the simulations, their structures remain helical⁶. However there is evidence that when Syb is not associated with the SNARE bundle it is largely unstructured²¹. In our previous work, Syb remained helical because the focus for docking was primarily on small SNARE separations²². However, for this work, large SNARE un zipperings are required to set up initial states for the study of assembly. A valid concern is therefore whether the unraveling of Syb must be considered in setting up the initial state for re-assembly.

As determined by Gao et al.⁶, there are 3 separate regions of Syb which unravel as a group of residues: (1) the linker domain (LD) which was not present in the x-ray structure or our model (reversible), (2) from the LD to the ionic layer (IL) (reversible), and (3) from the ionic layer to the remaining Syb structure (irreversible). These experimental results can be represented by a Markov chain model, as described in Fig. 3.2A and its caption.

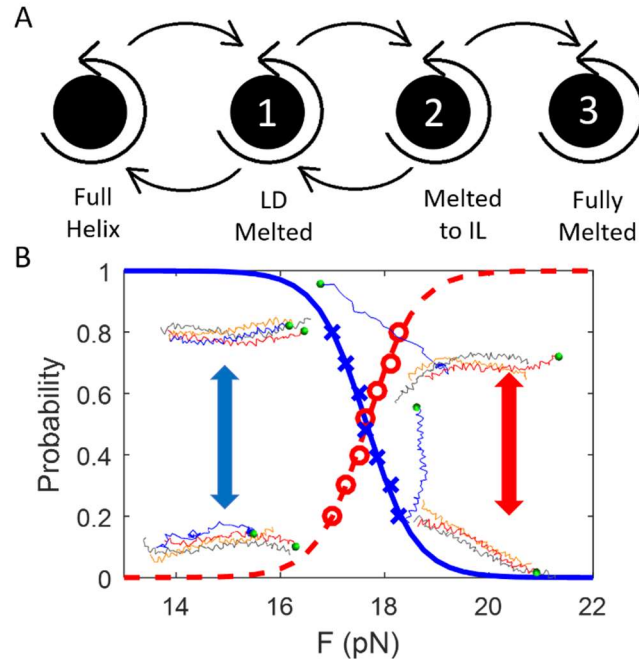


Figure 3.2 (A) A Markov chain model is shown for the unfolding/folding states of Syb for increasing force, according to Gao et al.⁶ Syb starts out fully helical and has a probability for the LD to melt or to remain fully helical. If the LD is melted, Syb is in state 1 where there is a probability to remain in that state, refold or melt to the IL. If Syb melts to the IL, it is in state 2 where there is a probability to remain in that state, refold to the LD, or to melt completely. If Syb is fully melted, this is irreversible and it remains in state 3. (B) The analytical probability of LD and IL being in a folded (*solid blue*) or unfolded (*dashed red*) state are shown for Syb as functions of applied force. These match the experimentally estimated values of P_u (*red circles*) and P_f (*blue X's*) from Gao et al. At low forces, there is reversible transition between a folded and unfolded state (shown with a blue arrow and structures) with the folded state being favored. At high forces, there is reversible transition between a folded and unfolded state (shown with a red arrow and structures) with the unfolded state being favored.

Because the structure we have used in our work lacks the LD, in our model, Syb only has the latter two unfolding/folding events. The Markov chain drawn in Fig 3.2A was implemented as a Monte Carlo method executed every ten BD steps in the following way. If Syb is completely folded, it can reversibly unfold up to the ionic layer. If Syb is already unfolded up to the ionic layer, it can either refold up to the C-terminus or completely

unfold. However, if Syb is completely unfolded, this event is considered irreversible (for increasing applied force). Unfolding or melting of a certain portion of the Syb helix is implemented as removal of the ENM springs for that specific region, while leaving the backbone springs intact. The force-dependent probabilities associated with various events in the Markov chain are based on the experimentally determined probability of finding Syb in a folded state, P_F , or unfolded state, P_U (Gao et al.²⁸), modeled as a two-state process with energy landscape biased by applied force, for which the ratio of the probability of folding to the probability of unfolding is determined by

$$\frac{P_F}{P_U} = \exp\left(\frac{\Delta E - F\lambda}{kT}\right) \quad (3.1)$$

where ΔE is the energy difference between the folded and unfolded states, F is the applied force, λ is the transition length, k is Boltzmann's constant, and T is temperature. Details describing the implementation are provided in Appendix; Figure 3.2B shows that the implementation faithfully replicates the experimentally measured probabilities for melting up to IL.

3.2.3 Re-assembly of SNARE

After an initial state was established using FC, assembly simulations were performed by releasing the force on the Syb pulling bead and allowing the SNARE to relax. In initial states where Syb was fully or partially melted two forms of raveling were used (Fig. 3.3): (1) a rapid assembly method mimicking the action of a chaperone, and (2) a distance-based criterion (SNARE self-templating) for helix assembly.

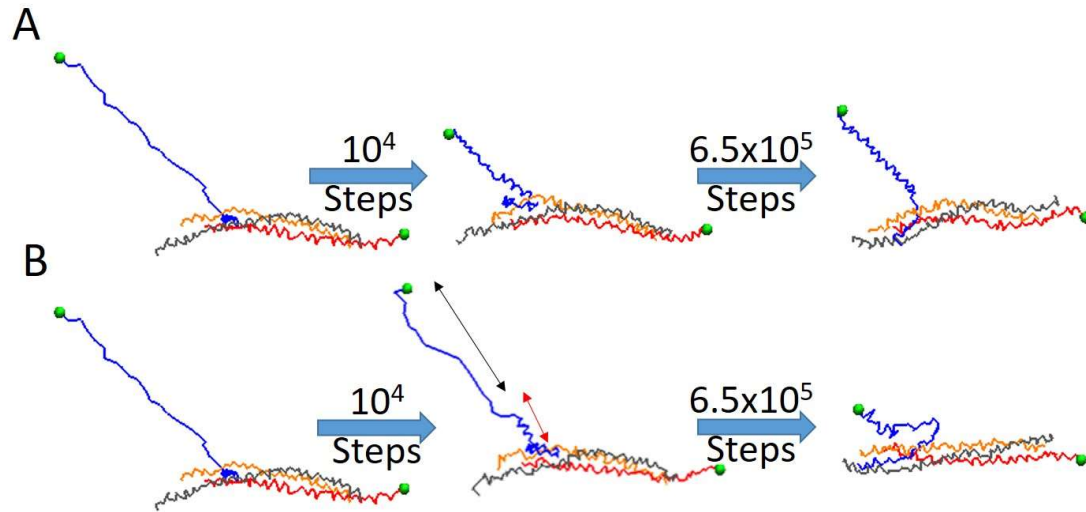


Figure 3.3 Examples of a portion of an assembly simulation are shown using the two methods of helix reformation. Both simulations start from the same initial state produced using the FC method. (A) Rapid helix formation immediately turns on the ENM springs for Syb when the relaxation simulation begins and the applied force is released. (B) The distance criterion method only turns on ENM springs for residues that are within 1 nm of the SNARE bundle. The red arrow shows the portion of the Syb helix that has regained structure due to its close proximity to the bundle. The black arrow shows the portion of the Syb helix that is not within the distance criterion and has not yet regained its helical structure.

In the rapid assembly method, when the FC pulling force is released, all the ENM springs that were previously removed are reinstated. This allows the Syb helix to re-form rapidly, in $<10^4$ timesteps which is seen in Fig. 3.3A. This rapid helix formation method is intended to mimic the presence of a chaperone such as Munc18 that would promote Syb helix formation. In the distance criterion method, the minimum distance between every Syb residue/ bead and the SNARE bundle is determined at each time-step. If this distance is less than the distance criterion of 1 nm, chosen as a characteristic distance for MJ interactions, the ENM springs for that particular bead are replaced (reversibly). This distance criterion

method mimics the action of SNARE self-templating. Upon interaction with the rest of the SNARE bundle, Syb would become helical, creating a zipper-like effect. In Fig. 3B three snapshots are shown during an assembly simulation. An initial state was produced using FC. After 10^4 timesteps only a small portion of the helix that is within close proximity of the SNARE bundle is helical, and the rest of Syb is unstructured. After another 6.5×10^5 timesteps, more of Syb is helical as more of it is associated with the bundle. Part of Syb has actually twisted back onto itself due to its lack of helical structure. This process continues as more of Syb becomes associated with the bundle and turns helical, creating a self-templating effect. See the Appendix for more details on the reassembly methods. The folding/unfolding behavior qualitatively matches the results of Gao et al.'s experiment⁶. However realistically the quantitative time for the distance criterion method folding can only be viewed as a pseudo folding time because the Monte Carlo event of folding does not have a time element associated with it. In the simulation folding occurs on the order of 10s of ns, whereas in reality this is very likely an activated process that could take more several ms¹⁶.

3.3 Results and Discussion

Syb assembly studies were conducted for three separate conditions: (1) fully helical SNARE unzipping and assembly, (2) SNARE unzipping with force based MC Syb melting and assembly with rapid Syb helix formation, and (3) SNARE unzipping with force based MC Syb melting and assembly with distance criterion based Syb helix formation. Case (1) is the base case to study the isolated effects of SNARE assembly

without melting. Case (2) mimics the presence of a chaperone that promotes helix formation prior to assembly. Case (3) represents the self-templating model where the SNARE bundle serves as a template for Syb helix formation and SNARE assembly.

3.3.1 SNARE Unzipping and Assembly with Fully Helical Syb

In the first case of re-assembly studied, the initial state was produced by unzipping under FC while keeping Syb fully helical. Thus, relaxation to assembly following release of the force began with Syb already in a fully helical state.

As was described in the Methods section, a fixed bead was attached to the C-terminal end of Syx and a pulling bead was attached to the C-terminal end of Syb. FC on the Syb C-terminal bead was used in step 1 to completely pull the SNARE bundle apart to a distance of ~20 nm between the Syb and Syx C-termini as shown in Fig. 3.4 (blue trace).

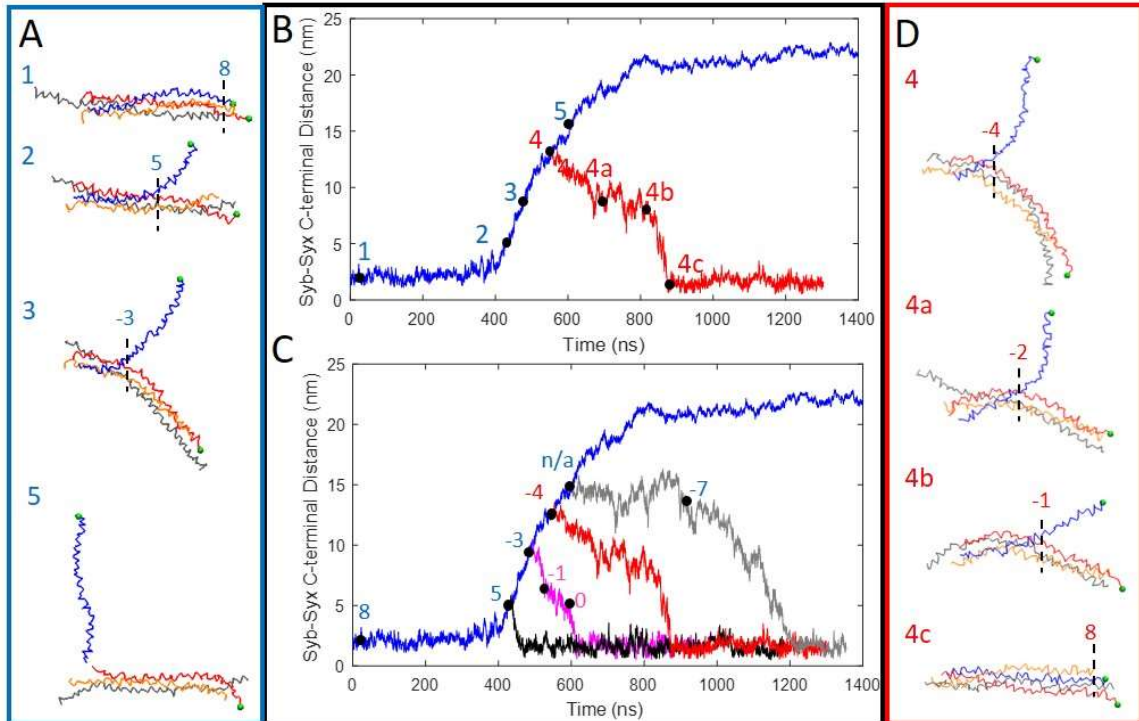


Figure 3.4 The Syb-Syx C-terminal distance is shown as a function of time for fully helical SNARE unzipping (*blue traces (B and C) and snapshots 1-5 (A and D)*) using FC. Snapshots are shown for one unzipping trajectory and one assembly trajectory (*A, B, and D*). The force was released at several points within the unzipping trajectory (*black, magenta, red, and gray traces in C*) and the bundle was permitted to relax. The layer up to which the SNARE bundle is zippered is indicated for all snapshots and for several points in unzipping/assembly (*C*). For small initial SNARE openings of only a couple of layers (*black*) the bundle assembles at a relatively constant fast rate. For intermediate initial openings (*magenta and red*) the bundle starts to assemble initially at a slow rate and then assembles at a faster rate. The snapshots (*4-4c*) are shown for one specific assembly case in this intermediate region. The bundle assembles slowly from layer -4 to layer -1 (near the ionic layer). Then from layer -1 to layer 8 it assembles quickly. For large initial openings, where no layers are in contact (*gray*), the bundle first experiences a plateau and Syb fluctuates at roughly a constant distance from the bundle until layer -7 is assembled, then the bundle assembles at a constant rate. (Only a few of the BD assembly simulations are shown in this figure for clarity.)

At several points during the unzipping trajectory, the force was released on the Syb pulling bead, and the SNARE bundle allowed to relax. For example, point 4 Fig. 3.4B indicates the initial state for a relaxation run beginning at Syb-Syx separation of ~ 5 nm. A

fully assembled SNARE bundle is indicated by a Syb-Syx distance of ~ 2 nm which is a similar Syb-Syx C-terminal distance to that of a relaxed full SNARE bundle taken from the x-ray crystal structure. From Fig. 3.4C it can be concluded that as the starting Syb-Syx separation increases, so does the time required for assembly. For small initial separations of up to ~ 10 nm, the SNARE bundle immediately begins to assemble at a relatively constant rate when the applied force is released and completes assembly in 250 ns or less. Therefore for these cases, the assembly time is less than the time required to unzip the bundle to form the initial state. For initial separations of ~ 10 nm to ~ 13.4 nm the bundle seems to assemble in two major steps. The bundle initially begins to assemble at one rate until the bundle is zippered up to layer -1 and then the rate of assembly increases until the bundle is fully closed as shown for a 13.4 nm run in Fig. 3.4B and D. Layer -1 is very close to the ionic layer (layer 0), a particularly adhesive contact within SNARE, which is known to help hold SNARE in a partially zippered state⁶. Snapshots are shown in Fig. 3.4D for one of these assemblies. Syb remains helical throughout the relaxation and slowly assembles with the rest of the SNARE bundle. For separations > 13.4 nm, there are again two distinct regions during relaxation. The first region is more of a plateau in which case the Syb's, distance from the bundle, on average, is not changing. During this plateau most of Syb is fluctuating with no contact to the bundle, and at some point there is a transition where the SNARE bundle is in contact at layer -7 and the second region is entered where Syb begins to come in contact with the bundle and assembles. This most likely occurs due to some random fluctuation of Syb bringing it closer to the SNARE bundle and in turn initiating assembly. For even greater initial separation, there is no reassembly within the duration of the simulation.

3.3.2 SNARE Unzipping and Assembly with Syb Melting and Rapid Helix Formation

If Syb is not associated with the SNARE bundle, especially if it is also under applied force, it is known that it is highly unlikely to remain helical^{9,28}. Therefore during the FC Syb unzipping process, melting will realistically occur. An MC force based unraveling criterion was used, as described in the methods section. FC was applied to Syb, as was done in 3.3.1, to create an initial unzipped state for SNARE as shown in Fig. 3.5.

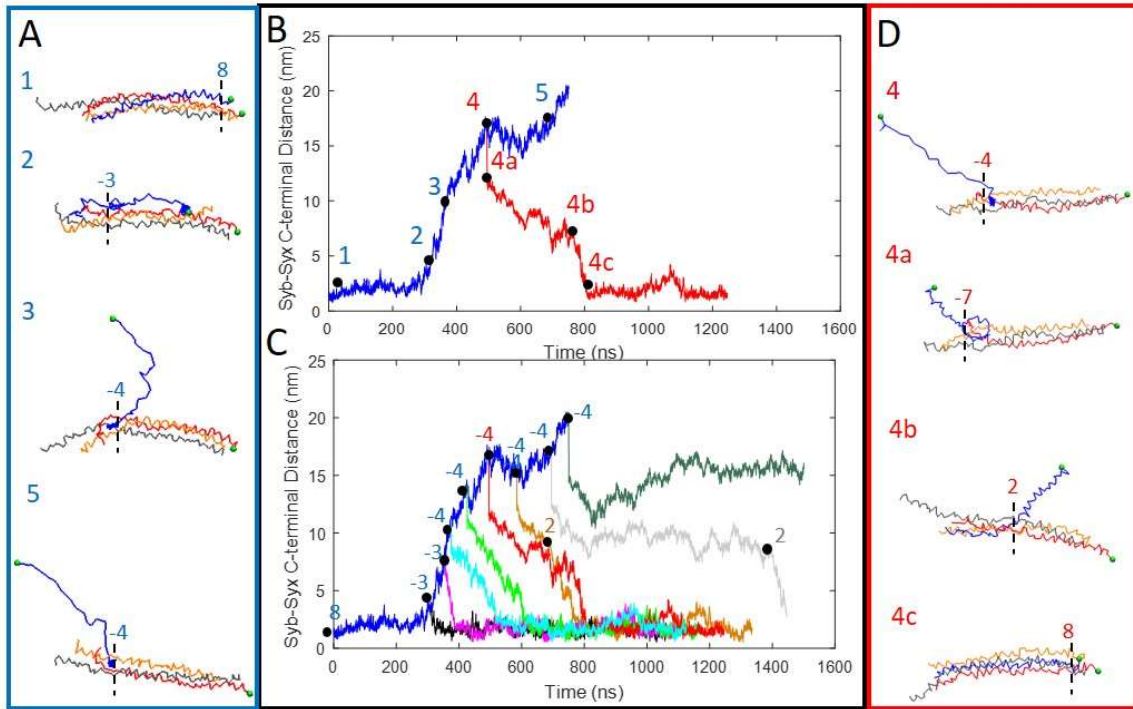


Figure 3.5 The Syb-Syx C-terminal distance is shown as a function of time for SNARE unzipping using FC with a MC force based unraveling criterion (*blue traces (B and C) and snapshots 1-5 (A and D)*). Snapshots are shown for one unzipping trajectory and one assembly trajectory (*A, B, and D*). The force was released at several points within the unzipping trajectory (*black, magenta cyan, green, red, brown, and gray traces in C*) and the bundle was permitted to relax. The layer up to which the SNARE bundle is zippered is indicated for all snapshots and for several points in unzipping/assembly (*C*). When the force was released, the ENM springs were immediately reinstated for Syb, and helix formation occurred in $<10^4$ timesteps. For small initial SNARE openings of up to 10 nm (*black, magenta, and cyan*) the bundle assembles at a relatively constant fast rate. For intermediate initial openings (*green, red, and brown*) the bundle starts to assemble initially at a slow rate and then assembles at a faster rate. The snapshots (*4-4c*) are shown for one specific assembly case in this intermediate region. The bundle assembles slowly from layer -4 to layer 2 (near the ionic layer). Then from layer 2 to layer 8 it assembles quickly. For large initial openings (*grey*) the bundle first experiences a plateau and Syb fluctuates at roughly a constant distance from the bundle until layer 2 is assembled, then the bundle assembles at a constant rate. For the largest initial separations (*dark green*) SNARE does not re-assemble within the duration of the simulation. Note that even for small separations of ~ 5 nm, the bundle is unzipped to layer -3. This is due to the unraveling of Syb which disrupts the interaction between Syb and Syx/SNAP25. (Only a few of the BD assembly simulations are shown in this figure for clarity.)

Several points within the unzipping trajectory were chosen as initial states for the relaxation/assembly simulations as was done for the full helix simulations. During the first timestep of the relaxation simulation, the ENM for Syb was immediately reinstated as described in the methods section. Full Syb helix formation occurred within 10^4 timesteps which accounts for the rapid decrease in end to end distance as seen in relaxation simulations above ~ 10 nm in Fig. 3.2. As the SNARE end to end separation of the initial structures increased, the relaxation times to an assembled SNARE also increased.

If we define the initial separation to be the distance between the C termini *after* re-formation of the helix, the results for these simulations are very similar to those of the fully helical simulations previously discussed. For initial separations of < 11 nm, SNARE assembly occurs at a relatively constant rate indicating that the SNARE bundle is closing rather easily. For separations from ~ 11 nm to ~ 15 nm or so, there is first a slow assembly region and then a fast assembly region as in Fig. 3.4C. Snapshots are shown in Fig. 3.4D for one of these assemblies. The transition between assembly rates is seen when the bundle has assembled up to layer 2, which again is very close to the ionic layer, layer 0. Syb quickly takes on its helical structure and steadily begins to assemble. When the initial separation is > 15 nm again there is a plateau region followed by an assembly region. As with the intermediate openings, this transition occurs at layer 2 as well. Even though the initial state before assembly was created very differently in that the melting of Syb is considered, the main conclusions from the helical simulations in 3.3.1 hold true. There are a range of initial displacements that allow for quick and easy assembly, then a range that have a transition from a slow to fast assembly, a range of displacements where there is a

plateau and then an assembly region, and finally for sufficiently large initial opening SNARE no longer assembles within the time frame of the simulation.

This rapid helical formation is intended to mimic the effect on assembly of the presence of a chaperone such as MUNC18. When Syb and Syx are bound to MUNC18, they are thought to be highly helical¹⁷. Therefore, the interaction of free Syb with MUNC18 would promote Syb helix formation (as was simulated by replacing the ENM springs). Syx and SNAP25 remained helical throughout the entire process because they are assumed to be preassembled and helical before their interaction with Syb^{1,6}.

3.3.3 SNARE Unzipping and Assembly with Syb Melting and Helix Formation with Distance Criterion

The alternative hypothesis for SNARE assembly is that it is through self-templating²¹. Syb is nonhelical when not associated with the SNARE bundle. However, if the SNARE bundle is initially partially assembled, the bundle itself can act as a site of helix nucleation. As Syb residues come within close proximity of the SNARE bundle, they take on their helical structure. Therefore in the distance criterion method, residues reversibly take on a helical conformation when they are associated with or close to the SNARE bundle. The SNARE unzipping simulation was performed in the same manner as 3.3.2 as is shown in Fig. 3.6.

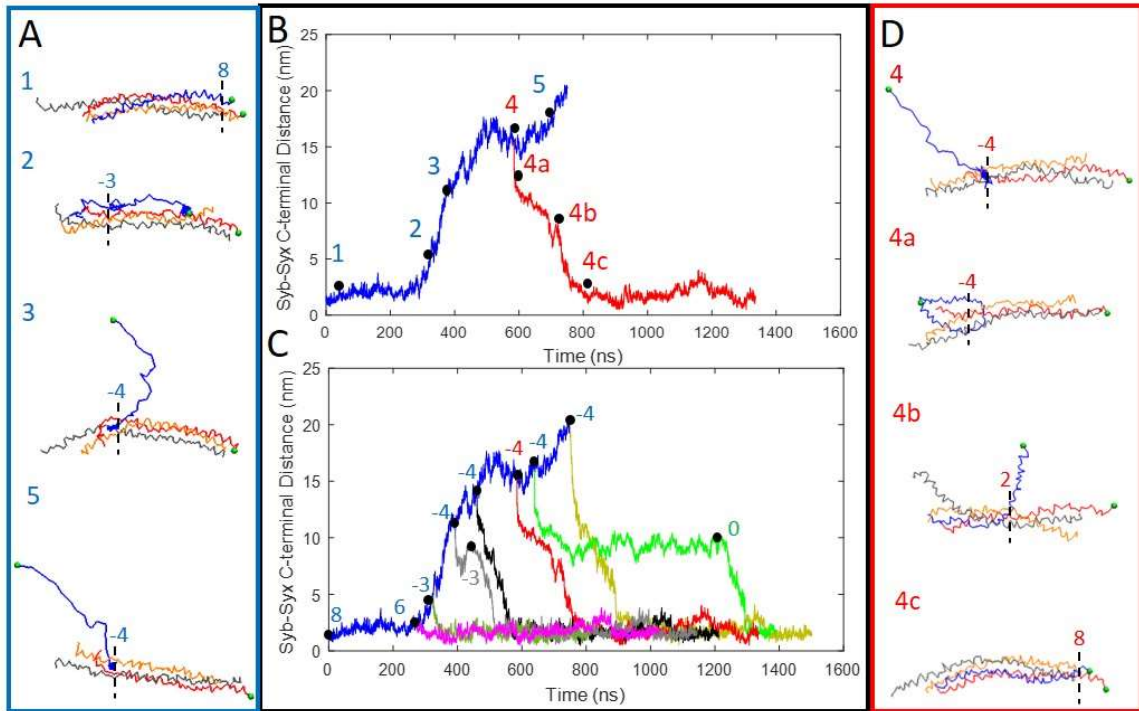


Figure 3.6 The Syb-Syx C-terminal distance is shown as a function of time for SNARE unzipping using FC with a MC force based unraveling criterion (*blue traces (B and C) and snapshots 1-5 (A and D)*). Snapshots are shown for one unzipping trajectory and one assembly trajectory (*A, B, and D*). The force was released at several points within the unzipping trajectory (*magenta, dark green, gray, black, red, green and yellow green in C*) and the bundle was permitted to relax. The layer up to which the SNARE bundle is zippered is indicated for all snapshots and for several points in unzipping/assembly (*C*). When the force was released, the ENM springs were reversibly replaced using a distance criterion as described in the methods section. For small initial SNARE openings of up to 10 nm (*magenta, dark green, grey, and black*) the bundle assembles at a relatively constant fast rate. For intermediate initial openings (*red and yellow green*) the bundle starts to assemble initially at a slow rate and then assembles at a faster rate. The snapshots (*4-4c*) are shown for one specific assembly case in this intermediate region. The bundle assembles slowly from layer -4 to layer 2 (near the ionic layer). Then from layer 2 to layer 8 it assembles quickly. For large initial openings (*green*) the bundle first experiences a plateau and Syb fluctuates at roughly a constant distance from the bundle until layer 0 is assembled, then the bundle assembles at a constant rate. Note that even for small separations of ~5 nm, the bundle is unzipped to layer -3. This is due to the unraveling of Syb which disrupts the interaction between Syb and Syx/SNAP25. (Only a few of the BD assembly simulations are shown in this figure for clarity.)

Several points within the unzipping trajectory were chosen as initial states for the relaxation/assembly simulations. During the relaxation simulations, the ENM springs are slowly reinstated using the distance criterion. As described in sections 3.3.1 and 3.3.2, as the initial SNARE end to end distance is increased, so is the time required for assembly. Above an initial Syb-Syx distance of ~ 15 nm this correlation is not as distinct. For example, the simulation which started at 16 nm assembles much slower than the simulation started at 20 nm. However, it is important to note that the time for helical reformation must also be taken into account in this system. In 3.3.1 helical formation was not considered at all, so there was a clear and monotonic relation between initial distance and assembly time. In 3.3.2 the Syb helices were reformed very quickly and had little effect on assembly time, so the trend was also more obvious. Thus, it appears that assembly of the SNARE bundle is much more rapid if Syb, Syx, and SNAP25 are helical. Therefore in this case the assembly time is a combination of the time required to reform the Syb helix as well as to assemble the bundle. An example of this is seen in the second SNARE snapshot in Fig. 3.6 where Syb has folded back on itself in a partially helical form, however in a later snapshot Syb is fully helical and assembling properly. There is a balance between helix formation and bundle assembly.

However despite the differences between the fully helical model, rapid helix reassembly, and distance criterion models we again have the same robust results. For smaller separations, assembly occurs quickly at a constant rate. For moderate separations, assembly occurs slowly at first and then rapidly with the transition again occurring at layer 2 near the ionic layer. For large separations, there is a plateau region followed by assembly with a transition occurring at the ionic layer.. The initial SNARE separation is indicative

of the propensity and time to assembly, and assembly is most likely dependent on SNARE helicity.

In the unraveling studies in Fig. 3.5 and Fig. 3.6 it should also be noted that for the forces applied in this simulation, the bundle never unzips past layer -4. In an experimental study by Wiederhold et al.¹⁴, layers -4 to -2 were determined to be the trigger site of the SNARE coiled coil bundle formation. When two residues within these layers were mutated (Syb^{N49A, V50A}), SNARE assembly in solution was greatly compromised. In a second mutation (Syb^{I45A, M46A}), this effect was even more prominent. In both the fully helical case (3.3.1) and the rapid reassembly case (3.3.2), layer -2 was determined to be when the slow to fast assembly transition occurred for intermediate SNARE openings again confirming that this could be due to these layers being the location of the coiled coil trigger site.

3.3.4 Combining the Results of Fully Helical Syb and Rapid Helix Reformation Case

In order to determine the correlation between SNARE assembly time and initial Syb-Syx C-terminal separation, the fully helical case (3.3.1), the rapid helix formation (3.3.2), and the distance criterion (3.3.3) cases were analyzed. The SNARE assembly time is shown as a function of the initial Syb-Syx C-terminal distance in Fig. 3.7.

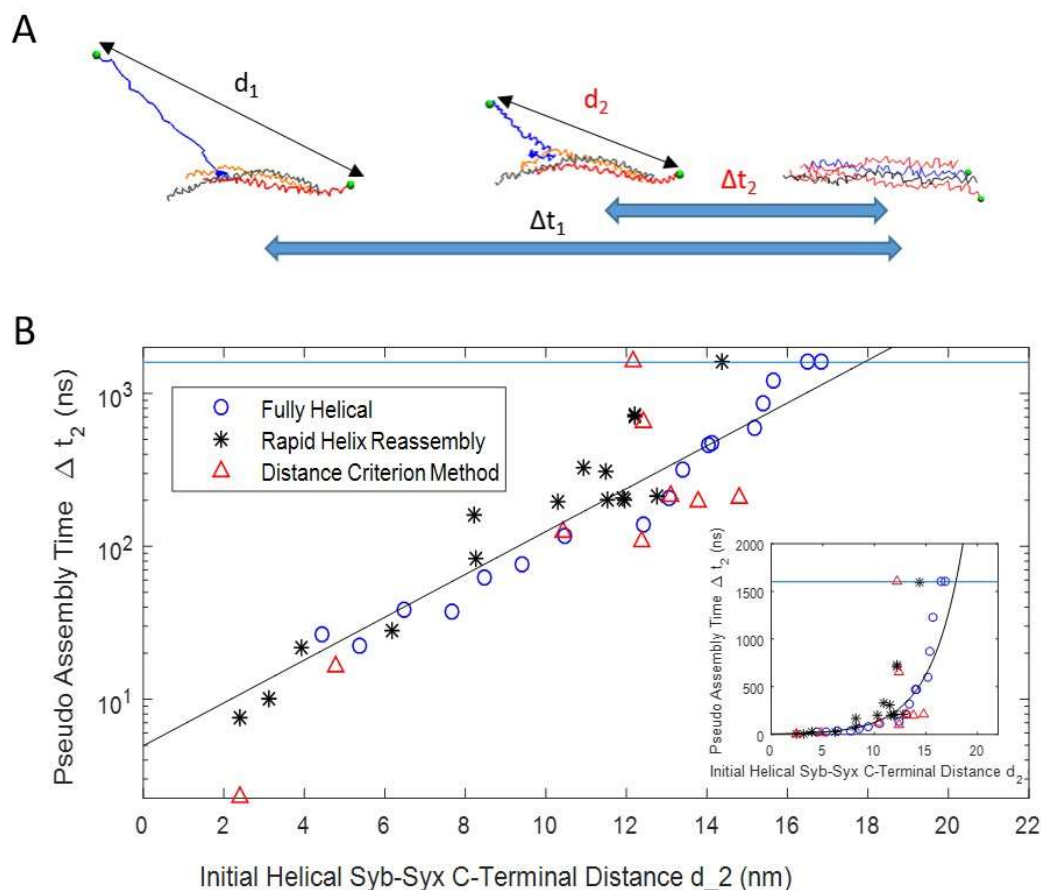


Figure 3.7 (A) A schematic is shown defining pseudo assembly time. Initial Syb-Syx C-Terminal distance, d_1 , is that distance at the start of a relaxation simulation when the force is released. The time required from that point to SNARE bundle formation is defined as pseudo assembly time Δt_1 . Initial helical Syb-Syx C-Terminal distance, d_2 , is the Syb-Syx distance during a relaxation simulation when Syb first becomes helical. The time required from that point to SNARE bundle formation is defined as pseudo assembly time Δt_2 . (B) Δt_2 as a function of d_2 was fitted with an exponential function, $\Delta t_1 = 4.96ns \exp\left(\frac{d_1}{3.10nm}\right)$. Fully helical (*circle*), rapid helix reassembly (*asterisk*), and distance criterion method (*triangle*) cases follow the same trend when only helical distance is taken into account.

In order to compare the three simulation types, the “Initial Syb-Syx C-Terminal Distance” used is the distance during relaxation when SNARE is first helical again. In the case of the full helix runs, this would be the first timestep, for the rapid helix formation simulations

this is at $<10^4$ timesteps, and for the distance criterion runs it varied from the first timestep to $\sim 10^5$ timesteps depending on the structures. The assembly time noted was the change in time from the initial helix formation to full SNARE assembly. The SNARE bundles were assumed to be assembled when the Syb-Syx C-terminal distance was less than ~ 1.8 nm. This criterion was determined by the initial distance for a relaxed CG fully formed SNARE bundle derived from the x-ray crystal structure.

For the three sets of simulations there is a robust conclusion that there is exponential growth in pseudo assembly time as a function of initial Syb-Syx C-terminal distance. Because the Monte Carlo method is probabilistic and independent of time, the times indicated in Fig. 3.7 are only pseudo assembly times. Syb helical folding occurs on the order of ms, to s depending on the degree of unfolding¹⁶, therefore the times presented in Fig. 3.7 are mainly a consequence of helical assembly. However, this study does show that assembly time of SNARE helices for a given degree of opening is independent of how the initial state was determined (with or without unraveling). A characteristic Syb-Syx C-terminal distance of 3.10nm was extracted from the exponential fit shown in Fig. 3.7. This distance is when the SNARE bundle is first starting to unzip its adhesive layers, as shown in Figs. 3.4C, 3.5C, and 3.6C.

For a fully disassembled SNARE, the assembly time including folding is on the order of seconds¹⁶, which is an unrealistic time for evoked vesicle to membrane fusion which occurs on the order of 10s of ms. Our study shows that a partially assembled SNARE that is primarily helical can assemble in ~ 100 ns which is a more realistic assembly time for evoked vesicle to membrane fusion to occur. This priming step to partially zipper SNARE and promote helicity would require some sort of molecular chaperone. Munc18 is

one possibility as it has been proposed to put SNARE into a mostly helical, partially zippered state, up to the ionic layer, which according to this study could very likely promote SNARE assembly.

3.4 Appendix

3.4.1 Adjustment of CG Parameters from Chapter 2 and Fortoul et al. ⁸

The CG model of SNARE and the forcefield used was based on the model described in Fortoul et al.⁸ where an ENM was used to hold the shape of helices and MJ potentials were used for helix-helix interactions. The majority of the simulations conducted in our previous work⁸ were done at quasi equilibrium conditions (0 K) and the simulations conducted in this chapter were done at 300 K, so some adjustment in parameters were required.

3.4.1.1 Adjustment of ENM Parameters

An ENM^{23,24} was used to represent intrahelical interactions and hold the shape of the helices. In this method, all beads within a single helix are connected to all beads within a cutoff distance, R_c , using harmonic springs using the energy potential

$$u_{spring}(r) = \frac{1}{2}k_s(r - r_0)^2 \quad (\text{A3.1})$$

where k_s is the spring constant, r is the distance between 2 beads, and r_0 is the natural length of the spring. In Fortoul et al.⁸, the value of k_s used was 0.0963 N/m. However, at 300 K slightly stronger springs were required to hold the helical shape at higher

temperatures. In order to determine an adequate value of k_s several simulations of the CG structure of the SNARE bundle were done for 20ns using different values of k_s . A value of 0.1685 N/m for k_s was chosen because at this value was able to produce helical proteins while still not deviating too much from the original value of k_s which was determined by matching AA and CG simulations in our previous work.

Because simulations in this work were done at 300 K, relaxation runs typically take longer than for 0 K cases. Therefore we wished to increase simulation speed by adjusting the value of R_c . A smaller R_c will create a smaller network of springs and require many less calculations. In Fortoul et al.⁸ a value of 20 Å was used. To find a minimum value of R_c that could be used without compromising simulation speed, several 20 ns CG simulations of SNARE were completed using different values of R_c . R_c could be decreased to a minimum of 16 Å without compromising the SNARE structure (using a k_s of 0.1685 N/m), therefore the value was decreased to 16 Å.

3.4.1.2 Adjustment of MJ Potential Parameters

MJ potentials²⁵⁻²⁷ were used to provide chemical specificity and to represent helix-helix interactions. Again because these simulations were done at 300 K, these parameters had to be adjusted from those of our previous work which were calibrated at quasi equilibrium conditions⁸. For a particular bead, every bead within the cutoff distance, R_{c_MJ} , of that bead (not on its own helix) has an interaction with that bead. For each interaction type there is a contact energy, e_{ij} , that is dependent on the two bead types, i and j , interacting (ex. Leu-Leu vs. Leu-Trp). The value of e_{ij} is adjusted for a particular system as

$$\varepsilon_{ij} = \lambda(e_{ij} - e_0) \quad (\text{A3.2})$$

where ε_{ij} is the scaled contact energy, λ is a scaling parameter, and e_0 is a shifting parameter. λ and e_0 are the same for all interaction types. A negative ε_{ij} represents an attractive interaction, while a positive ε_{ij} represents a repulsive interaction. The interaction potentials depend on both the sign of ε_{ij} as well as if the distance between beads is larger or smaller than the distance at the potential minimum, r_{ij}^0 .

The attractive interaction potential ($\varepsilon_{ij} < 0$) is

$$u_{ij}(r) = 4|\varepsilon_{ij}| \left[\left(\frac{\sigma_{ij}}{r} \right)^{12} - \left(\frac{\sigma_{ij}}{r} \right)^6 \right] \quad (\text{A3.3})$$

The repulsive interaction potential ($\varepsilon_{ij} > 0$) and $r < r_{ij}^0$ is

$$u_{ij}(r) = 4|\varepsilon_{ij}| \left[\left(\frac{\sigma_{ij}}{r} \right)^{12} - \left(\frac{\sigma_{ij}}{r} \right)^6 \right] + 2\varepsilon_{ij} \quad (\text{A3.4})$$

The repulsive interaction potential ($\varepsilon_{ij} > 0$) and $r \geq r_{ij}^0$ is

$$u_{ij}(r) = -4|\varepsilon_{ij}| \left[\left(\frac{\sigma_{ij}}{r} \right)^{12} - \left(\frac{\sigma_{ij}}{r} \right)^6 \right] \quad (\text{A3.5})$$

where r is the distance between the two beads and σ_{ij} is the interaction radius. σ_{ij} is the scaled average of the Van der Waals (VDW) diameters of the two bead types as shown as

$$\sigma_{ij} = A * \frac{\sigma_i + \sigma_j}{2} \quad (\text{A3.6})$$

where A is the scaling parameter, σ_i is the VDW diameter of bead type i , and σ_j is the VDW diameter of bead type j . In order to ensure that the proper parameters were being used, several 20 ns relaxation simulations of the SNARE bundle were done using different values of λ , e_0 , and A . Parameters were chosen to produce the right SNARE bundle width and overall bundle shape compared to that of the AA relaxed crystal structure. λ was

adjusted from 0.30 in our last study to 0.37. e_0 , was adjusted from 0 in our last study to $0.95*kT$. A was kept at a value of 0.8 from the last study.

3.4.2 Force Based MC Unraveling Method

One significant change to this SNARE CG model from our previous model is the addition of unraveling of Syb during FC unzipping. The method of unraveling used is based on the work of Gao et al.²⁸ that concluded that during SNARE unzipping, Syb unravels in a series of distinct events, as shown in Fig. 3.2, starting from a SNARE bundle that is fully helical: (1) The linker domain (LD) of Syb *reversibly* unravels, (2) Syb *reversibly* unravels up to the ionic layer, and (3) Syb *irreversibly* unravels completely. For each unraveling event, there is a probability of unraveling given as a function of the applied force as shown in Fig. 3.2.

3.4.2.1 Derivation of Folding/Unfolding Probabilities

The free energy diagram for the folded and unfolded Syb states is shown in Fig. A3.1

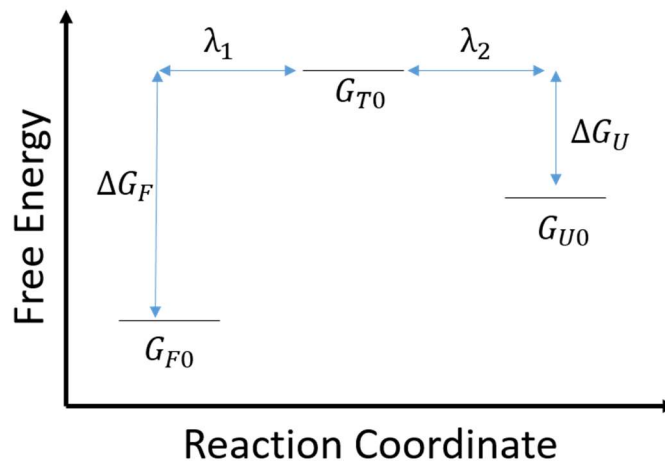


Figure A3.1 The free energy diagram for the transition to/from the folded state to the unfolded state of Syb is shown. The relative positions of the different states can vary depending on the applied force.

where the relative positions of the unfolded, folded, and transition states will differ based on their free energies. G_{F0} is the free energy of the folded state, G_{T0} is the free energy of the transition state, G_{U0} is the free energy of the unfolded state, ΔG_F is the change in free energy from the folded to transition state, and ΔG_U is the change in free energy from the unfolded to transition state. Under an applied force, f ,

$$\Delta G_F = G_{F0} - G_{T0} + f\lambda_1 \quad (\text{A3.7})$$

$$\Delta G_U = G_{U0} - G_{T0} + f\lambda_2 \quad (\text{A3.8})$$

The rate of going from the folded state to the unfolded state is

$$J^{F \rightarrow U} = J_0 \exp\left(-\frac{\Delta G_F}{kT}\right) \quad (\text{A3.9})$$

And the rate of going from the unfolded state to the folded state is

$$J^{U \rightarrow F} = J_0 \exp\left(-\frac{\Delta G_U}{kT}\right) \quad (\text{A3.10})$$

where J_0 is the inverse of the time between probability calculations. We assume the equilibrium condition that

$$P_F J^{F \rightarrow U} = P_U J^{U \rightarrow F} \quad (\text{A3.11})$$

where P_F is the probability of folding and P_U is the probability of unfolding. This can be rearranged to

$$\frac{P_F}{P_U} = \frac{J^{U \rightarrow F}}{J^{F \rightarrow U}} = \exp\left(-\frac{(-G_{U0} + f(\lambda_1 + \lambda_2) + G_{F0})}{kT}\right) \quad (\text{A3.12})$$

which can be simplified to

$$\frac{P_F}{P_U} = \exp\left(\frac{\Delta E - f\lambda}{kT}\right) \quad (\text{A3.13})$$

where λ is the combination of λ_1 and λ_2 and ΔE is the difference in the free energy of the folded and unfolded states. In terms of P_u , this can be rewritten as

$$\ln\left(\frac{P_U}{1 - P_U}\right) = \frac{-\Delta E + f\lambda}{kT} \quad (\text{A3.14})$$

Values of P_U as a function of f were taken from the experimental data of Gao et al.²⁸. This data was used to determine the values of ΔE to be 37.42 kT and λ to be 2.12 kT/N. For any given value of f , the values of P_F and P_U could be determined from Eqn. A3.13 and A3.14.

3.4.2.2 Folding/Unfolding Algorithm

As previously stated and shown in Fig. 3.2, during unzipping the Syb's helical structure changes in stages (LD, up to ionic layer, and entire Syb). In the SNARE xray crystal structure, the LD was not present, so that is not included in the model. Every 10 timesteps,

we determine the probability of folding/unfolding and accept/reject the event using a MC type method. The algorithm used is as follows:

- (1) If Syb is fully helical:
 - a. Generate a random number ($rand$) from a uniform distribution
 - i. If $rand < P_U$, accept the unravel event and unravel Syb up to the ionic layer.
 - ii. If $rand < P_U$, leave Syb fully helical.
- (2) If Syb is melted up to the ionic layer only
 - a. Generate $rand$.
 - i. If $rand < P_F$, accept the raveling event and refold Syb completely.
 - b. If b fails Generate $rand$.
 - i. If $rand < P_U$, accept the unraveling event and unravel Syb completely.
 - c. If b and d fail,
 - i. Leave Syb only unraveled up to the ionic layer
- (3) If Syb is completely melted, this is irreversible.

The force dependent MC algorithm allows for the reversible transition of a fully helical and partially helical SNARE. However the transition to a fully unraveled SNARE is irreversible in accordance with Gao et al.²⁸

3.4.3 Force Control Pulling Rate

For all of the FC unzipping simulations, a constant pulling rate was used. The pulling rate was chosen at a speed slow enough to keep the system at as close to equilibrium as possible while not going too slow that simulation speed was compromised. The pulling rate was varied from 0.22 pN/ns to 0.06 pN/ns as shown in Fig. A3.2.

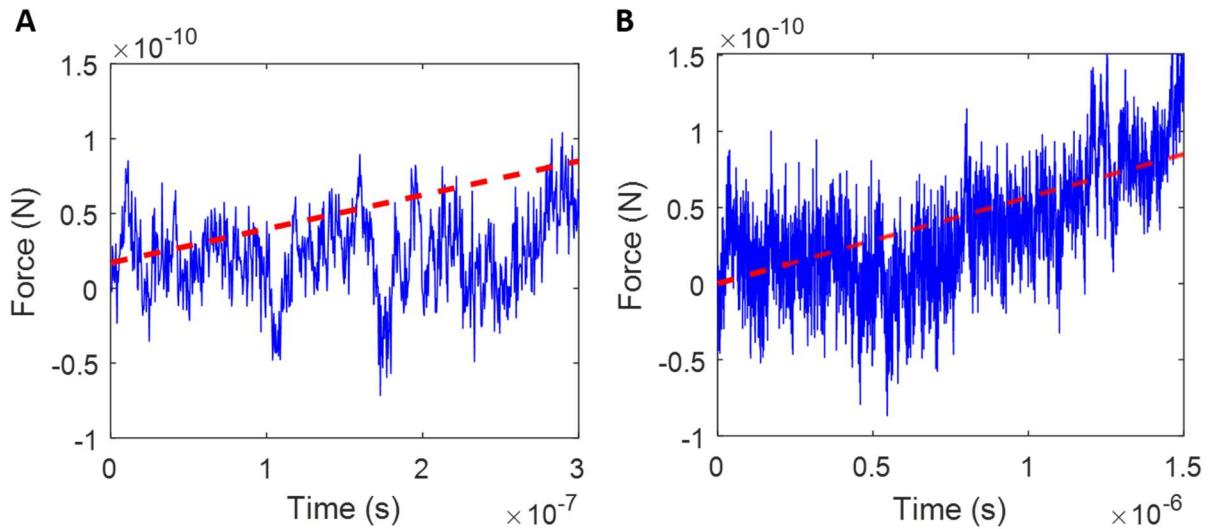


Figure A3.2 The force as a function of time is shown for 2 fully helical unzipping runs. The applied force on the C-terminal Syb bead (*dotted line*) as well as the negative of the force on the C-terminal Syx bead (*solid line*) are shown. (A) If a pulling rate of 2.2E-1 pN/ns is used which leads to the Syb and Syx C-terminal forces not being in equilibrium with one another. (B) If a slower pulling rate of 5.6E-2 pN/ns is used the forces are closer together and the system is closer to equilibrium.

In order to be close to equilibrium, the forces on the C-termini of Syb and Syx should be equal and opposite. At a pulling rate of 2.2E-1 pN/ns, the force on Syb is greater than the force on Syx, therefore it is too fast. When the pulling rate was lowered to 5.6E-2 pN/ns, the forces were closer together and the system was closer to equilibrium. A slower

pulling force did not bring the system much closer to equilibrium, so $5.6\text{E-}2$ pN/ns was chosen in order to balance system equilibrium conditions with simulation time.

3.4.4 Helical Formation/Raveling Methods

There are three main simulations methods used in this work: (1) Syb is helical for the entire simulation, (2) the force dependent MC unraveling/raveling method is used for unzipping and rapid helix formation is used during relaxation, and (3) the force dependent MC unraveling/raveling method is used for unzipping and the distance criterion helix formation is used for zipping. Method (1) is more straight forward in that there is not melting considered. Methods (2) and (3) are described in more detail below.

3.4.4.1 Rapid Helix Assembly

For the rapid helix assembly method, FC unzipping is used to set up an initial state using the force dependent MC unraveling/raveling method. The relaxation simulation is started from that initial state (which may or may not be helical), and during the first time step all of the ENM springs, which may have previously been removed, are replaced. The ENM provides the potentials required to keep helices helices. As a test this CG code was used to simulate the Syb helix independent of the SNARE bundle as shown in Fig. A3.7

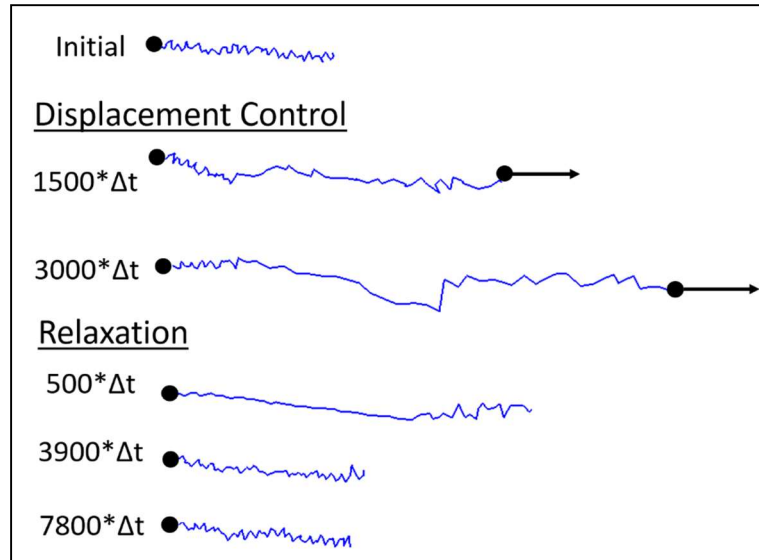


Figure A3.3 In order to prove that the rapid helix formation model is indeed “rapid”, the Syb structure was isolated with the N-terminal bead held fixed and a restraint on the C-terminal bead. The ENM springs for 10 helical turns were removed and Syb was stretched using displacement control on the C-terminal bead for which snapshots are shown. After Syb was stretched, the restraint on the C-terminal bead was released, and Syb was permitted to relax back into a helix (snapshots shown). This was accomplished in 7800 timesteps.

The initial Syb structure was taken from a relaxed CG structure of SNARE. The elastic network associated with 10 helical turns was removed from that structure making those 10 helical turns into a freely jointed chain. Over 3000 timesteps, displacement control was used on the C-terminal end of Syb to stretch out the molecule (with the N-terminal bead fixed). This was done slowly as to let the Syb structure equilibrate throughout the simulation. After Syb was stretched the restraints on the C-terminal Syb bead were released. Within 3900 timesteps, the Syb structure had unstretched nearly back to its helical length. Within 7800 timesteps the Syb structure was able to regain its helical form. This

demonstrated that the rapid helix formation model is actually “rapid” in that Syb can reform into a helix within 10^4 timesteps when the ENM springs are replaced.

3.4.4.2 Distance Criterion Helix Assembly

For the rapid helix assembly method, FC unzipping is used to set up an initial state using the force dependent MC unraveling/raveling method. The relaxation simulation is started from that initial state (which may or may not be helical), and the ENM springs are replaced slowly using a distance criterion. It is assumed that if beads are “close” to the bundle, they are helical. Therefore for every bead within a given distance, R_{DC} , of the SNARE bundle will be in a helical structure. To determine if a bead is within R_{DC} of the bundle, its minimum distance to Syx, SN1, and SN2 are calculated and if any of those distances qualify, the bead is in helical form. To accomplish this, all beads within R_{DC} of the SNARE bundle will have the ENM springs associated with that bead replaced. This criteria is checked every 10 timesteps and is reversible. For example if a bead was previous within R_{DC} of the bundle, but after the next 10 timesteps is no longer within R_{DC} of the bundle, the ENM springs for that bead will again be removed. The value of R_{DC} should be small enough so that Syb slowly regains its helical structure as it assembles but large enough that helix formation and assembly is possible. In order to determine a value of R_{DC} 2 distance criterion simulations were performed. The initial state for each was produced using the same force dependent MC unraveling/raveling method. From that same initial state, two separate simulations were performed with an R_{DC} of 1 nm and 0.5 nm.

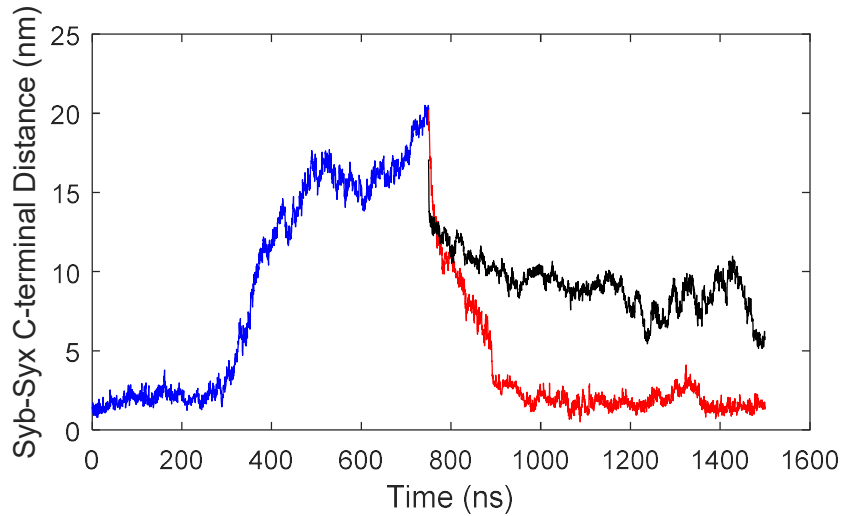


Figure A3.4 Two simulations were done where force dependent MC unraveling/raveling was used to unzip the SNARE bundle (*blue*) and set up an initial state for two distance criterion relaxation simulations. One relaxation simulation was done with an R_{DC} of 0.5 nm (*black*) and another with an R_{DC} of 1 nm (*red*).

In the case where R_{DC} the SNARE bundle was 0.5 nm, this value was too small and helix formation was not occurring in a short enough time to study so the bundle could not assemble. A smaller value of R_{DC} would also result in no assembly. In the case where R_{DC} the SNARE bundle was 1 nm, Syb was still able to assemble while slowly regaining its helical structure. The value of 1 nm for R_{DC} was ideal and chosen for this work. A larger value would act too similar to the rapid helix formation case.

3.5 References

1. Baker, R. W. & Hughson, F. M. Chaperoning SNARE assembly and disassembly. *Nat. Rev. Mol. Cell Biol.* **17**, 465–479 (2016).
2. Südhof, T. C. The synaptic vesicle cycle: a cascade of protein-protein interactions. *Nature* **375**, 645–653 (1995).
3. Hanson, P. I., Heuser, J. E. & Jahn, R. Neurotransmitter release - four years of SNARE complexes. *Current Opinion in Neurobiology* **7**, 310–315 (1997).
4. Söllner, T., Bennett, M. K., Whiteheart, S. W., Scheller, R. H. & Rothman, J. E. A protein assembly-disassembly pathway in vitro that may correspond to sequential steps of synaptic vesicle docking, activation, and fusion. *Cell* **75**, 409–418 (1993).
5. Rothman, J. E. Mechanisms of intracellular protein transport. *Nature* **372**, 55–63 (1994).
6. Gao, Y. *et al.* Single reconstituted neuronal SNARE complexes zipper in three distinct stages. *Science* (80-.). **337**, 1340–1343 (2012).
7. Bykhovskaia, M., Jagota, A., Gonzalez, A., Vasin, A. & Littleton, J. T. Interaction of the complexin accessory helix with the C-terminus of the SNARE complex: molecular-dynamics model of the fusion clamp. *Biophys J* **105**, 679–690 (2013).
8. Fortoul, N., Singh, P., Hui, C.-Y., Bykhovskaia, M. & Jagota, A. Coarse-Grained Model of SNARE-Mediated Docking. *Biophys. J.* **108**, 2258–69 (2015).
9. Hong, W. J. & Lev, S. Tethering the assembly of SNARE complexes. *Trends in Cell Biology* **24**, 35–43 (2014).
10. Kuhlee, A., Raunser, S. & Ungermann, C. Functional homologies in vesicle

- tethering. *FEBS Letters* **589**, 2487–2497 (2015).
11. Yu, I.-M. & Hughson, F. M. Tethering factors as organizers of intracellular vesicular traffic. *Annu. Rev. Cell Dev. Biol.* **26**, 137–156 (2010).
 12. Sutton, R. B., Fasshauer, D., Jahn, R. & Brunger, A. T. Crystal structure of a SNARE complex involved in synaptic exocytosis at 2.4 Å resolution. *Nature* **395**, 347–353 (1998).
 13. Ernst, J. A. & Brunger, A. T. High resolution structure, stability, and synaptotagmin binding of a truncated neuronal SNARE complex. *J. Biol. Chem.* **278**, 8630–8636 (2003).
 14. Wiederhold, K. *et al.* A coiled coil trigger site is essential for rapid binding of synaptobrevin to the SNARE acceptor complex. *J. Biol. Chem.* **285**, 21549–21559 (2010).
 15. Durrieu, M. P., Bond, P. J., Sansom, M. S. P., Lavery, R. & Baaden, M. Coarse-grain simulations of the R-SNARE fusion protein in its membrane environment detect long-lived conformational sub-states. *ChemPhysChem* **10**, 1548–1552 (2009).
 16. Min, D. *et al.* Mechanical unzipping and re-zipping of a single SNARE complex reveals hysteresis as a force-generating mechanism. *Nat Commun* **4**, 1705 (2013).
 17. Baker, R. W. *et al.* A direct role for the Sec1/Munc18-family protein Vps33 as a template for SNARE assembly. *Science (80-.)*. **349**, 1111–1114 (2015).
 18. Gallwitz, D. & Jahn, R. The riddle of the Sec1/Munc-18 proteins - New twists added to their interactions with SNAREs. *Trends in Biochemical Sciences* **28**, 113–116 (2003).

19. de Wit, H. *et al.* Synaptotagmin-1 Docks Secretory Vesicles to Syntaxin-1/SNAP-25 Acceptor Complexes. *Cell* **138**, 935–946 (2009).
20. Liang, B., Dawidowski, D., Ellena, J. F., Tamm, L. K. & Cafiso, D. S. The SNARE motif of synaptobrevin exhibits an aqueous-interfacial partitioning that is modulated by membrane curvature. *Biochemistry* **53**, 1485–1494 (2014).
21. Ellena, J. F. *et al.* Dynamic structure of lipid-bound synaptobrevin suggests a nucleation-propagation mechanism for trans-SNARE complex formation. *Proc Natl Acad Sci U S A* **106**, 20306–20311 (2009).
22. Fortoul, N., Singh, P., Hui, C. Y., Bykhovskaia, M. & Jagota, A. Coarse-grained model of SNARE-mediated docking. *Biophys. J.* **108**, 2258–2269 (2015).
23. Zhang, Z., Pfaendtner, J., Grafmuller, A., Voth, G. A. & Grafmüller, A. Defining coarse-grained representations of large biomolecules and biomolecular complexes from elastic network models. *Biophys. J.* **97**, 2327–2337 (2009).
24. Chu, J.-W. W. & Voth, G. A. Coarse-grained modeling of the actin filament derived from atomistic-scale simulations. *Biophys. J.* **90**, 1572–1582 (2006).
25. Miyazawa, S. & Jernigan, R. L. Self-consistent estimation of inter-residue protein contact energies based on an equilibrium mixture approximation of residues. *Proteins Struct. Funct. Genet.* **34**, 49–68 (1999).
26. Miyazawa, S. & Jernigan, R. L. Estimation of effective interresidue contact energies from protein crystal structures: quasi-chemical approximation. *Macromolecules* **18**, 534–552 (1985).
27. Miyazawa, S. & Jernigan, R. L. Residue-residue potentials with a favorable contact pair term and an unfavorable high packing density term, for simulation and

threading. *J. Mol. Biol.* **256**, 623–644 (1996).

28. Gao, Y. *et al.* Single Reconstituted Neuronal SNARE Complexes Zipper in Three Distinct Stages. *Science* **337**, 1340–1343 (2012).

Chapter 4: SNARE Protein Expression, Purification, and Characterization

4.1 Introduction

Both AA and CG SNARE protein simulations have been invaluable to the understanding of SNARE structure and function including the mechanism of synaptic vesicle to membrane fusion. From these types of simulations, we have been able to predict the number of SNAREs required for vesicle to membrane docking as well as attain mechanistic information on the SNARE assembly process¹. However simulations must be calibrated and validated thoroughly using experimental data in order to show that predicted results will be accurate and have physical meaning. In our past simulations we repeatedly calibrate and validate our forcefields using SNARE experimental data, particularly the optical tweezers experiment by Gao et al.².

For the purpose of determining the importance of amino acid sequence certain structural components within the SNARE and other molecules, it is often very useful to study mutations. For example, one study was looking at the interaction of Complexin (Cpx) with the SNARE bundle³. Complexin was discovered to bind to SNARE and clamp vesicle to membrane fusion by preventing full SNARE zippering. In order to study the importance of sequence on this behavior, a Syx T251I mutation was introduced at layer 7 of SNARE (near the C-terminus and close to where Cpx interacts with the bundle) both experimentally and in an AA MD simulation. In both cases, the small mutation was enough to weaken the Cpx clamping effect, and the AA simulation was used to further study the effect in detail.

We have developed a working CG model and forcefield for SNAREs which can be combined with a continuum vesicle to membrane model. However this system was only calibrated using experiments with one particular amino acid sequence. In order to study the effects of different mutations using simulations, we also need experimental data for those sequences but validated experimental data for many mutated sequences can be difficult to find. Therefore we proposed to develop our own in-house SNARE protein expression and purification protocol. This would give us the ability to choose any sequence we like, express and purify the proteins, and perform a few experiments. These experiments would be used to calibrate and validate our existing CG model which can be used to study the mutation effects on vesicle to membrane docking, SNARE assembly, etc. which are all difficult problems to study exclusively using experiments. Because we have detailed information on the unzipping forces required for SNARE based on the work of Gao et al.², we chose to start with that sequence in order to develop a protocol that we could confirm was working properly through ellipsometry, contact angle and Johnson-Kendall-Roberts (JKR) adhesion experiments.

4.2 Materials and Methods

4.2.1 SNARE Sequence

The sequences used for Syb (VAMP2 (1-92)), Syx (Synatxin 1A (187-265)), and SNAP25 (SNAP25B (1-206)) were slightly modified from those used in Gao, et al.² shown in Fig. 4.1.

VAMP2 and MBP
 MGHHHHHHGASKIEEGKLVIIWINGDKGYNGLAEVGGKFEKDTGIKVTVEHPDKLEEKFPQVAATGDGPDIIFWAHDRFGG
 YAQSGLLAEITPDKAFQDKLYPFTWDAVRYNGKLIAYPIAVEALSIIYNKDLLPNPPKTWEEIPALDKELKAKGKSALMFNLQ
 EPYFTWPLIAADGGYAFKYENGGYDIKDVGVNDAGAKAGLTFVLVLIKNKHMNADTDYSIAEAAFNKGETAMTINGPWAWWS
 NIDTSKVNYGVTVLPTFKGQPSKPFVGVLSAGINAASPNKELAKEFLENYLLTDEGLEAVNKDKPLGAVALKSYEEELVKDP
 RIAATMENAQKGEIMPNIQMSAFWYAVRTAVINAASGRQTVDEALKDAQTNELGTGGGGG LVPRGS GMSATAATVPPAA
 PAGEGGPPAPPPNLT SNRRLQQTQAQVDEVVDIMRVNVDKVLERDQKLSLDDRADALQAGASQFETSAAKLRKYWW
 KNGGSGNGSGGDYKDDDDKACALEHHHHHH

Syntaxin 1A and MBP
 MGHHHHHHGASKIEEGKLVIIWINGDKGYNGLAEVGGKFEKDTGIKVTVEHPDKLEEKFPQVAATGDGPDIIFWAHDRFGG
 YAQSGLLAEITPDKAFQDKLYPFTWDAVRYNGKLIAYPIAVEALSIIYNKDLLPNPPKTWEEIPALDKELKAKGKSALMFNLQ
 EPYFTWPLIAADGGYAFKYENGGYDIKDVGVNDAGAKAGLTFVLVLIKNKHMNADTDYSIAEAAFNKGETAMTINGPWAWWS
 NIDTSKVNYGVTVLPTFKGQPSKPFVGVLSAGINAASPNKELAKEFLENYLLTDEGLEAVNKDKPLGAVALKSYEEELVKDP
 RIAATMENAQKGEIMPNIQMSAFWYAVRTAVINAASGRQTVDEALKDAQTNELGTGGGGG LVPRGS GGNPAIFASGIIMD
 SSISKQALSEIETRHSEIIKLENSIRELHDMFMDMAMLVESQGEMIDRIEYNVEHAVDYVERAVSDTKKAVKYQSKARRKKG
 GSGNGSGSGGGCG LEHHHHHH

SNAP25B and MBP
 MGHHHHHHGASKIEEGKLVIIWINGDKGYNGLAEVGGKFEKDTGIKVTVEHPDKLEEKFPQVAATGDGPDIIFWAHDRFGG
 YAQSGLLAEITPDKAFQDKLYPFTWDAVRYNGKLIAYPIAVEALSIIYNKDLLPNPPKTWEEIPALDKELKAKGKSALMFNLQ
 EPYFTWPLIAADGGYAFKYENGGYDIKDVGVNDAGAKAGLTFVLVLIKNKHMNADTDYSIAEAAFNKGETAMTINGPWAWWS
 NIDTSKVNYGVTVLPTFKGQPSKPFVGVLSAGINAASPNKELAKEFLENYLLTDEGLEAVNKDKPLGAVALKSYEEELVKDP
 RIAATMENAQKGEIMPNIQMSAFWYAVRTAVINAASGRQTVDEALKDAQTNELGTGGGGG LVPRGS MAEDADMNLELE
 EMQRRADQLADESLESTRRMLQLVEESKDAGIRTLVMLDEQGEQLERIEEGMDQINKDMKEAEKNLTDLGKFSGLSVSPS
 NKLKSSDAYKKAWGNNQDGVVASQPARVVDEREQMAISGGFIRRVTDARENEMDENLEQVSGIIGNLRHMALDMGNEI
 DTQNRQIDRIMEKADSNKTRIDEANQRATKMLGSG LEHHHHHH

Figure 4.1 The sequences used for the SNARE proteins are shown using the pMBP7 cloning vector including MBP (*underlined*), 2 his-tags for purification (*gray*), a thrombin cleavage site (*green*), and the SNARE sequences (*yellow*).

All of the cysteines were changed to serines in order to prevent unwanted cross linking between helices. C-terminal cysteines were added to Syb and Syx for surface modification purposes. All of the protein sequences were inserted into pMBP7 vectors. A thrombin cleavage site was added between MBP and the SNARE sequences in order to remove MBP during the purification process. A His-tag was added at the N-terminal and C-terminal ends of each sequence for purification purposes.

4.2.2 SNARE Protein Expression and Purification

All of the SNARE sequences were cloned into pMBP7 cloning vectors. The plasmids for each protein were purchased from GenScript. The DNA plasmids were transformed into *E. Coli* BL21 cells. These were plated on LB agar kanamycin selective plates. Starter cultures were prepared followed by incubation with said antibiotic. Flash freezing and sonication were used to break open the cells after the proteins had been expressed, and an IMAC column was used for purification utilizing the 2 his-tags. The presence of the proteins were confirmed using an electrophoresis gel, and dialysis was performed in Tris buffer. More details on the protein expression and purification procedure are given in the Appendix.

4.2.3 Surface Functionalization on Silicon Wafer

In order to perform ellipsometry and contact angle measurements, we functionalized 1 cm x 1 cm silicon wafer with the SNARE proteins. The silicon wafer was piranha cleaned with a 3:1 solution of sulfuric acid with hydrogen peroxide for 30 minutes and thoroughly rinsed with DI water and dried with nitrogen. The samples were then added to 25 mL of acetone (95%) with 2.5 mL of (3-Aminopropyl)triethoxysilane (APTES) (1%) for 15 min and the resulting structure is shown in Fig. 4.2A.

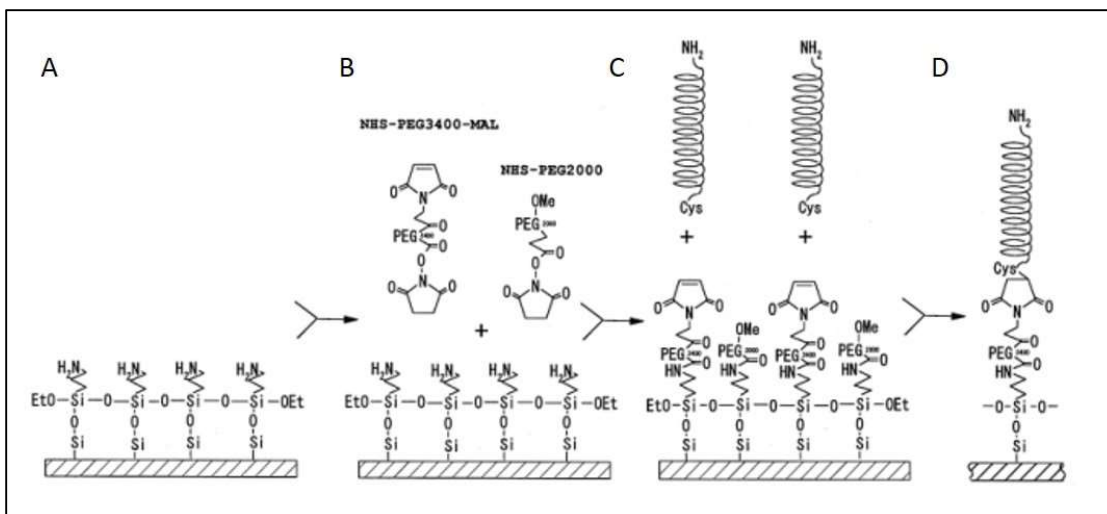


Figure 4.2 Structures are shown for (A) piranha cleaned silicon wafer functionalized with APTES, (B) piranha cleaned silicon wafer functionalized with APTES with NHS-PEG3400-MAL and NHS-PEG2000 in solution, (C) piranha cleaned silicon wafer functionalized with APTES and PEGs with a helical protein with a C-terminal cysteine (Syb or Syx) in solution, (D) and the final surface layer structure. Figure 4.2 was published by Idiris et al.⁴ and the copyright permission was obtained prior to the submission of this document.

The samples were then washed 5 times with acetone for 5 minutes each and dried with nitrogen. The samples were dried in a 110 C oven for 45 min.

Two types of PEGs (polyethylene glycol) were used in surface functionalization: a spacer PEG, NHS-PEG2000 (mPEG), and a linker PEG, NHS-PEG3400-MAL (malPEG), were used in ratios varying from 100:1 to 1:1⁴. The samples were added to 1.7E-7 total moles of PEG in DI water for 2.5 hours as shown in Fig. 4.2B (see Appendix for PEG molar calculation). Simultaneously the protein, Syb or Syx depending on the functionalization technique, was cleaved from MBP using the thrombin cleavage site. 0.001 mL of thrombin was added and to the protein and permitted to incubate for 1 hour. After the PEG functionalization, the samples were added to a 1 nM solution of the protein in 20 mM Tris pH 7.5 buffer with 5mM TCEP to prevent cross linking for 2.5 hours. The

C-terminal cysteine in Syb and Syx was utilized in this step for the attachment to the maleimide group as shown in Fig. 4.2C and 4.2D.

4.2.4 Surface Functionalization for JKR Experiments

The JKR experiment involves the indentation of a surface by a functionalized stiff spherical probe to measure adhesive interactions as shown in Fig. 4.3. For the JKR experiments two samples were required: a PDMS sample functionalized with Syx and a glass indenter (3-4mm) functionalized with Syb as shown in Fig. 4.3.

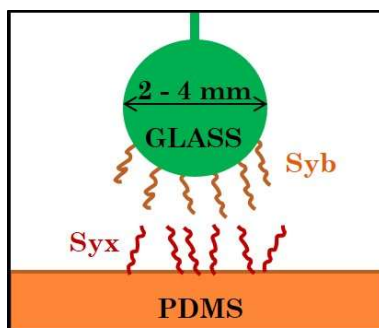


Figure 4.3 The JKR adhesion setup is shown including a PDMS functionalized surface with Syx and a glass indenter functionalized with Syb. SNAP25 is added in solution immediately before the adhesion experiments are performed.

For the PDMS surfaces the silicon wafer protocol was used, but the surfaces were only Piranha cleaned for 10 min. For the glass indenters, the silicon wafer protocol was used, but the surfaces were Piranha cleaned for 2 hours. This was to ensure that the glass indenters were free of contaminants due to the fact that these were reused for experiments.

4.2.5 JKR Experiments

Immediately before the JKR experiments were performed, the PDMS Syx sample was transferred to a petri dish of Tris buffer with TCEP and 2nM SNAP25 where the sample was adhered to the dish. The Syb coated glass indenter was used on the JKR to perform adhesion experiments between the two surfaces. The indenter was advanced until it was put in contact with the surface for anywhere from one second to overnight, and the indenter was retracted from the surface and the adhesion force measured.

4.3 Results and Discussion

To confirm that the protein purification had worked successfully, gel electrophoresis was conducted for all of the effluents from the IMAC column. The electrophoresis gel for Syb + MBP is shown in Fig. 4.4.

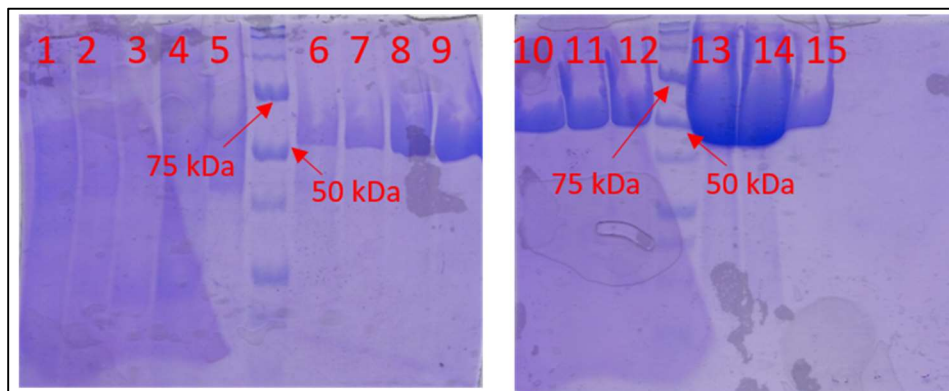


Figure 4.4 The electrophoresis gel for them IMAC effluents for the Syb + MBP purification is shown with the sample wells labeled. Syb + MBP (56 kDa) is present in wells 6 – 15.

Syb + MBP, 56 kDa, was present in sample wells 6 -15. Because sample wells 10 – 15 had a higher concentration of Syb, the effluents corresponding to those wells were used for

experiments. The gels for Syx and SNAP25 were quite similar and are given in the Appendix.

In order to determine the incubation time required for thrombin cleavage, samples of Syb + MBP and thrombin were incubated from 30 min to 2 hours and gel electrophoresis was conducted to confirm cleavage as shown in Fig. 4.5.

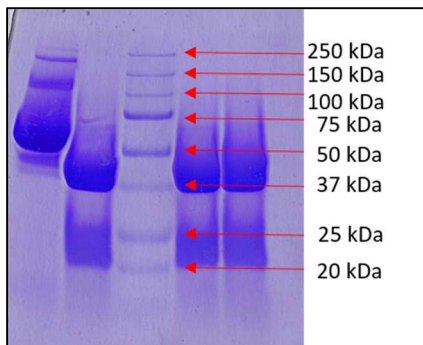


Figure 4.5 The electrophoresis gel for thrombin cleavage of Syb and MBP are shown. In the first well is Syb + MBP. The other wells contain the addition of thrombin with incubation times of 30 min, 1 hour, and 2 hours respectively for all of which thrombin cleavage is successful.

Thrombin cleavage of Syb (13 kDa) and MBP (43 kDa) was successful for all incubation times of 30 minutes to 2 hours, so 1 hour was used to be safe. The same results were shown for Syx and SNAP25 as shown in the Appendix.

In order to confirm that something was being added to the surface during each functionalization step, several ellipsometry experiments were performed on silicon wafer as shown in Table 4.1.

Table 4.1 Two sets of ellipsometry experiments were done on for surface functionalizations on silicon wafer. These experiments showed that with each new layer added to the sample there was an additional thickness gained in the sample.

Layer	Sample Set 1 Additional Thickness (nm)	Sample Set 2 Additional Thickness (nm)
Piranha	2.3 ± 0.3	2.1 ± 0.3
APTES	1.5 ± 0.2	1.2 ± 0.2
mPEG	0.1 ± 0.2	0.0 ± 0.2
mPEG + malPEG	0.8 ± 0.3	0.8 ± 0.2
Syb	4.4 ± 2.4	0.9 ± 0.1
Syx		0.7 ± 0.2
SNARE (Syb first)		1.9 ± 0.1
SNARE (Syx first)		0.5 ± 0.2

Two sets of experiments were done with two different sample sets. The samples in each set included piranha cleaned silicon wafer, piranha cleaned silicon wafer with APTES, piranha cleaned silicon wafer with APTES and mPEG, and piranha cleaned silicon wafer with APTES and mPEG and malPEG (100:1). Additionally there were samples including SNARE proteins: Syb, Syx, SNARE (with Syb added first and then Syx and SNAP25), and SNARE (with Syx added first and then Syb and SNAP25). All of the SNARE protein samples included the APTES, mPEG, and malPEG surface functionalization first. With each additional functionalization step performed there was an additional thickness layer added to the sample. The piranha and PEG experiments are consistent among the two sample sets, however there is a large discrepancy between the Syb data. For the SNARE experiments, there should be no difference in thickness between Syb or Syx being added first however the results said otherwise. It is very difficult to conclude whether the

functionalization worked or not from this data, however it did confirm that layers were added with each functionalization step.

In addition to the ellipsometry experiments, contact angle experiments using DI water were also done on same two sample sets as shown in Table 4.2.

Table 4.2 The advancing and receding contact angles were determined for all samples in sample set 1 and sample set 2 that correspond to the samples in Table 4.1.

	Sample Set 1		Sample Set 2	
	Advancing	Receding	Advancing	Receding
Functionalization	Angle (deg)	Angle (deg)	Angle (deg)	Angle (deg)
Piranha	69 ± 5	48 ± 7	58 ± 3	48 ± 7
APTES	46 ± 6	30 ± 7	50 ± 3	34 ± 10
mPEG	76 ± 5	54 ± 8	67 ± 6	39 ± 8
mPEG + malPEG	64 ± 5	49 ± 9	40 ± 4	32 ± 4
Syb	78 ± 6	55 ± 11	64 ± 6	46 ± 13
Syx			60 ± 6	50 ± 8
SNARE (Syb first)			75 ± 2	42 ± 13
SNARE (Syx first)			67 ± 6	48 ± 7

Within the margin of error nearly all of the advancing and receding angles are consistent between sample set 1 and sample set 2, however these results were inconclusive.

The ellipsometry experiments had shown that something was being deposited on the surface during each functionalization step, and the contact angle experiments were not conclusive. So in order to determine if the surface functionalization procedure was working, JKR adhesion experiments were conducted. In all experiments there was a functionalized PDMS surface put into contact with a functionalized glass indenter as shown in Fig. 4.3. Several sample types were used similar to those used in the ellipsometry and contact angle experiments and the results are summarized in Table 4.3.

Table 4.3 The results of JKR experiments are shown for several sample types. The results were robust for the three experiments performed for each sample type.

PDMS	Indenter	In Solution	Adhesion?
Piranha	Piranha	Tris/TCEP	No
malPEG	malPEG	Tris/TCEP	No
mPEG	mPEG	Tris/TCEP	Yes
mPEG + malPEG	mPEG + malPEG	Tris/TCEP	Yes
Syx	Syb	SNAP25	No

There was no adhesion shown during pull off for the piranha or malPEG samples. When mPEG was added with or without malPEG there was consistently adhesion for all 3 sets of experiments. For those experiments mPEG:malPEG concentrations were 100:1. When SNARE proteins were added, there was no adhesion for the 100:1 ratio, so this was increased to 10:1 and 1:1 and there was still no adhesion. In Gao et al.² the SNARE proteins were incubated overnight prior to optical tweezer experiments. In the results in Table 4.3 the incubation time was ~1 second where the indenter and PDMS surface were in contact. So we did 3 experiments with the SNARE system where the indenter was put in contact with the surface and left to incubate overnight. After ~16 hours the indenter was retracted from the surface. In 2 out of 3 of the overnight experiments there was adhesion. An example of the data from one of the overnight experiments is shown in Fig. 4.6.

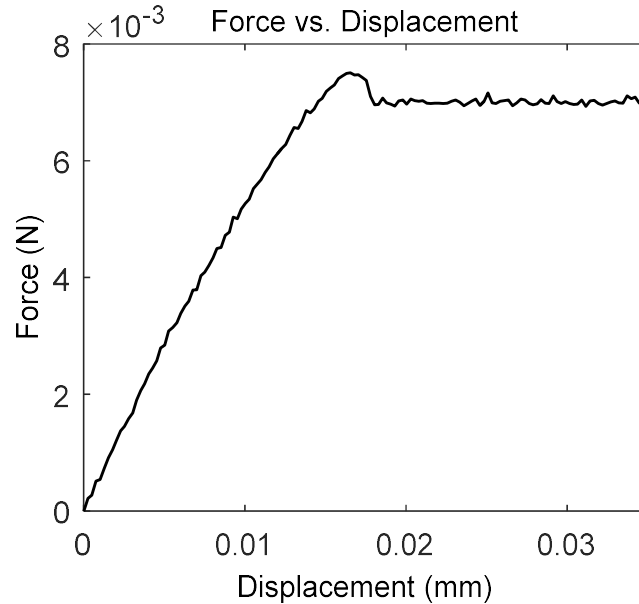


Figure 4.6 Successful force displacement data for an overnight JKR experiment for SNARE adhesion is shown. Upon recession from the PDMS surface, the glass indenter experiences an adhesive force.

As the indenter is receded from the PDMS surface (displacement) there is an adhesive force shown right before the indenter is pulled off the surface.

Despite the fact that there is a promising result that surfaces with SNARE proteins show adhesive interaction after overnight incubation, much more work still needs to be done to confirm these results. More surface characterization should be done to show that the SNARE proteins have assembled on the surface of the PDMS and glass indenter. Also the overnight experiments should be repeated using the piranha, APTES, and PEG controls to show that this is actual SNARE interaction and possibly bundle formation producing the adhesive forces. We also jumped from incubation times of ~ 1 second to ~ 16 hours, so a study should be done varying the incubation time to see if there is an ideal incubation time for bundle formation.

4.4 Appendix

4.4.1 Protein Expression and Purification Protocol^f

4.4.1.1 Protein expression in ZYP media

After the protein plasmid has been transformed into BL21 cell, make a liquid cell culture.

To make the liquid cell culture, add one colony of cells to 15mL Lysogeny broth (LB) with 50µg/mL kanamycin (kan) and incubate at 20C overnight. (Note that 50µg/mL of kan are kept with the cells at all stages of expression.) After incubation:

1. Dilute incubated cells 100x in ZYP + kan
 - a. ZYP formulation (200 mL):
 - i. 185.3 ZY
 - ii. 203.3 uL 1M MgSO₄
 - iii. 4.14 mL 50x 5052
 - iv. 10.34 mL 20x NPS
 - b. ZY formulation (1L):
 - i. 10g casein peptone
 - ii. 5 g yeast extract
 - iii. Bring to 1L with tap water
 - c. Allow cells to grow at 37C overnight. Collect cell pellets & store frozen.

^f These procedures were supplied by Dr. Bryan Berger, Dr. Rachel Barton, and Dr. Logan MacDonald.

4.4.2 Protein Flash Freezing and Tip Sonication Protocol

After completing the protein expression, protein flash freezing and tip sonication is done:

1. Take expression cell pellet & re-suspend in lysis buffer. For 200 mL of expressed culture, we typically re-suspend in 10 mL of the desired buffer.
2. Freeze suspension at -80C for 10 minutes or until frozen solid (longer is ok).
3. Thaw suspension in the 37C water bath. Once the solution is liquid, try to keep it cold as much as possible.
4. Make an ice slurry by filling a 400 mL beaker with ice and adding tapwater and a little salt.
5. Place sample in ice beaker & assemble the tip-sonicator. Ensure that the conical tube is not touching the beaker, nor is it touching the tip (the tip should be submerged in the liquid, but not touching the walls of the conical tube). Try to keep the liquid level of the sample below the slurry level.
6. Tip-sonicate for a processing time of 15 minutes with 20 second on/off pulses (total time of 30 minutes). Check that it is running at 15W and adjust the front dial as necessary to make this happen.
7. Once the sonication is done, clean-off the tip-sonicator using ethanol.
8. Centrifuge the suspension at maximum speed for 20 minutes.
 - a. Transfer the supernatant to a new conical tube.
 - b. Centrifuge the suspension at maximum speed for 20 minutes.
 - c. Transfer the supernatant to a new conical tube & either proceed to IMAC or store frozen.

4.4.3 Protein Purification Protocol

Protein purification is done using immobilized metal affinity chromatography (IMAC):

1. Prewash the column 3 column volumes (CV) of H₂O
2. Charge the column by running 2 CV of 0.2 M NiCl₂ solution
3. Wash unbound nickel ions by running 3 CV of H₂O
4. Equilibrate column in 1-2 CV of IMAC Lysis Buffer
5. Bind your sample by running your cell lysate, collect flow through.
6. Wash with 10 CV of 10mM imidazole, collect flow through.
7. Wash with 2 CV of 25mM imidazole, collect flow through.
8. Wash with 2 CV of 100mM imidazole, collect flow through.
9. Wash with 2 CV of 150mM imidazole, collect flow through.
10. Wash with 2 CV of 200mM imidazole, collect flow through in small aliquots.
11. Elute product with 2 CV of 500mM imidazole, collect flow through in small aliquots.
12. Strip away nickel and any bound proteins by running 2 CV of Column Stripping Buffer. If the resin still appears blue after this, add more stripping buffer.
13. Wash away any excess Column Stripping Buffer by running 3-5 CV of H₂O

4.4.4 Moles of PEG Calculation

A rough calculation for the amount of PEG required for surface functionalization was done based on the amount of APTES on the surface. There is ~1 APTES molecule on the surface per A² or 10¹⁶ APTES molecules/cm². For surface functionalization, there should be ~10x

the amount of PEG in solution. Each surface used has a surface area of $\sim 1\text{cm}^2$, so $\sim 10^{17}$ PEG molecules or $1.7\text{E-}7$ moles of PEG are required per sample.

4.4.5 Protein Purification Gels

To confirm that the protein purification had worked successfully, gel electrophoresis was conducted for all of the effluents from the IMAC column. The electrophoresis gel for Syx + MBP is shown in Fig. A4.1.

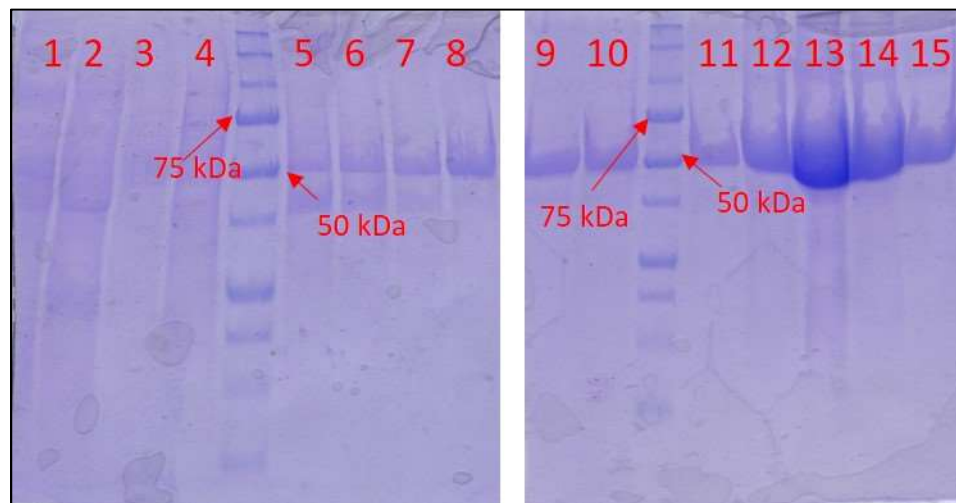


Figure A4.1 The electrophoresis gel for them IMAC effluents for the Syx + MBP purification is shown with the sample wells labeled. Syx + MBP (56 kDa) is present in wells 5 – 15.

Syb + MBP, 56 kDa, was present in sample wells 5 -15. Because sample wells 12 – 14 had a higher concentration of Syx, they were used for experiments. The electrophoresis gel for SNAP25 + MBP is shown in Fig. A4.2.

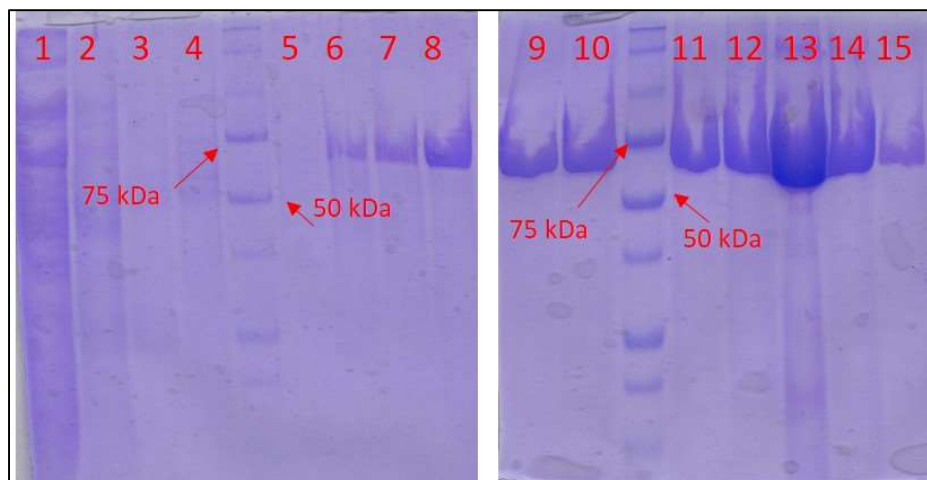


Figure A4.2 The electrophoresis gel for them IMAC effluents for the SNAP25 + MBP purification is shown with the sample wells labeled. SNAP25 + MBP (67 kDa) is present in wells 6 – 15.

SNAP25 + MBP, 67 kDa, was present in sample wells 6-15. Because sample wells 12 – 14 had a higher concentration of SNAP25, they were used for experiments.

4.4.6 Thrombin Cleavage Gels

In order to determine the incubation time required for thrombin cleavage, samples of Syx + and thrombin were incubated from 30 min to 2 hours. The same experiment was done with SNAP25 + MBP and thrombin. Gel electrophoresis was conducted to confirm cleavage as shown in Fig. A4.3.

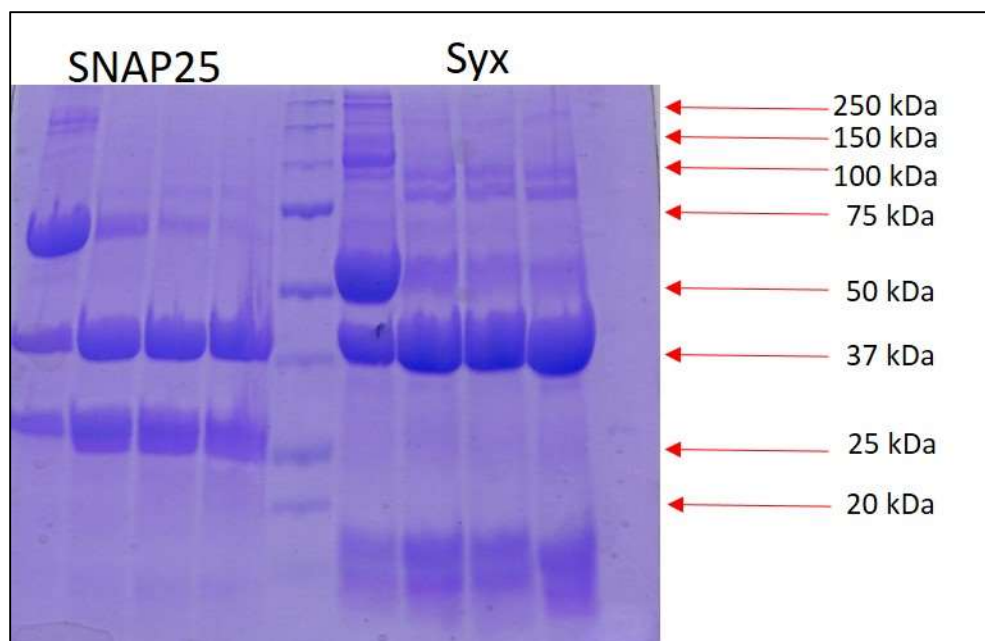


Figure A4.3 The electrophoresis gel for thrombin cleavage of Syx + MBP and SNAP25 + MBP are shown. To the left of the protein ladder in the first well is SNAP25 + MBP. The other wells (to the left of the ladder) contain the addition of thrombin with incubation times of 30 min, 1 hour, and 2 hours respectively for all of which thrombin cleavage is successful. To the right of the protein ladder in the first well is Syx + MBP. The other wells (to the right of the ladder) contain the addition of thrombin with incubation times of 30 min, 1 hour, and 2 hours respectively for all of which thrombin cleavage is successful.

Thrombin cleavage of SNAP25 (24 kDa) and MBP (43 kDa) was successful for all incubations times of 30 minutes to 2 hours, so 1 hour was used to be safe. These same analysis occurred for Syx (13 kDa) and MBP (43 kDa).

4.5 References

1. Fortoul, N., Singh, P., Hui, C. Y., Bykhovskaia, M. & Jagota, A. Coarse-grained model of SNARE-mediated docking. *Biophys. J.* **108**, 2258–2269 (2015).
2. Gao, Y. *et al.* Single Reconstituted Neuronal SNARE Complexes Zipper in Three Distinct Stages. *Science* **337**, 1340–1343 (2012).
3. Bykhovskaia, M., Jagota, A., Gonzalez, A., Vasin, A. & Littleton, J. T. Interaction of the complexin accessory helix with the C-terminus of the SNARE complex: molecular-dynamics model of the fusion clamp. *Biophys J* **105**, 679–690 (2013).
4. Idiris, a, Alam, M. T. & Ikai, a. Spring mechanics of alpha-helical polypeptide. *Protein Eng.* **13**, 763–70 (2000).

Chapter 5: Analytical Model and Kinetics of TIM Protein-Mediated Ebola Virus-Host Cell Adhesion[§]

5.1 Introduction

Since the most recent outbreak in 2014, the Ebola virus (EBOV) epidemic remains one of the world's major public health and safety concerns. EBOV is a single-stranded, negative-sense RNA virus that can infect humans and primates, and causes hemorrhagic fever¹. It has been proposed that the T-cell immunoglobulin and mucin domain (TIM) family proteins act as cell surface receptors for EBOV, and that the interaction between TIM and phosphatidylserine (PS) on the surface of EBOV mediates the EBOV-host cell attachment^{2,3}. In order to develop treatments/vaccines for EBOV it is necessary to better understand the conditions under which the virus is internalized into a host cell.

To infect a host cell, EBOV first attaches to the host cell using the cell's own T-cell immunoglobulin Ig and mucin domain 1 (TIM-1) transmembrane proteins, binding to the phosphatidylserine (PS) covering EBOV's surface as shown in Fig. 5.1A⁴.

[§] This work is part of a manuscript under review as: Dragovich, M., Fortoul, N., Jagota, A., Schutt, K., Xu, Y., Sanabria, M., Moyer, D., Moller-Tank, S., Maury, W., Zhang, X.F. Biomechanical Characterization of TIM Protein-Mediated Ebola Virus-Host Cell Interaction. (*under review*)

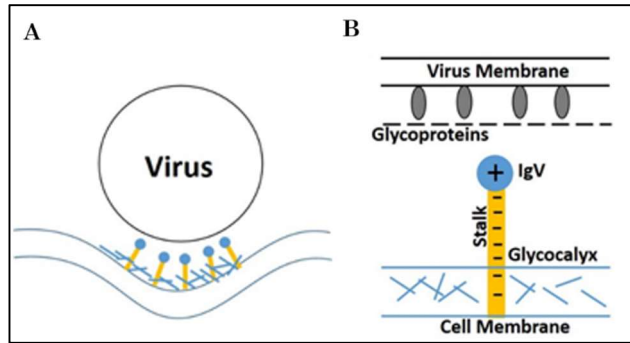


Figure 5.1 (A) Schematic of the adhesion of EBOV and a deformed host cell membrane is shown including TIM-1 receptors on the host cell. (B) A schematic of the TIM-1 receptor coming into contact with the EBOV surface. TIM-1 comprises a negatively charged stalk or mucin-like domain, MLD, and a positively charged head group, IgV. The base of the TIM-1 stalk is imbedded in the cell membrane that is covered with a flexible glycolyx layer. The surface of the virus is negatively charged and covered with PS and large glycoproteins.

After EBOV has adhered to the cell, endocytosis occurs and it is internalized by the cell. This process is electrostatically driven by the positive charge on the TIM-1 head group, IgV, and the negative charge of the PS on EBOV as shown in Fig. 5.1B. TIM-1 is composed of an IgV head group and a negatively charged stalk or mucin-like domain (MLD)⁵. The membrane bound end of TIM-1 is also covered with a glycolyx layer which hides some of the TIM-1 stalk. It has been shown that there is a minimum length of TIM-1 of 120 amino acids needed for EBOV to be internalized⁴. It has also been shown that the composition of the stalk does not affect this behavior⁴. We propose that perhaps the reason for these findings are that a minimum stalk length is required for TIM-1 emerge from the glycolyx and interact with PS. Another hypothesis is that TIM-1 must be long enough to overcome the electrostatic (or hydration) repulsion between the two negatively charge membranes.

Although TIM-1 and TIM-4 proteins have been characterized as the PVEER for EBOV², little is known about the biomechanical properties of the TIM-1/-4 – host cell interaction that help to initiate EBOV internalization. In particular, how the mechanical interaction collectively drives virus engulfment, remain unclear. The mechanical strength of interaction between TIM and PS has been determined using atomic force microscopy (AFM)-based single-molecule force spectroscopy, a method where a single bond rupture between two proteins can be measured directly.

How do the biophysical parameters identified from single-molecule studies relate to the mechanics of virus engulfment? To address this question, we have developed a simple model for EBOV-host cell interaction driven by adhesive interactions between the virus and cell-membrane receptors. Our model is based on interaction between the viral particle and cell membrane driving adhesion, which is at the energetic cost of deforming the membrane. Generally, the agents resisting deformation are either bending of the membrane, its tension, or both. We study two limiting cases where deformation is dominated by (1) membrane bending and (2) membrane tension.

We have begun to develop coarse-grained simulations to discriminate between the hypotheses for how TIM-1 functions in the binding of EBOV. In a previous work by Dragovich, et al.⁶, adhesion experiments were performed using an atomic force microscope, AFM. These experiments were used to quantify the adhesive interaction between TIM-1 and PS using a Bell-Evans model⁷. As a preliminary study, to begin to develop and calibrate the potentials to be used in the CG model with this experiment, we simulate one CG bead, representing IgV, and an analytical surface.

5.2 Materials and Methods

5.2.1 Analytical Model of EBOV-Host Cell Interaction

The virus is assumed to be cylindrical and relatively stiff so that it maintains its circular cross-section as shown in the schematic in Fig. 5.2.

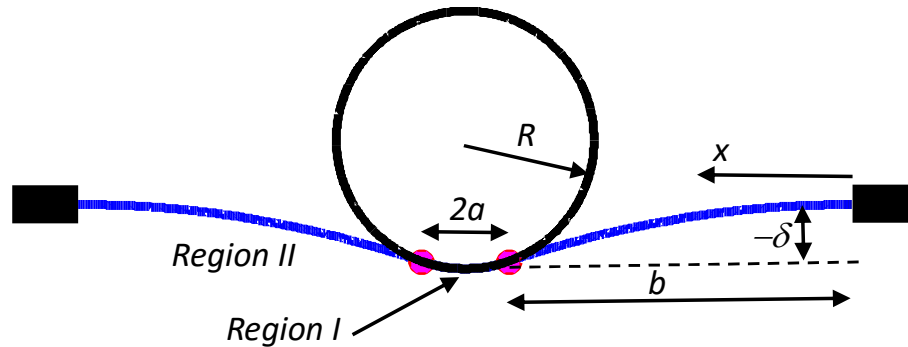


Figure 5.2 The geometry of a cylindrical viral particle with radius R adhering to a cell membrane is shown. The virus is long with a large internal pressure, so we assume it is stiff and model it in two-dimensions. Region I indicates the contact region of width $2a$ and Region II indicates the region where the membrane is free of lateral loads which is symmetrical with a width of b that has a maximum deformation of $-\delta$. Circles indicate the width of the contact region.

Because its length is large compared to the radius, we model the interaction in the two-dimensions of the virus cross-section. The viral particle is in the tens of nm in diameter, much smaller than the size of the cell it infects. Therefore, we assume that the cell membrane (Figure 5.2, blue line) is originally flat but deforms under contact with the virus. The contact width is $2a$ and the cell membrane is supported some distance $l=a+b$ away from the center of the virus attachment point; this represents a characteristic distance over which macropinocytosis occurs. We study this system under two limiting conditions: (1) membrane bending dominates and tension in the membrane is negligible and (2) tension

in the membrane dominates and membrane bending is negligible. To quantify this condition, consider the equation governing deflection w of the membrane when both bending and tension are present:

$$\kappa \frac{d^4 w}{dx^4} - T \frac{d^2 w}{dx^2} = 0 \quad (5.1)$$

where T is the tension (N/m) and κ is the bending rigidity,

When normalized by R , this is

$$\frac{\kappa}{TR^2} \frac{d^4 \bar{w}}{d\bar{x}^4} - \frac{d^2 \bar{w}}{d\bar{x}^2} = 0 \quad (5.2)$$

Thus, we can neglect tension if $\frac{\kappa}{TR^2} \gg 1$; conversely we can neglect bending if $\frac{\kappa}{TR^2} \ll 1$. Using values for $\kappa = 40 k_B T$ and $R=40$ nm, we find $T < 100$ pN/ μ m is needed to be able to neglect tension.

5.2.1.1 Membrane Bending Dominated Limiting Case

To express this mathematically, we write the total energy of the system as a sum of contributions from the elastic bending of the membrane and adhesion between the membrane and viral particle:

$$U_{total} = U_{elastic} + U_{adhesive} = U_I + U_{II} + U_{adhesive} \quad (5.3)$$

where $U_{elastic}$ is the contribution due to membrane bending, and $U_{adhesive}$ is the contribution due to adhesion between TIM and the viral surface. The elastic bending energy is a sum of contributions from two regions, region I where the membrane is in contact with the virus and region II where it is free of lateral loads. The deflection $w(x)$ is prescribed in

region I by the circular shape of the virus cross-section and, according to small-deflection plate theory⁸ $w(x)$ is governed in region II by the differential equation

$$\kappa \frac{d^4 w_{II}}{dx^4} = 0 \quad (5.4)$$

The elastic energy (per unit length out of plane) in terms of the displacements is given by

$$U_{elastic} = \int_b^l \frac{\kappa}{2} (w_I'')^2 dx + \int_0^b \frac{\kappa}{2} (w_{II}'')^2 dx \quad (5.5)$$

where κ is the bending rigidity of the cell membrane (in Joules; typically $10-100 \text{ k}_B T^{9-11}$).

The adhesion energy is given by

$$U_{adhesiv} = -\rho(l-b)\beta \quad (5.6)$$

where ρ is the number of bonds per unit area, and β is the free energy of binding of each bond. We proceed as follows. (See Appendix for details.) For specified values of parameters b , l , δ , R , β , and κ , we solve equation (5.4) subject to the conditions that deflection matches the circular profile of the virus in region I ; w and w' are both zero at $x=0$; and both are continuous at $x=b$. We then impose a condition of configurational energy balance, that is, energy is minimized with respect to location of the contact edge:

$$\frac{dU_{total}}{db} = 0 \quad (5.7)$$

The minimum energy condition provides the equilibrium value of b (and hence of a) eliminating b as a variable. Finally, we vary δ until the value of the net normal force, which is proportional to w'''' evaluated at $x=b$, equals zero. This situation corresponds to adhesion of the virus to the cell membrane in the absence of a net external force, and thus eliminates δ as a variable.

The following normalization simplifies the analysis and reveals the important dimensionless parameters that govern the adhesion behavior. We normalize all distances and sizes by the radius of the virus:

$$\bar{\delta} = \frac{\delta}{R}; \bar{b} = \frac{b}{R}; \bar{l} = \frac{l}{R} \quad (5.8)$$

and force and energy as

$$\bar{F} = \frac{F}{\rho\beta}; \bar{U}_{total} = \frac{U}{\rho\beta R} \quad (5.9)$$

With normalization we find that the solution depends solely on two dimensionless parameters:

$$\alpha = \frac{\kappa}{2\rho\beta R^2} \text{ and } \bar{l} \quad (5.10)$$

In particular, the equilibrium contact width, $\bar{a} = \bar{a}(\alpha, \bar{l})$. The first parameter, α , represents the ratio of bending energy ($\kappa/2$) for one radian and adhesion energy $\rho\beta$ ².

5.2.1.2 Membrane Tension Dominated Limiting Case

The total energy for the system is now:

$$U_{total} = U_{tension} + U_{adhesive} \quad (5.11)$$

where $U_{tension}$ is the contribution due to the work done by tension in the membrane, and $U_{adhesive}$ is the contribution due to adhesion between TIM and the viral surface represented by

$$U_{adhesive} = -R\theta\rho\beta \quad (5.12)$$

where θ is the angle of virus internalization ($\theta = 0$ representing no engulfment, and $\theta = \pi$ corresponding to total engulfment). The work done by the tension in the membrane, $W_{tension}$, equals the product of tension and total length:

$$W_{tension} = T(R\theta + l - R\sin\theta) \quad (5.13)$$

Adding the energy contributions from the tension in the membrane to the adhesive energy from the TIM-1 interaction we find the total energy to be

$$U_{total} = TR(\theta + \bar{l} - \sin\theta) - \frac{TR\theta\rho\beta}{T} \quad (5.14)$$

which can be nondimensionalized to

$$\bar{U}_{total} = \frac{U_{total}}{TR} = \theta + \bar{l} - \sin\theta - \frac{\theta}{\gamma} \quad (5.15)$$

using the dimensionless variable γ that represents the ratio between tension and adhesion

$$\gamma = \frac{T}{\rho\beta} \quad (5.16)$$

Setting the derivative of the energy to zero identifies the equilibrium condition:

$$\frac{d\bar{U}_{total}}{d\theta} = 1 - \cos\theta - \frac{1}{\gamma} = 0 \quad (5.17)$$

which yields the relation

$$\cos\theta = 1 - \frac{1}{\gamma} \quad (5.18)$$

5.2.2 Kinetics of TIM Protein-Mediated Ebola Virus-Host Cell Adhesion

Dragovich et al.⁶ quantified the interaction between TIM-1 and PS using a Bell Evans model

$$k = k^0 \exp\left(\frac{f\gamma}{kT}\right) \quad (5.19)$$

where k is the off rate or the rate at which TIM-1 dissociates from the surface covered with PS; k^0 is the off rate at no force (0.6 1/s), f is the applied force, and γ is the activation barrier width (0.33 nm). Using solely this information, we developed a potential that could

be used to reproduce this experimentally observed Bell-Evans model behavior and Eyring kinetics as shown in Fig. 5.3⁷.

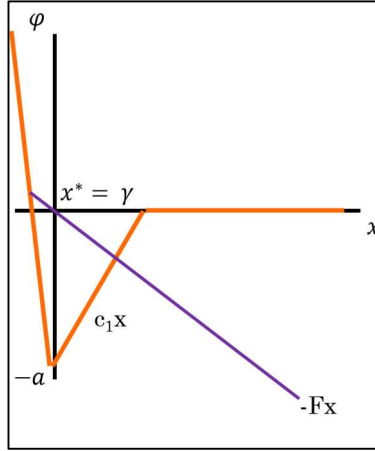


Figure 5.3 A pictorial model of the potential used between the TIM-1 head group and the EBOV surface (orange) as well as the potential from an external applied force (purple). The potential energy from these two forces is shown as a function of the distance between IgV and the surface. The interaction potential between TIM-1 and PS starts with a steep slope in order to prevent penetration into the surface. The minimum depth of the potential is $-a$ and it grows linearly with distance at a slope of c_1 until $x^* = \gamma$. The interaction potential becomes 0 at a distance greater than γ .

The interaction potential between TIM-1 and PS starts with a steep negative slope in order to penalize penetration into the surface. The minimum depth of the potential $-a$ and it grows linearly with distance at a slope of c_1 until $x^* = \gamma$. When this potential is put into the Bell-Evans form it results in

$$J = J^0 \exp\left(-\frac{c_1}{kT}\right) \exp\left(\frac{f\gamma}{kT}\right) \quad (5.20)$$

where J is analogous to the off rate, and $J^0 \exp\left(-\frac{c_1}{kT}\right)$ is analogous to k^0 in equation (5.19). Brownian dynamics simulations at 300K were conducted using this potential between the one-bead model and an analytical surface in order to confirm that the potential

gives the correct kinetics. These simulations were used to assure that the off rate and the applied force were related through equation (5.20).

5.3 Results and Discussion

5.3.1 Analytical Model of EBOV-Host Cell Interaction

Physically, attachment of the virus to the cell membrane is driven by adhesion between the two and we assume it is resisted by energy required to deform the cell membrane. We study this system under the limiting conditions where deformation is dominated by (1) membrane bending and (2) membrane tension.

5.3.1.1 Membrane Bending Dominated Limiting Case

Fig. 5.4 shows results for normalized half contact width versus normalized membrane bending stiffness for three different values of \bar{l} .

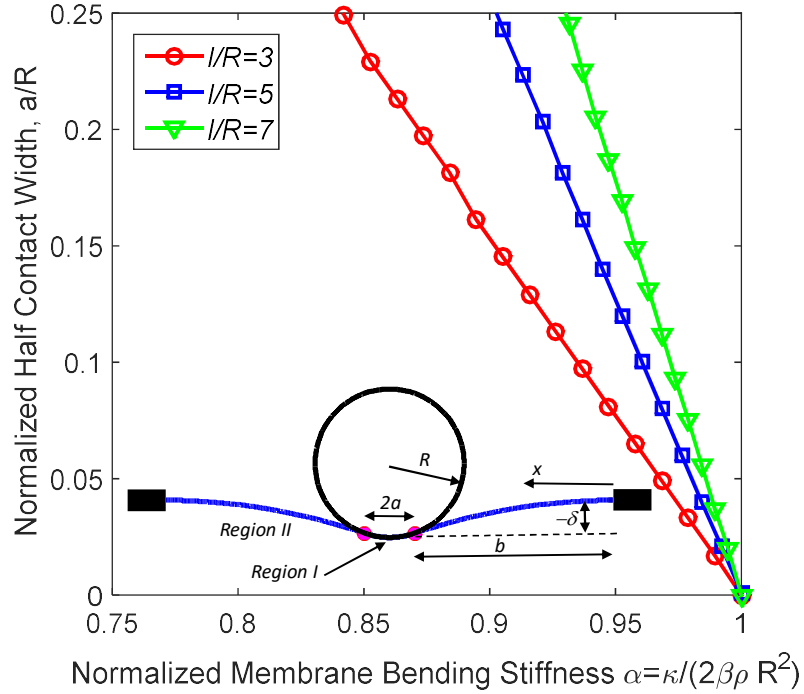


Figure 5.4 Mechanical model of EBOV-host cell attachment driven by adhesion and resisted by membrane bending. Our principal result is that if a dimensionless parameter representing the ratio of bending and adhesion energies has value greater than one, then there is no adhesion. If it assumes values less than one, contact width grows rapidly, leading presumably to engulfment.

The most important and definitive conclusion of our analysis is that a condition for adhesion between the virus particle and the cell is:

$$\alpha = \frac{\kappa}{2\rho\beta R^2} < 1 \quad (5.21)$$

This condition is *necessary* regardless of the value of \bar{l} . If this condition is not met, the equilibrium contact width is zero; there is no adhesion. The second important conclusion is that for relevant values of \bar{l} , the normalized contact width rises rapidly with decrease of membrane stiffness below the value needed to have any adhesion. We show results only over a range of contact width for which the linear Euler-Bernoulli beam model used here

should be accurate. However, it does show the importance of the parameter α : if it exceeds unity there is no adhesion; if it is only somewhat smaller than unity, the contact width increases rapidly, suggesting easy engulfment of the viral particle.

The EBOV virus has a radius of about 40 nm, whereas a reasonable length is about 250 nm. Therefore the range of l/R used in Fig. 5.4 matches the range of expected dimensions. Picking reasonable values for $\rho = 1000 \text{ per sq. } \mu\text{m}$, $\kappa=40 k_B T$; $\beta=50 kJ/mol$; $R=40 \text{ nm}$, we find $\alpha=0.62$, i.e., sufficiently small to drive engulfment.

5.3.1.2 Membrane Tension Dominated Limiting Case

Using the relation given in equation (5.18), θ was plotted as a function of γ in Fig. 5.5.

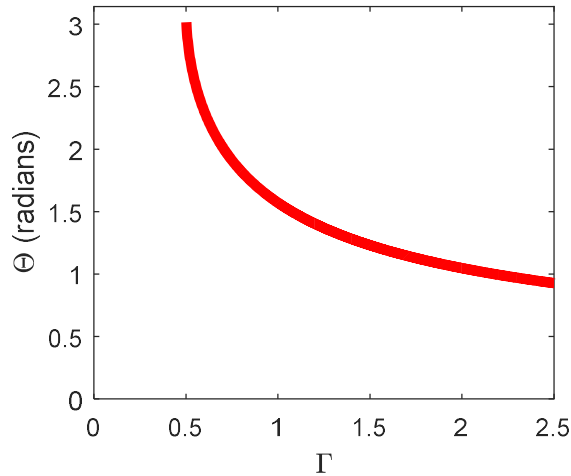


Figure 5.5 The angle of virus internalization, θ , is plotted as a function of the ratio between tension and adhesion, γ . Based on this relation, virus engulfment will occur when $\gamma < 1/2$.

We show that under the tension dominated conditions that viral engulfment is dependent on the unitless parameter γ . Four conditions are predicted:

- (a) If $\gamma = 1 \rightarrow \theta = \pi/2$, Tension is equal to adhesion and half of the virus is engulfed in the membrane
- (b) If $\gamma \gg 1 \rightarrow \theta = 0$, Tension dominates, the virus is just touching the membrane, and no engulfment occurs
- (c) If $\gamma = \frac{1}{2} \rightarrow \theta = \pi$, Adhesion dominates and the virus is engulfed.
- (d) If $\gamma < \frac{1}{2}$, Adhesion dominates and the virus is engulfed.

5.3.1.3 Overall Discussion for the Analytical Model

We have developed a simple model for the mechanics of attachment of viral particles to a cell membrane. The purpose of the model is to show how single molecule measurements can be combined with other physical properties of the system, such as density of ligand-receptor pairs and membrane stiffness, to predict whether and to what extent a viral particle will adhere to the cell membrane. We model attachment as being driven by TIM-PS adhesion and resisted by membrane bending. (In some cells, membrane tension will be the dominant player resisting deformation.) The model finds equilibrium configurations for given assumed deflections of the viral particle. It then seeks that deflection for which the force on the virus vanishes, thus finding the condition of natural adhesion without external forces. We show that the process is governed by two dimensionless parameters, the more important of which is the ratio of bending and adhesion energies. When this parameter exceeds unity in value, no adhesion is possible; for values less than one, the size of the

contact increases rapidly, presumably leading to engulfment of the viral particle. If tension dominates over bending as the agent resisting deformation, the engulfment is governed by the value of a single parameter representing the ratio of works of tension and adhesion.

5.3.2 Kinetics of TIM Protein-Mediated Ebola Virus-Host Cell Adhesion

One IgV bead was simulated using Brownian Dynamics at 300K. The interaction potential used is describe in Fig. 5.3. These simulations were conducted using various values of c_1 and applied force, f . For each set of conditions, 1000 beads were simulated and their off rates were determined for a value of $\gamma = 0.33nm$ as determined by Dragovich et al.⁶ as shown in the inset of Fig. 5.6.

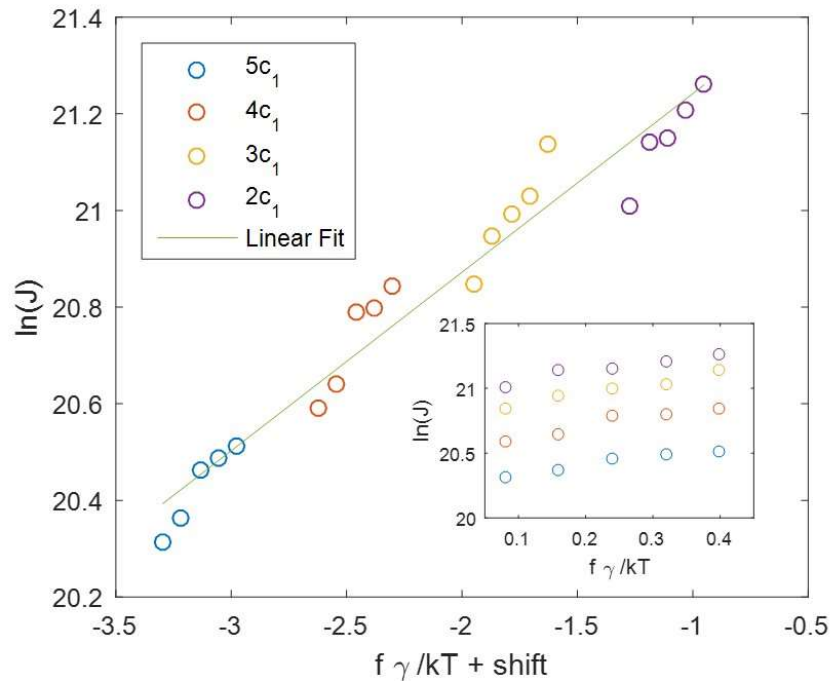


Figure 5.6 In the inset the natural log of the dissociation rate of a CG IgV of TIM-1 and PS is shown as a linear function of normalized external force for given values of c_1 . When the results are shifted based on the normalized values of c_1 , the results collapse onto a single linear master curve.

This shows that $\ln(J)$ is a linear function of $\frac{fY}{kT}$ for a given value of c_1 which agrees with equation (6.2). According to Eyring kinetics, as the value of c_1 is increased, the off-rate should decrease which is also a result that is captured by the model. When our results are shifted by $-\frac{c_1}{kT}$ in Fig. 5.6, our results collapsed onto a single master curve again confirming that the potential used produces valid kinetics. Now that the IgV and PS interaction potential has been validated, it can be applied to a future CG model of EBOV and host cell interaction.

5.4 Appendix

5.4.1 Mechanics of Virus Attachment by Adhesion When Bending Dominates Over Tension

In that case, the governing equation for membrane deformation is

$$\frac{d^4 \bar{w}}{d\bar{x}^4} = 0 \quad (\text{A5.1})$$

We analyze the geometry shown in Fig. 5.2, and adopt the following additional assumptions:

1. The membrane acts as if it is on a fluid substrate for $x=0$ to $x=1$
2. The membrane is tethered at the ends a distance b from where the viral particle touches the membrane
3. The virus is rigid and nondeformable
4. By symmetry about the center axis of the virus, we model only the right half of the geometry.

Region I (where the virus adheres to the membrane)

Membrane deflection in this adhesive zone between $x=b$ and $x=l=a+b$ is prescribed by the shape of the viral particle:

$$y = R - \sqrt{R^2 - x^2} = R - R\sqrt{1 - \left(\frac{x}{R}\right)^2} = R\left(1 - \sqrt{1 - \left(\frac{x}{R}\right)^2}\right) \quad (\text{A5.2})$$

Using Taylor Series Expansion, this approximates to $\frac{x^2}{2R}$. The deflection in region I is therefore

$$w_I(x) = \delta + \frac{x^2}{2R} \quad (\text{A5.3})$$

$$w_I'(x) = -\frac{x}{R} \quad (\text{A5.4})$$

At the boundary between regions I and II,

$$w_I(b) = \delta + \frac{b^2}{2R} \quad (\text{A5.5})$$

$$w_I'(b) = -\frac{b}{R} \quad (\text{A5.6})$$

Region II (Membrane not in contact with virus)

Integrating the governing equation (5.1), we get

$$w_{II}(x) = c_1 + c_2x + c_3x^2 + c_4x^3 \quad (\text{A5.7})$$

$$w'_{II}(x) = c_2 + 2c_3x + 3c_4x^2 \quad (\text{A5.8})$$

This must satisfy the boundary conditions:

$$w_{II}(b) = w_I(b) = \delta + \frac{b^2}{2R} \quad (\text{A5.9a})$$

$$w_{II}(0) = 0 \quad (\text{A5.9b})$$

$$w'_{II}(b) = w'_I(b) = -\frac{b}{R} \quad (\text{A5.9c})$$

$$w'_{II}(0) = 0 \quad (\text{A5.9d})$$

(There is no cumulative force in region I and II, but there is a point force at the boundary between the two regions.) This gives us the result that $c_1 = c_2 = 0$, and

$$c_3 = \frac{b^2 + 6\delta - 4bl + 3l^2}{2b^2} \quad (\text{A5.10})$$

$$c_4 = \frac{-2\delta + (b-l)l}{b^3} \quad (\text{A5.11})$$

Now that we know the deflection everywhere, we can create the expression for U_{total} (under displacement control)

$$U_{\text{total}} = U_{\text{elastic}} + U_{\text{adhesive}} = U_I + U_{II} + U_{\text{adhesive}} \quad (\text{A5.12})$$

$$U_{\text{total}} = \int_b^l \frac{\kappa}{2} (w'_I)^2 dx + \int_0^b \frac{\kappa}{2} (w'_{II})^2 dx - \rho(l-b)W \quad (\text{A5.13})$$

$$U_{\text{total}} = \frac{\kappa}{2} \left(\frac{1}{R}\right)^2 (l-b) + \frac{\kappa}{2} (4c_3^2 + 12c_4^2 b^3 + 12c_3 c_4 b^2) - \rho W(l-b) \quad (\text{A5.14})$$

In terms of normalized variables:

$$\bar{\delta} = \frac{\delta}{R}$$

$$\bar{b} = \frac{b}{R}$$

$$\bar{c}_3 = R c_3$$

$$\bar{c}_4 = R^2 c_4$$

$$\bar{l} = \frac{l}{R}$$

$$U_{\text{total}} = \frac{\kappa R}{2} \left(\frac{1}{R}\right)^2 (\bar{l} - \bar{b}) + \frac{\kappa}{2R} (4\bar{c}_3^2 + 12\bar{c}_4^2 \bar{b}^3 + 12\bar{c}_3 \bar{c}_4 \bar{b}^2) - \rho W R (\bar{l} - \bar{b}) \quad (\text{A5.15})$$

Further defining normalized variables:

$$\bar{F} = \frac{F}{\rho W}$$

$$\alpha = \frac{\kappa}{2\rho W R^2}$$

$$\bar{U}_{total} = \frac{U}{\rho W R}$$

We find

$$\bar{U}_{total} = \alpha(\bar{l} - \bar{b}) - \alpha(4\bar{c}_3^2 + 12\bar{c}_4^2\bar{b}^3 + 12\bar{c}_3\bar{c}_4\bar{b}^2) - (\bar{l} - \bar{b}) \quad (\text{A5.16})$$

First we find the equilibrium point, we set $\frac{d\bar{U}_{total}}{d\bar{b}} = 0$

$$\frac{d\bar{U}_{total}}{d\bar{b}} = \frac{\bar{b}^4 - 4\alpha\bar{b}^2\bar{l}^2 + 12\alpha\bar{b}\bar{l}(2\bar{\delta} + \bar{l}^2) + 9\alpha(2\bar{\delta} + \bar{l}^2)^2}{\bar{b}^4} \quad (\text{A5.17})$$

Next, we vary $\bar{\delta}$ until we find the condition where force on the membrane is zero. This is done by evaluating shear force

$$V = -\frac{dM}{dx} = -\frac{\kappa d^3w}{dx^3} = -6c_4 \quad (\text{A5.18})$$

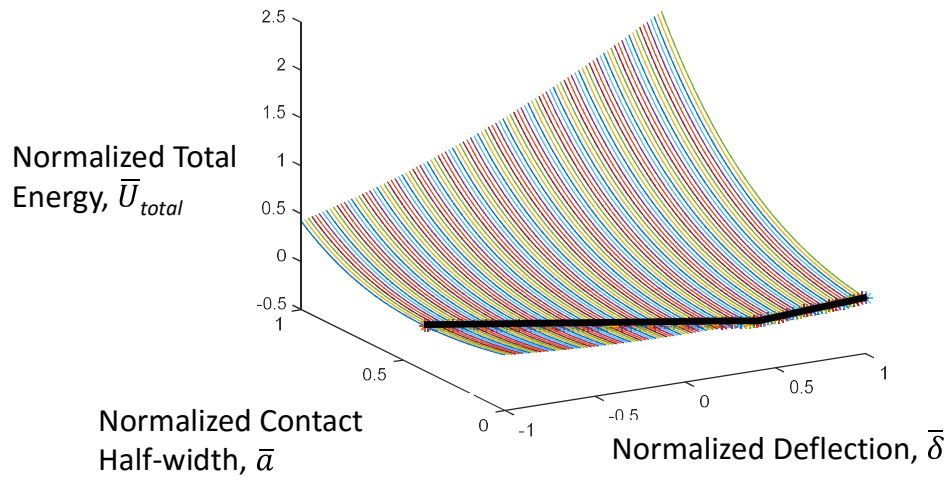


Figure A5.1 Example of normalized total energy as a function of normalized deflection and contact-half-width for $\alpha = 0.85$ and $\bar{l} = 5$. For each deflection, we find the value of normalized contact half-width that minimizes total energy. Then, along the locus of these points (black line in the figure), we search for the condition that shear force is zero.

3.6 References

1. Towner, J. S. *et al.* Newly discovered Ebola virus associated with hemorrhagic fever outbreak in Uganda. *PLoS Pathog.* **4**, (2008).
2. Moller-Tank, S., Kondratowicz, A. S., Davey, R. A., Rennert, P. D. & Maury, W. Role of the phosphatidylserine receptor TIM-1 in enveloped-virus entry. *J. Virol.* **87**, 8327–41 (2013).
3. Morizono, K. & Chen, I. S. Role of phosphatidylserine receptors in enveloped virus infection. *J Virol* **88**, 4275–4290 (2014).
4. Moller-Tank, S., Albritton, L. M., Rennert, P. D. & Maury, W. Characterizing functional domains for TIM-mediated enveloped virus entry. *J. Virol.* **88**, 6702–13 (2014).
5. Jemielity, S. *et al.* TIM-family Proteins Promote Infection of Multiple Enveloped Viruses through Virion-associated Phosphatidylserine. *PLoS Pathog.* **9**, (2013).
6. Dragovich, M. *et al.* Biomechanical Characterization of TIM Protein-Mediated Ebola Virus-Host Cell Interaction. *under Rev.* (2017).
7. Bell, G. I. Models for the specific adhesion of cells to cells. *Science (80-.).* **200**, 618–627 (1978).
8. Timoshenko, S. & Woinowsky-Krieger, S. *Theory of Plates and Shells.* (McGraw-Hill, 1959).
9. Evans, E. & Rawicz, W. Entropy-driven tension and bending elasticity in condensed-fluid membranes. *Phys. Rev. Lett.* **64**, 2094–2097 (1990).
10. Brochard, F. & Lennon, J. F. Frequency spectrum of the flicker phenomenon in

erythrocytes. *J. Phys.* **36**, 1035–1047 (1975).

11. Boal, D. H. *Mechanics of the Cell*. (Cambridge University Press, 2012).

Chapter 6: Conclusions and Future Work

6.1 Main Results

In Chapter 2 and Chapter 3 a CG model of SNARE was developed that included chemical specificity. Intrahelical interactions were represented with an elastic network model and interhelical interactions were represented using Miyazawa and Jernigan contact energies. This model is simulated using Brownian dynamics and was successfully calibrated and validated using AA simulations and experimental results.

In Chapter 2 the results of displacement control simulations to unzipper the CG SNARE were used in conjunction with a continuum model of the synaptic vesicle/membrane to predict the number of SNAREs required for docking. One SNARE can bring the vesicle within 3 nm of the membrane. Increasing this number, brings the two closer together. 4-6 SNAREs provide the minimum equilibrium vesicle to a membrane distance of about 2 nm. The addition of more SNAREs increases this distance. In Chapter 2 the minimum distance between the synaptic vesicle and membrane solely through SNARE adhesive forces was 2nm indicating that SNAREs cannot initiate fusion without the help of other molecular players.

In Chapter 3 the SNARE CG model was used to study the SNARE assembly process. Force control unzipping and relaxation simulations were used to set up an initial state and determine the assembly pathway. The time for assembly was a combination of time required for Syb folding and the time for Syb to SNARE assembly. The time for SNARE assembly (after Syb has become helical) increases exponentially with the degree of SNARE unzipping. For a partially zippered SNARE this assembly would occur in

~100ns. However according to experimental data¹ Syb folding can add up to seconds to this timescale. This is not a feasible time for assembly for evoked vesicle to membrane fusions which occurs in microseconds. Therefore a chaperone such as Munc18 would be required to put SNARE into a half-zippered, helical primed state for assembly to occur.

In Chapter 4 a protocol for SNARE adhesion experiments was proposed from protein expression and purification to surface functionalization to experimental setup. When properly validated, this protocol could be used to study the effect of mutations and could be used to help calibrate the SNARE CG model.

In Chapter 5 a continuum model of the EBOV virus and host cell membrane was developed that included membrane bending, membrane tension, and TIM-1 PS adhesion. This model was used to predict the equilibrium virus/host cell configuration under two limiting cases: (1) High membrane bending stiffness and (2) high tension. For the membrane bending limit, a dimensionless number was extracted, the ratio of bending stiffness to adhesion energy, which completely determined the equilibrium state of the system and whether engulfment is probable. Analogously under the tension limit, a dimensionless number was extracted, the ratio of membrane tension to adhesion energy, that predicts engulfment conditions. Based on experiment AFM measurements², an IgV PS interaction potential was developed and validated to be used for coarse-grained modeling.

6.2 Ongoing and Future Work

In Chapters 2 and 3 a SNARE CG model was developed. This model was combined with a continuum model of the vesicle/membrane to predict equilibrium vesicle to membrane distances. However due to the nature of the continuum model, fusion could not be simulated. Currently a 3 bead CG model of the vesicle/membrane is being developed using LAAMPS. The SNARE CG model is being combined with the CG vesicle/membrane model in LAMMPS as well, and additional linker and transmembrane domains have been added to the SNARE in order to insert the helices into the membranes. After this model has been fully calibrated, it can be used to study the mechanisms of synaptic vesicle to membrane fusion.

In Chapter 4 an experimental protocol was developed for SNARE protein expression and purification which was validated. These proteins were used to modify PDMS surfaces and glass indenters to perform adhesion experiments. The surface modification and adhesion experimental procedures still need to be validated. A surface sensitive technique such as X-ray photoelectron spectroscopy or the AFM should be used to confirm that the surface functionalization protocol has worked. Secondly, SNARE bundle formation should also be confirmed. This may be difficult to do with surfaces that have been functionalized, but the bundle formation should be proven through the use of gel electrophoresis or a technique like small angle X-ray scattering.

In Chapter 5 a potential for the adhesive interaction between IgV and PS was developed. It has been shown that there is a minimum length of TIM-1 of 120 amino acids that allows EBOV to be internalized³. It has also been shown that the

composition of the stalk does not affect this behavior³. We propose that perhaps the reason for these findings are that the length of the stalk is a result of ensuring that TIM-1 is long enough to emerge from the glycocalyx and bind with PS. Another theory is that TIM-1 must be long enough to overcome the electrostatic repulsion region between the two negatively charge membranes. Currently CG simulations are being developed incorporating the IgV/PS potential to understand what hypothesis may hold true for how TIM-1 functions in the binding of EBOV.

6.3 References

1. Min, D. *et al.* Mechanical unzipping and reziping of a single SNARE complex reveals hysteresis as a force-generating mechanism. *Nat Commun* **4**, 1705 (2013).
2. Dragovich, M. *et al.* Biomechanical Characterization of TIM Protein-Mediated Ebola Virus-Host Cell Interaction. *under Rev.* (2017).
3. Moller-Tank, S., Albritton, L. M., Rennert, P. D. & Maury, W. Characterizing functional domains for TIM-mediated enveloped virus entry. *J. Virol.* **88**, 6702–13 (2014).

Nicole Fortoul

1569 Ralston Road
Bethlehem, PA 18018

www.linkedin.com/in/nicolefortoul

(267)410-7079

nicole.fortoul@gmail.com

Date of Birth: December 13th, 1989
Place of Birth: Jersey City, NJ
Parents: Mr. Alejandro Fortoul & Mrs. Kathleen Fortoul

EDUCATION

Lehigh University, Bethlehem PA Aug 2012 - May 2017
Ph.D, Chemical Engineering, GPA: 3.78
Advisor: Dr. Anand Jagota
Honors & Distinctions: Peebles Award for Graduate Student Research in Adhesion Science (17), ChEGA Vice President (14-15)

Lehigh University, Bethlehem PA Aug 2008 - May 2012
B.S., Chemical Engineering, GPA: 3.73
Honors & Distinctions: Tau Beta Pi (12). National Society of Collegiate Scholars (08-12), Dean's List (6 Semesters), Joseph J. Grano Scholarship (08-12).

TECHNICAL SKILLS

- Modeling Software: MATLAB, GROMACS, LAMMPS, Aspen Plus, Aspen Plus Dynamics, Mathematica, Mathcad
- Programming Languages: C++, Python
- Experimental Techniques: Ellipsometry, AFM, JKR, Contact Angle, Protein Expression and Purification
- Languages: English, Intermediate Spanish

RESEARCH/WORK EXPERIENCE

Lehigh University
Bethlehem, PA

Graduate Research Assistant

Aug 2012 - May 2017

- Developed an alpha carbon based coarse-grained (CG) model of the neuronal SNARE/Complexin protein complex with chemical specificity in MATLAB and LAMMPS that was calibrated using normal modes analysis, published experimental results, and individual helix all-atom simulations conducted in GROMACS . Used said model to study the number of SNAREs required for docking as well as SNARE assembly.
- Developed a continuum model of the EBOV and host cell membrane to determine the conditions for viral engulfment

Lehigh University

Bethlehem, PA

Teaching Assistant

- Biological Fluid Mechanics
- Chemical Engineering Thermodynamics
- Chemical Engineering Lab
- Chemical Engineering Transport Processes

Jan 2014 - May 2017

Colgate-Palmolive

Piscataway, NJ

Global Supply Chain Intern

- Established best practices and stage gate elements for the design, construction, and operation of global technology centers in the 21st century, encompassing all aspects of product development from early research to sensory & consumer insight, through implementation & support, and regulatory approval.

Summer 2007

PUBLICATIONS

- Fortoul, N., Bykhovskaia, M., Jagota, A. "Coarse-Grained Model of SNARE Shows that Partial Assembly and Helicity are Required for Quick Zippering." (2017) (*under preparation*)
- Dragovich, M., Fortoul, N., Jagota, A., Schutt, K., Xu, Y., Sanabria, M., Moyer, D., Moller-Tank, S., Maury, W., Zhang, X.F. "Biomechanical Characterization of TIM Protein-Mediated Ebola Virus-Host Cell Interaction." (2017) (*under review*)
- Fortoul, N., Singh, P., Hui, C.Y., Bykhovskaia, M., and Jagota, A. "Coarse-Grained Model of SNARE-Mediated Docking." *Biophysical Journal* 108, no. 9 (2015): 2258-2269.

LEADERSHIP**Gordon Research Seminar on the Science of Adhesion**

Jan 2014 – Jul 2015

Chair

- Invited and selected speakers and attendees based on talk abstracts and publications
- Organized the program and extracurricular activities for the 2 day seminar
- Allocated available funds to attendees and optimized the seminar budget.